

## ABSTRACT

Title of Dissertation: Measurements of Doping-Dependent Microwave  
Nonlinearities in High-Temperature Superconductors

Sheng-Chiang Lee, Doctor of Philosophy, 2004

Dissertation directed by: Professor Steven M. Anlage  
Department of Physics

I first present the design and use of a near-field permeability imaging microwave microscope to measure local permeability and ferromagnetic resonant fields. This microscope is then modified as a near-field nonlinear microwave microscope to quantitatively measure the local nonlinearities in high- $T_c$  superconductor thin films of  $\text{YBa}_2\text{Cu}_3\text{O}_{7-\delta}$  (YBCO). The system consists of a coaxial loop probe magnetically coupling to the sample, a microwave source, some low- and high-pass filters for selecting signals at desired frequencies, two microwave amplifiers for amplification of desired signals, and a spectrum analyzer for detection of the signals. When microwave signals are locally applied to the superconducting thin film through the loop probe, nonlinear electromagnetic response appearing as higher harmonic generation is created due to the presence of nonlinear

mechanisms in the sample. It is expected that the time-reversal symmetric (TRS) nonlinearities contribute only to even order harmonics, while the time-reversal symmetry breaking (TRSB) nonlinearities contribute to all harmonics. The response is sensed by the loop probe, and measured by the spectrum analyzer. No resonant technique is used in this system so that we can measure the second and third harmonic generation simultaneously. The spatial resolution of the microscope is limited by the size of the loop probe, which is about 500  $\mu\text{m}$  diameter. The probe size can be reduced to  $\sim 15 \mu\text{m}$  diameter, to improve the spatial resolution.

To quantitatively address the nonlinearities, I introduce scaling current densities  $J_{NL}(T)$  and  $J_{NL}'(T)$ , which measure the suppression of the super-fluid density as  $n_s(T, J)/n_s(T, 0) = 1 - (J/J_{NL}'(T)) - (J/J_{NL}(T))^2$ , where  $J$  is the applied current density. I extract  $J_{NL}(T)$  and  $J_{NL}'(T)$  from my measurements of harmonic generation on YBCO bi-crystal grain boundaries, and a set of variously under-doped YBCO thin films. The former is a well-known nonlinear source which is expected to produce both second and third harmonics. Work on this sample demonstrates the ability of the microscope to measure local nonlinearities. The latter is proposed to present doping dependent TRS and TRSB nonlinearities, and I use my nonlinear microwave microscope to measure the doping dependence of these nonlinearities.

MEASUREMENTS OF DOPING-  
DEPENDENT MICROWAVE  
NONLINEARITIES IN HIGH-  
TEMPERATURE SUPERCONDUCTORS

by

Sheng-Chiang Lee

Thesis submitted to the Faculty of the Graduate School of the  
University of Maryland, College Park in partial fulfillment  
of the requirements for the degree of  
Doctor of Philosophy  
2004

Advisory Committee:

Professor Steven M. Anlage, Chair/Advisor  
Professor J. Robert Anderson  
Assistant Professor Michael Fuhrer  
Associate Professor Romel Gomez  
Professor Frederick C. Wellstood

©Copyright by  
Sheng-Chiang Lee  
2004

DEDICATION

To Connie  
and my precious Lord,  
Jesus Christ

## ACKNOWLEDGMENTS

To me, doing research is an everlasting struggle that only furthers our understanding of the mysterious creation of God, but also challenges our personal integrity and character.

Through the years I have spent here, I have learned a lot and been very grateful.

First, I would like to thank my advisor, Steve Anlage, for his patience and continual encouragement, even when my research was not going so well. His enthusiasm for physics and positive attitude have been an inspiration to me. Secondly, I would like to give my appreciation to my co-workers: Atif Imtiaz, Dragos Mircea, Sameer Hammedy, Greg Ruchti, Nathan Orloff, and Marc Pollak, with whom I have had many interesting conversations not only about physics, but about other things in life. I would also like to thank David Steinhauer, Andy Schwartz, and Johan Feenstra, who have been great examples and encouragement to me in my early stage of research. I thank Matt. Sullivan for his help in making YBCO thin films, and Ben Palmer for adjusting the oxygen deficiency of these films for me. I would like to thank Fred Wellstood and Chris Lobb, with whom I have had very helpful conversations. I would like to thank Bob Anderson, Michael Fuhrer, Fred Wellstood, and Romel Gomez for being on my doctoral defense committee. I am also grateful for support from the National Science Foundation (NSF) and

from the NSF Material Research Science and Engineering Center through support of Shared Experimental Facility, through the GOALI program and the DARPA TASS program to my microscope.

I thank my parents and parents-in-law for their encouragement and support through these years. I would like to especially thank my wife Connie, who was always encouraging, supportive, and loving as I struggled with my research. I truly believe that she deserves another P.H.D. degree (Push her Husband to Doctoral degree). Finally and most importantly, I would like to thank my God for all these blessings He has given me. Without His help and guidance, mercy and grace, I would not have been able to walk through these years and become who I am today.

## TABLE OF CONTENTS

Table of Contents.....	v
List of Tables .....	x
List of figures .....	xi
Glossary .....	xvi
1. Introduction to the Nonlinear Near-Field Microwave Microscope.....	1
1.1 Introduction.....	1
1.2 Ancestor of the Nonlinear Near-Field Microwave Microscope: The Permeability Imaging Near-Field Microwave Microscope.....	5
1.2.1 Introduction .....	5
1.2.2 Experimental Setup.....	6
1.2.3 Samples .....	9
1.2.4 Results of Permeability Imaging .....	10
1.2.5 CMR Field Imaging .....	17
1.2.6 Conclusions .....	22
1.3 The Nonlinear Near-Field Microwave Microscope .....	22



1.3.1 Introduction .....	22
1.3.2 Experimental Setup .....	24
1.3.3 Principle of Operation .....	27
2. Introduction to Nonlinear Superconductivity .....	30
2.1 Nonlinear Meissner Effect.....	32
2.1.1 The Ginzburg-Landau Theory .....	32
2.1.2 The Bardeen-Cooper-Schrieffer (BCS) Theory .....	35
2.1.3 Prior Experiments on the Nonlinear Meissner Effect .....	42
2.2 Vigni's model of modulating normal fluid density by external AC fields .....	45
2.3 Andreev Bound State Nonlinearities.....	48
2.4 Another Potential TRSB Nonlinearity – Varma's proposal.....	56
3. The Nonlinear Scaling Current Densities .....	58
3.1 Time-Reversal Symmetric (TRS) Nonlinearities .....	60
3.1.1 Introduction .....	60
3.1.2 Algorithm for Extracting $J_{NL}$ from Experimental Data.....	62
3.2 Time-Reversal Symmetry-Breaking (TRSB) Nonlinearities .....	67
3.2.1 Introduction .....	67
3.2.2 Algorithm for Extracting $J_{NL}'$ from Experimental Data .....	69

3.3 Predicted harmonics and measured harmonics: coupling and amplification issues ..	70
3.3.1 Analytical Model of Loop/Sample Interactions Calculated by Mathematica™ ..	71
3.3.2 Numerical Simulation using the High Frequency Structure Simulator (HFSS) ..	73
3.3.3 Estimations of the Figures of Merit: $\Gamma$ and $\Gamma'$ ..	75
3.3.4 Estimations of the Probe/Sample Coupling ..	78
3.3.5 Estimations of Attenuation and Amplification in the Microwave Circuit ..	83
4. Microwave Nonlinearities of the YBCO Bi-crystal Grain Boundary ..	85
4.1 Introduction ..	85
4.2 Sample ..	87
4.3 Spatially Resolved Measurement – 1D and 2D measurements ..	91
4.4 Modeling the Origins of Second and Third Harmonic Generation in the Bi-crystal Grain Boundary ..	94
4.4.1 Uncoupled ERSJ Model Solved by Mathematica ..	96
4.4.2 Coupled ERSJ Model by WRSpice® ..	99
4.5 Vortex Dynamics Discussion with WRSpice® Simulations ..	102
4.5.1 Oates' ERSJ calculation ..	103
4.5.2 Vortex Dynamics in Our YBCO Bi-crystal Grain Boundary ..	106
4.6 Extraction of $J_{NL}$ from the Data ..	108

4.7 Conclusion .....	109
5. Doping Dependent Nonlinearities in HTSC – System and Sample Characterization....	111
5.1 Experimental Setup and Sample Description .....	112
5.1.1 Brief review of the microscope.....	112
5.1.2 Samples .....	113
5.1.3 Field dependent $P_{2f}$ and Importance of the Magnetic Shielding Assembly .....	115
5.1.4 Determination of the doping level of $\text{YBa}_2\text{Cu}_3\text{O}_{7-\delta}$ .....	123
5.2 Doping-dependent quantities in HTSC .....	123
5.2.1 London Penetration Depth.....	124
5.2.2 Zero-Temperature Condensation Energy .....	125
5.3 Mechanisms of nonlinear response in under-doped YBCO.....	127
5.3.1 Background nonlinearity of the experimental apparatus .....	127
5.3.2 Granularity and weak links .....	129
5.3.3 TRSB Physics.....	130
5.3.4 Tests to distinguish which model is most viable.....	131
6. Doping Dependent Nonlinearities in HTSC – Discussion of 2 <sup>nd</sup> and 3 <sup>rd</sup> Harmonic Data .....	133
6.1 Magnitude of $P_{3f}$ varies with doping levels .....	134

6.1.1 Fitting and Temperature Normalization of the $P_{3f}(T)$ Measurements .....	135
6.1.2 Extraction of $J_{NL}$ from the $P_{3f}$ data .....	141
6.1.3 Note on the choice of $\lambda(x, T)$ .....	146
6.2 The unusual $P_{2f}$ peak seen near $T_c$ in all under doped films.....	147
6.2.1 Extraction of $J_{NL}'$ from $P_{2f}$ data .....	149
6.3 Power dependence measurements of $P_{2f}$ and $P_{3f}$ .....	155
6.4 Conclusion .....	159
7. Summary and Future Work .....	161
7.1 Summary .....	161
7.2 Future Work.....	163
7.2.1 Sensitivity to the Nonlinearities.....	164
7.2.2 Spatial Resolution .....	167
7.3 Conclusion .....	173
APPENDIX A Fourier transforms used in data analysis and model calculations.....	175
APPENDIX B How to use wrspice <sup>®</sup> software?.....	179
REFERENCES .....	188

## LIST OF TABLES

Table 2.1 Summary of Yip and Sauls' predictions of NLME.....	40
Table 2.1 Summary of expected experimental signatures of the NLME.....	42
Table 3.1 Important dimensions of simulated coaxial cables.....	73
Table 3.2 Simulated figures of merit and coupling coefficient by analytical and HFSS models for different probe sizes.....	82
Table 5.1 Summary of oxygen-doped YBCO thin film samples.....	114
Table 5.2 Summary of the measurements of $\lambda$ on YBCO ceramics, thin films, and single crystals.....	125
Table 6.1 Summary of the fitting parameters used in the Ginzburg-Landau model for $P_{3f}(T)$ near $T_c$ for most of my samples.....	137
Table A.1 Fourier coefficients in Eq. A.3 calculated via Eq. A.4.....	176

## LIST OF FIGURES

Fig. 1.1 Different classes of near-field microwave microscopes. ....	3
Fig. 1.2 Schematic of the permeability imaging near-field microwave microscope. ....	7
Fig. 1.3 Equivalent circuit model of the probe/sample coupling. ....	8
Fig. 1.4 The schematic of electric probe and magnetic loop probe, and arrangement of metallic tapes while taking line-scan data. ....	11
Fig. 1.5 A line scan of $\Delta f$ and $Q$ across the ferromagnetic and paramagnetic metal glass tapes using an electric probe. ....	13
Fig. 1.6 A line scan of $\Delta f$ and $Q$ across the ferromagnetic and paramagnetic metal glass tapes using a loop probe. ....	14
Fig. 1.7 Distance dependence of the frequency shift and $Q$ factor measured at different frequencies. ....	16
Fig. 1.8 FMR phenomenon observed in the microwave microscope on a LSMO single crystal in $\Delta f(H)$ and $Q(H)$ measurements using the magnetic loop probe. ....	19
Fig. 1.9 Images of variations in $\Delta f$ and $Q$ demonstrating the variation in the FMR field. ...	21
Fig. 1.10 Schematic of the nonlinear near-field microwave microscope. ....	25
Fig. 1.11 Pictures of the microscope. ....	26

Fig. 2.1 Schematics of the GL calculation performed by Gittleman <i>et. al.</i> .....	34
Fig. 2.2 Fermi surfaces of s-wave and d-wave superconductors.....	38
Fig. 2.3 Calculation of $b_{\mathcal{C}}(T)$ for s-wave and d-wave superconductors. ....	41
Fig. 2.4 $P_{3f}(T)$ measured on an unpatterned NbN thin film near the $T_c \sim 10.5\text{K}$ .....	45
Fig. 2.5 Schematic of the formation of Andreev bound state.....	49
Fig. 3.1 Schematic of the expected $J_{NL}(T)$ for various nonlinear mechanisms in HTSC. ....	62
Fig. 3.2 Schematic of the integral for estimation of the inductance per unit length.....	63
Fig. 3.3 Schematic of the ideal-circular-loops model.....	72
Fig. 3.4 Setup in HFSS to simulate the probe/sample interaction.....	75
Fig. 3.5 Microwave current distribution $ K $ (A/m) simulated by HFSS. ....	77
Fig. 3.6 The configuration of two circular loops for the idea-loop model.....	78
Fig. 3.7 Setup for estimating the coupling coefficient $M/L_{loop}$ using HFSS. ....	80
Fig. 3.8 Plot of $\Gamma$ and $\Gamma'$ calculated by both the analytical model and HFSS. ....	83
Fig. 4.1 $P_{3f}(T)$ measured above and away from the YBCO bi-crystal gain boundary. ....	88
Fig. 4.2 Power dependence of $P_{2f}$ and $P_{3f}$ signals measured above and away from the bi-crystal grain boundary at 60K.....	90
Fig. 4.3 A line-scan of $P_{2f}(X)$ and $P_{3f}(X)$ across the bi-crystal grain boundary. ....	92

Fig. 4.4 Spatially resolved 2D images of $P_{2f}$ and $P_{3f}$ containing the YBCO bi-crystal grain boundary. ....	93
Fig. 4.5 Schematic of the un-coupled ERSJ model. ....	97
Fig. 4.6 Coupled and uncoupled ERSJ model calculations compared with the experimental $P_{2f}$ and $P_{3f}$ data.....	99
Fig. 4.7 Schematic of the coupled ERSJ model simulated by WRSpice <sup>®</sup> .....	101
Fig. 4.8 Trajectories of vortices simulated by Oates' group. ....	104
Fig. 4.9 Trajectories of vortices in one RF cycle simulated for Oates' setup.....	105
Fig. 4.10 WRSpice <sup>®</sup> simulation for vortex dynamics in the grain boundary. ....	107
Fig. 4.11 The extracted $J_{NL}(X)$ from the $P_{3f}(X)$ experimental data in Fig. 4.3.....	109
Fig. 5.1 $\text{Im}(\chi)$ measured from samples with different doping levels.....	115
Fig. 5.2 $P_{2f}(T)$ and $P_{3f}(T)$ of an optimally doped YBCO thin film (MCS1). ....	117
Fig. 5.3 The effect of external magnetic fields on $P_{2f}$ . ....	119
Fig. 5.4 Magnetic shielding assembly made by Amuneal.....	121
Fig. 5.5 Harmonic measurements of different samples taken after installation of the magnetic shielding assembly. ....	122
Fig. 5.6 Zero-temperature condensation energy density and $T_c$ of Ca doped YBCO. ....	126
Fig. 5.7 $P_{2f}$ and $P_{3f}$ generated by the system (background nonlinearity). ....	129



Fig. 6.1 A typical harmonic data of an under-doped YBCO thin film with $T_c \sim 75\text{K}$ . .....	134
Fig. 6.2 Typical $P_{3f}(T)$ data fitted by the Ginzburg-Landau theory. ....	136
Fig. 6.3 $P_{3f}(T)$ data taken from variously doped YBCO thin films without the magnetic shielding assembly. ....	139
Fig. 6.4 $P_{3f}(T)$ data taken from variously doped YBCO thin films with the magnetic shielding assembly. ....	140
Fig. 6.5 Linear fit of $\lambda(T=0)$ versus the doping level $x$ . ....	142
Fig. 6.6 $J_{NL}(0.97T_c)$ converted from the same set of $P_{3f}$ data taken with/without the magnetic shielding assembly on variously doped YBCO thin films. ....	144
Fig. 6.7 $P_{2f}(T)$ data near $T_c$ normalized by the $T_c$ 's of the oxygen-doped samples. ....	148
Fig. 6.8 $J_{NL}'$ at $0.97T_c$ extracted from $P_{2f}(T)$ data of variously doped YBCO thin films. ..	150
Fig. 6.9 $J_{TRSB}$ vs. $T/T_c(ac)$ for variously doped YBCO thin films. ....	152
Fig. 6.10 $P_{2f}(P_f)$ and $P_{3f}(P_f)$ of MCS4, and $P_{2f}(P_f)$ and $P_{3f}(P_f)$ of MCS1 near $T_c$ taken without the magnetic shielding assembly. ....	157
Fig. 6.11 $P_{2f}(P_f)$ and $P_{3f}(P_f)$ of degraded YBCO thin films. ....	158
Fig. 6.12 $P_{2f}(P_f)$ and $P_{3f}(P_f)$ of MCS2 taken with the magnetic shielding assembly. ....	159
Fig. 7.1 Schematic of a patterned loop probe on a sapphire substrate. ....	166
Fig. 7.2 The extension of z-piezo as a function of input microwave power. ....	168

Fig. 7.3 Schematic of the re-entrant cavity. .... 170

Fig. 7.4 STM topography image of a 200nm thick c-axis YBCO film on a STO 30° mis-oriented bi-crystal substrate. .... 172

Fig. 7.5 Simultaneously taken harmonic data with STM imaging..... 173

## GLOSSARY

**1D, 2D.** One dimensional, two dimensional

**AC.** Alternating current

**ABS.** Andreev bound state

**APS.** American Physical Society

**BCS.** Bardeen-Cooper-Schrieffer

**CMR.** Colossal Magneto-Resistance

**dBm.** Logarithmic scale of power: power in dBm =  $10 \times \text{Log}_{10}(\text{power in mW})$

**DOS.** Density of State

**ERSJ.** Extended Resistively Shunted Josephson Junction

**FFC.** Frequency Following Circuit

**FMR.** Ferromagnetic Resonance

**GB.** Grain boundary

**GL.** Ginzberg-Landau

**HFSS.** High-Frequency Structure Simulator

**HTSC, HTS.** High-Temperature Superconductors

**J.** Current density ( $\text{A/m}^2$ )

**J<sub>NL</sub>**. Nonlinear scaling current density (A/m<sup>2</sup>)

**J<sub>TRSB</sub>**. Current density of spontaneous currents generated by TRSB nonlinearities (A/m<sup>2</sup>)

**K**. Surface current density (A/m)

**L**. Self-inductance

**LPS**. Laboratory for Physical Science

**LSMO**. La<sub>0.8</sub>Sr<sub>0.2</sub>MnO<sub>3</sub>

**M**. Mutual inductance

**MCS**. Label of samples made by Matt. Sullivan

**NGO**. NdGaO<sub>3</sub>

**NL**. Nonlinear; Nonlinearity

**NLME**. Nonlinear Meissner effect

**P<sub>f</sub>**. Power of the fundamental tone

**P<sub>2f</sub>**. Power of the second harmonic generation

**P<sub>3f</sub>**. Power of the third harmonic generation

**P<sub>IMD</sub>**. Power of the intermodulation distortion

**PLD**. Pulsed Laser Deposition

**Q**. Quality factor of a microwave resonator

**QCP**. Quantum critical point

**RF.** Radio frequency

**SNMM.** Scanning Near-field Microwave Microscope

**SQUID.** Superconducting Quantum Interference Device

**STO.** SrTiO<sub>3</sub>

**t.** Time; also used as thickness of films

**T.** Temperature

**T<sub>c</sub>.** Critical temperature of superconducting phase transition

**TRS.** Time-Reversal Symmetric

**TRSB.** Time-Reversal Symmetry Breaking

**UD.** Under-doped

**VAV.** Vortex-Anti-Vortex

**WRSpice.** Superconducting circuit simulation software developed by Whitely Research Inc.

**YBCO.** YBa<sub>2</sub>Cu<sub>3</sub>O<sub>7-δ</sub>

**ZBCP.** Zero-biased conductance peak

**$\Delta f$ .** Frequency shift of a microwave resonator

**$\mu$ -SR.** Muon spin relaxation

**$\tau$ .** Reduced temperature normalized by the critical temperature of superconductors

# CHAPTER 1

## INTRODUCTION TO THE NONLINEAR NEAR-FIELD MICROWAVE MICROSCOPE

### 1.1 Introduction

Traditional microwave measurements of electromagnetic properties of materials are done on the length scales of centimeters, which is the free-space wavelength of microwave signals. The earliest microwave measurement on superconductors was done by Pippard [1] using a superconducting microwave resonator. In this measurement, however, what was measured was an averaged property along the sample, weighted by the standing-wave pattern in the resonator.

Later refinements of this technique utilized the cavity perturbation method, in which the sample is placed in a small region of relatively uniform magnetic or electric field in a large (compared to the sample) electromagnetic cavity. The properties of the sample are obtained by comparing the change of the resonant frequency and quality factor of the resonator in the presence and absence of the sample. However, the measured quantities are still averaged over the sample, weighted by the distribution of fields or currents on the sample.

The interpretation of these results is only simple in the case of a homogeneous sample with ellipsoidal geometry.

Other resonant or non-resonant techniques are used in far-field microscopy, but the spatial resolution is limited to a few centimeters ( $\sim$  microwave wavelength), and large screening currents are generated, especially near the edges, by globally applying fields to the sample. This means that such techniques only study the nonlinearities from the edges and corners, which are dominated by extrinsic nonlinear mechanisms, e.g. boundaries and defects. This is why near-field microscopy becomes an important approach for studying local electromagnetic properties of materials.

Near-field microwave microscopy is a state-of-the-art technique established over many years by various research and industrial groups. In principle, Synge should probably be credited as the intellectual founder of near-field microscopy, based on his work in 1928 [2]. However, the earliest high-resolution quantitative microwave measurements were performed by the ferromagnetic resonance community [3,4]. The most important advantages of near-field microscopy are the superior spatial resolution, and sensitivity to local electromagnetic properties.

Unlike far-field microscopy, the limit of the spatial resolution is no longer set by the wavelength of the microwave signals, but the geometry of the near-field microscope. Figure 1.1 shows some typical classes of near-field microscopes discussed in Ref. [5].

Generally, near-field microwave microscopy can work in both resonant (Fig. 1.1(a) and (c)) and non-resonant mode (Fig. 1.1(b), (d) and (e)). Fig. 1.1(a) shows a resonant cavity, which is coupled to a sample by an evanescent mode through a small hole (the aperture) on the cavity wall. The evanescent wave is locally applied to the sample, and the perturbation to the cavity due to the sample is measured through the shift in resonant frequency and change in quality factor  $Q$  of the cavity. Images of local properties can therefore be taken while scanning the sample under the hole. The spatial resolution is determined by the larger of the size of the aperture and the sample/cavity separation, which can be much smaller than the wavelength.

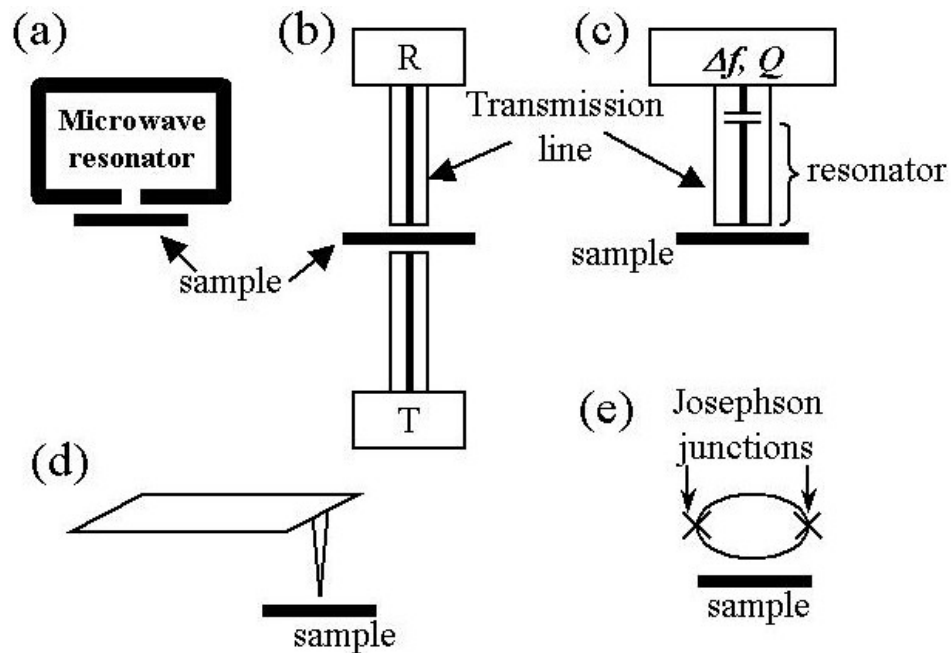


Fig. 1.1 Different classes of near-field microwave microscopes. Illustrations are taken from Ref. [5].



The same principle is used in Fig. 1.1(c), which has a section of coaxial transmission line or a resonator, decoupled from the rest of the microwave circuit by a capacitor (or inductor). Samples are placed very close to the end of the coaxial cable (the probe), and perturb the resonator. The locality is determined by the larger of two dimensions: the diameter of the inner conductor of the probe, and the separation between the probe and the sample. In this case, the type of probe/sample interaction can vary depending on the desired contrast mechanism. For example, the magnetic permeability imaging microwave microscope [6], which will be discussed later in this chapter, is in this category, but uses a shorted loop probe, which enhances its magnetic coupling to the sample.

Fig. 1.1(b) is a version of (c), in which there is no resonator. Microwave signals are sent to the sample and can be picked up after reflection from or transmission through the sample. The nonlinear microwave microscope [7], which is used for most of my work and will be discussed later, is in this category, operating in the reflection mode. Figure 1.1(e) shows the scanning microwave SQUID microscope [8], which uses a Superconducting QUantum Interference Device as a passive detector of the local magnetic fields. Such a microscope normally works in a narrow frequency band on the order of hundreds of kHz. Efforts to make broadband SQUID microscopes are in progress. Finally, Fig. 1.1(d) illustrates the advantage of the extremely high spatial resolution of scanning probe microscopy that utilizes very sharp tips (e.g. STM, AFM, etc.). Microwave signals are sent through the tip/sample coupling, which is controlled by independent means while scanning

[9]. However, making the microwave system work independently from the coupling-control mechanism is a difficult task.

In the remainder of this chapter, I demonstrate my work in permeability and ferromagnetic resonance imaging using a near-field microwave microscope in resonant mode [6], and the nonlinear near-field microwave microscope [7], which I used later in studying the local nonlinearities of superconductors.

## 1.2 Ancestor of the Nonlinear Near-Field Microwave Microscope: The Permeability Imaging Near-Field Microwave Microscope

### 1.2.1 Introduction

The extraordinary increase in the density of magnetic storage media and the access speeds of read/write heads has led to an increased interest in measuring local microwave magnetic properties of materials on short length scales. It is also of interest to evaluate the homogeneity of magnetic properties of samples, such as the local Curie temperature, magnetization, and microscopic phase separation into magnetic and nonmagnetic regions. Many techniques exist to measure the global microwave permeability or susceptibility of materials [10]. Progress has also been made in scanning microscopes which are designed to image radio frequency magnetic fields [8,11,12], electron paramagnetic resonance [13], and ferromagnetic resonance (FMR) [3,14,15,16]. However, few of these techniques measure microwave permeability on sub-mm length scales [17,18].

To fulfill this need, we have developed a technique for measuring local permeability using a scanning near-field microwave microscope (SNMM). Previously, the SNMM has been used to image conductivity [19] and dielectric properties [20] of materials with an open-ended tip probe, which has a maximum electric field and minimum magnetic field at the probe end, thus enhancing the electric coupling but minimizing the magnetic coupling. In this section, I discuss the utilization of a shorted loop probe, which couples magnetically, instead of electrically, to a sample.

### 1.2.2 Experimental Setup

Our SNMM is a driven resonant coaxial transmission line connected to a semi-circular loop formed by shorting the inner conductor of a coaxial cable to the outer conductor. Both inner and outer conductors are made of Cu, so that no magnetic materials interfere with the magnetic coupling between the probe and sample. We use a frequency following circuit (FFC) [21] designed in our group, and a lock-in amplifier in a feedback loop to lock to one of the resonant frequencies of the coaxial resonator (Fig. 1.2). We then monitor the frequency shift,  $\Delta f$ , due to perturbations from the sample, which is scanned under the probe. By modulating the microwave frequency of the source and monitoring twice the modulation frequency, the losses in the sample contributing to the  $Q$  factor of the resonator can be measured as well. Details of this microscope and how to determine the sample properties from the frequency shift and  $Q$  factor can be found in Refs. [19-22].

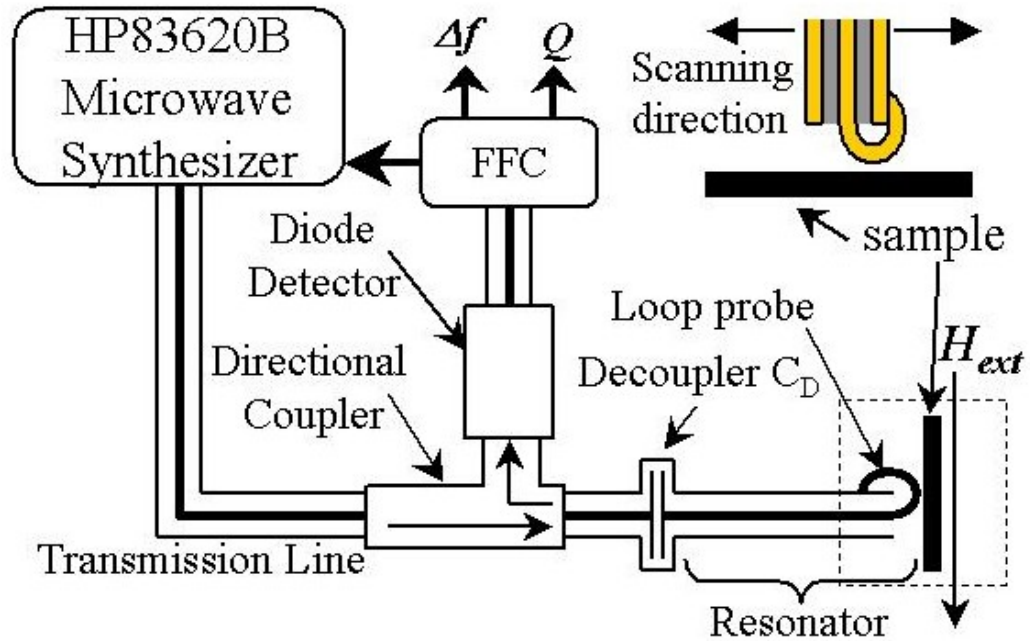


Fig. 1.2 Schematic of the permeability imaging near-field microwave microscope.

We use the same transmission line model established by David Steinhauer [21] to understand the observed changes in the resonant frequency and quality factor. However, since I use a different type of probe than Steinhauer's, the probe/sample coupling mechanism and the effective load impedance are different. To properly describe my system, I use the equivalent circuit shown in Fig. 1.3 in the transmission line model to represent the probe/sample coupling and how the load impedance affects the characteristics of the transmission line resonator. The loop probe is represented as an inductor  $L_0$ , the test material as a series combination of its effective inductance  $L_X$  and complex impedance  $Z_X = R_X + iX_X$ , and the coupling as a mutual inductance  $M$ . For materials with good

enough conductance so that the microwave skin depth is much smaller than the sample thickness, we model the sample inductance by an identical image of the loop probe, so that  $L_X = L_0$ . The self-inductance of the loop probe is roughly estimated as  $L_0 \approx 1.25\mu_0 a$  [23], assuming a circular loop with inner diameter  $a \cong$  wire thickness = 200  $\mu\text{m}$ . In this case,  $L_0 \cong 3.14 \times 10^{-10} \text{ H}$ .

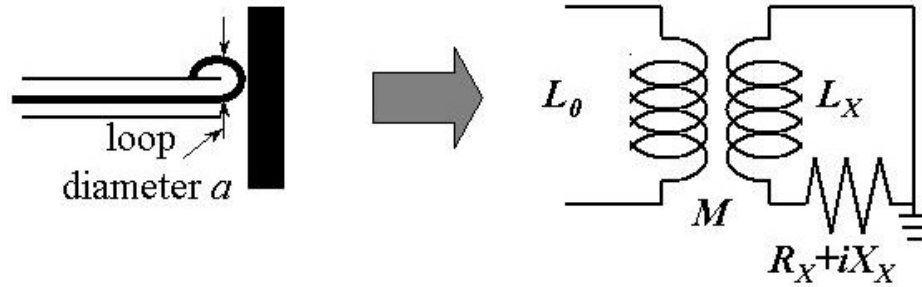


Fig. 1.3 Equivalent circuit model of the probe/sample coupling.

In the high frequency limit, the surface impedance of the sample can be written as

$$Z_X = \sqrt{i\mu_0\mu_r\omega\rho}, \quad (1.1)$$

where  $\mu_r$  is the complex relative permeability of the material,  $\omega$  is the microwave angular frequency, and  $\rho$  is the resistivity of the material, which is considered to be independent of  $\mu_r$ , and real.

Although the mutual inductance  $M$  can be estimated analytically by calculating the two-circular-loop model, it is merely a rough approximation of the real geometry. Therefore, when we first built this microscope, we had to treat the value of  $M$  as a fitting parameter.

From the analytical two-circular-loop model, we know  $M \approx 10^{-12} - 10^{-11}$  H, as will be discussed in Chapter 3. The microwave resonator of our microscope is a transmission line that is capacitively coupled to a microwave source. The frequency shift and  $Q$  are calculated using microwave transmission line theory, which is described in detail in Ref. [21].

In the typical operating frequency range (e.g.  $f = 6.5$  GHz), we can take  $\omega L_0 \sim 2\pi \times 6.5 \times 10^9 \times 3 \times 10^{-10} \approx 12.3\Omega$  to be much greater than the sample impedance  $|Z_x| = \sqrt{\mu_0 \mu_r \omega \rho} \sim \sqrt{4\pi \times 10^{-7} \times 5 \times 2\pi \times 6.5 \times 10^9 \times 200 \times 10^{-8}} \approx 0.7\Omega$ , taking  $\mu_r = 5$  and  $\rho = 200\mu\Omega cm$  typical of our samples. From the equivalent circuit shown in Fig. 1.3, we find that the load impedance presented by the probe and sample is

$$Z_{Load} \cong i\omega L_0(1 - k^2) + k^2(R_x + iX_x), \quad (1.2)$$

where the coupling coefficient  $k = M/\sqrt{L_0 L_x}$  is a purely geometrical factor, and  $R_x + iX_x = Z_x$  is the surface impedance of the sample. From the transmission line model, we know that to a good approximation, the frequency shift is produced by the imaginary part of  $Z_{Load}$ , while the real part of  $Z_{Load}$  determines the  $Q$  of the microscope.[21]

### 1.2.3 Samples

The samples we studied are two metallic glass tapes, made of  $Fe_{40}Ni_{40}P_{14}B_6$  and  $Fe_{32}Ni_{36}Cr_{14}P_{12}B_6$ , and a  $La_{0.8}Sr_{0.2}MnO_3$  (LSMO) single crystal. The difference in

composition of the metallic glass tapes makes the former ferromagnetic (FM) and the latter paramagnetic (PM) at room temperature, although both have the same resistivity  $\rho = 150\mu\Omega cm$ . This ensures that any difference observed in  $\Delta f$  and  $Q$  signals with the microwave microscope are due solely to the difference in permeability. This is important since the microscope may also be sensitive to the conducting properties of materials.

LSMO is a colossal magneto-resistive material, whose Curie temperature is  $T_C = 305.5K$ . This sample had been studied extensively by Dr. Andrew Schwartz [24] in our group, and exhibits ferromagnetic resonance (FMR) below  $T_C$ . I wanted to use the FMR phenomenon in this sample to test the ability of my microscope to measure local magnetic properties.

#### 1.2.4 Results of Permeability Imaging

To find the sensitivity of the loop probe to magnetic properties, I measured the metallic glass tapes with both the electric (open-ended) and loop probes as shown in Fig. 1.4.

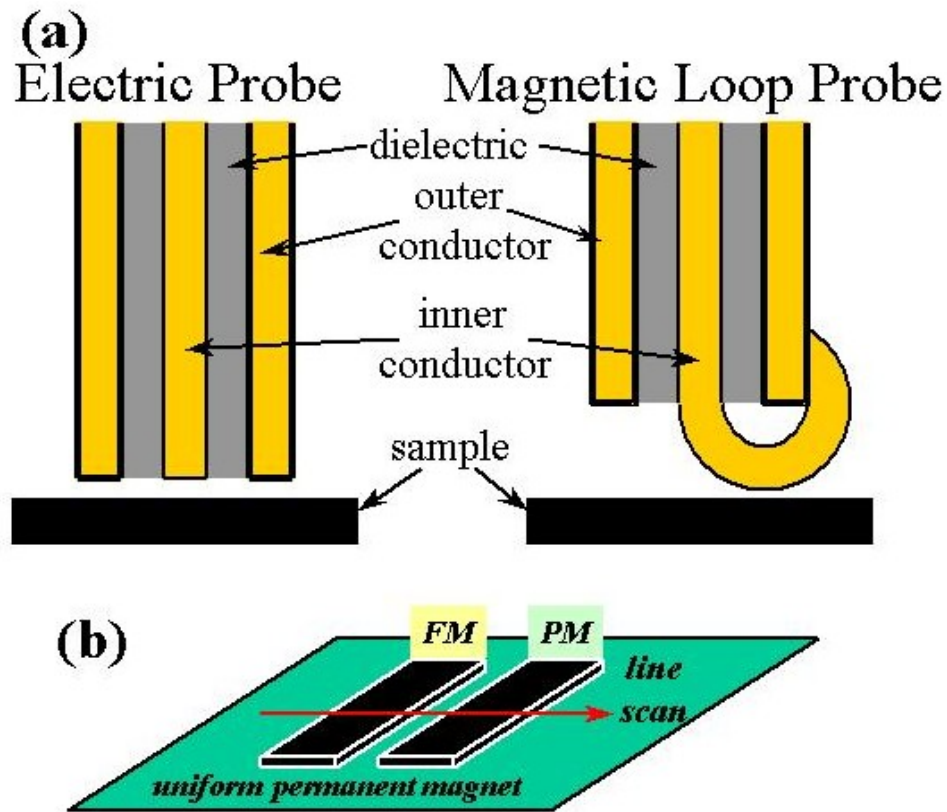


Fig. 1.4 (a) Schematic of electric probe and magnetic loop probe. (b) Arrangement of metallic tapes while taking line-scan data. The ferromagnetic tape was magnetized vertically.

From prior work in our group, we know that for a sample with uniform and homogeneous electrical properties (i.e. dielectric constant, resistivity, etc.), the variations in  $\Delta f$  and  $Q$  signals of the microscope with an electric probe represent the change of topography, which determines the coupling between the samples and probe while the probe is scanning on a horizontal plane. Despite the fact that the tapes have slightly different thickness, which appears as different height, the measurement on the tapes with the electric probe is essentially indistinguishable in both  $\Delta f$  and  $Q$  (see Fig. 1.5). It is noted that the



oscillating features in both  $\Delta f$  and  $Q$  are likely due to the lateral and longitudinal standing wave patterns in the strip samples. These patterns were investigated previously by David Steinhauer [21].

Next, I simply changed the probe tip on the microscope and re-measured the tapes. With the loop probe, the ferromagnetic tape gave a strong reduction in the  $Q$ , whereas the  $\Delta f$  data remained indistinguishable between the ferro- and paramagnetic tapes (Fig. 1.6). It is worth noting that the frequency shift data shows opposite trends in the electric probe and magnetic probe measurements. This is because the probes couple to the sample differently. The electric probe couples to the sample capacitively, which leads to an effective lengthening of the electric length of the resonator and a reduction of the resonant frequency. On the other hand, the magnetic probe couples to the sample inductively, and results in an effective shortening of the electric length of the resonator and higher resonant frequencies.

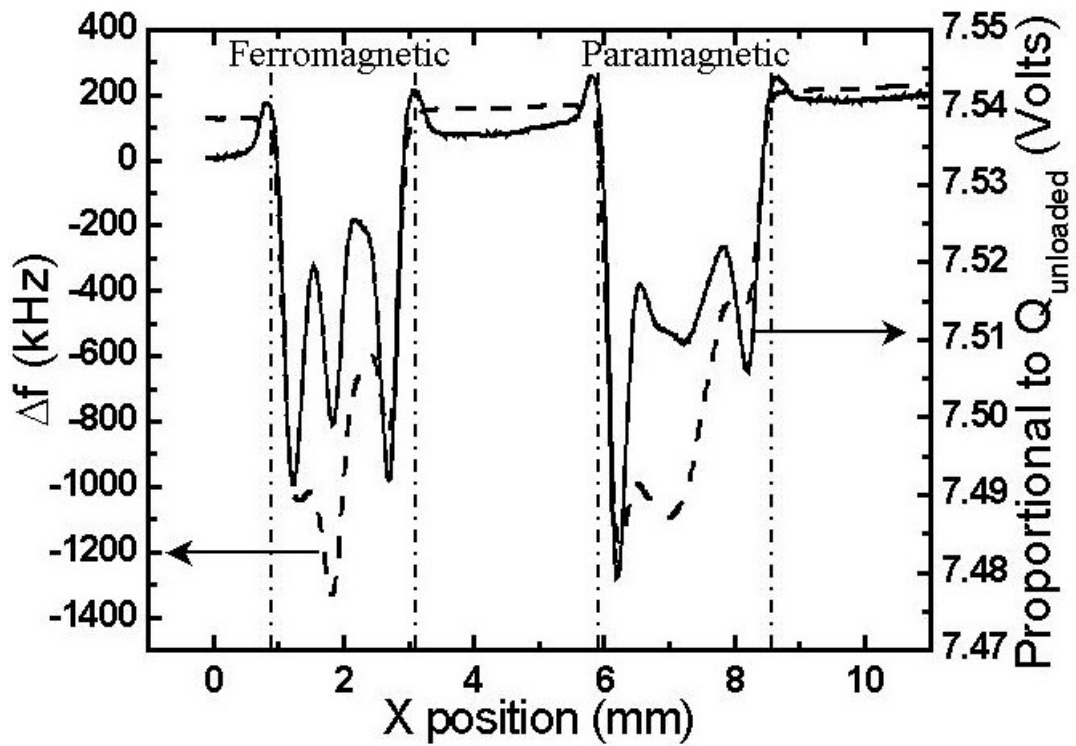


Fig. 1.5 A line scan of  $\Delta f$  (dashed curve) and  $Q$  (solid curve) across the ferromagnetic (left) and paramagnetic (right) metal glass tapes using an electric probe made of an .034" outer diameter coaxial cable, whose inner conductor has diameter  $\sim 200 \mu\text{m}$ .

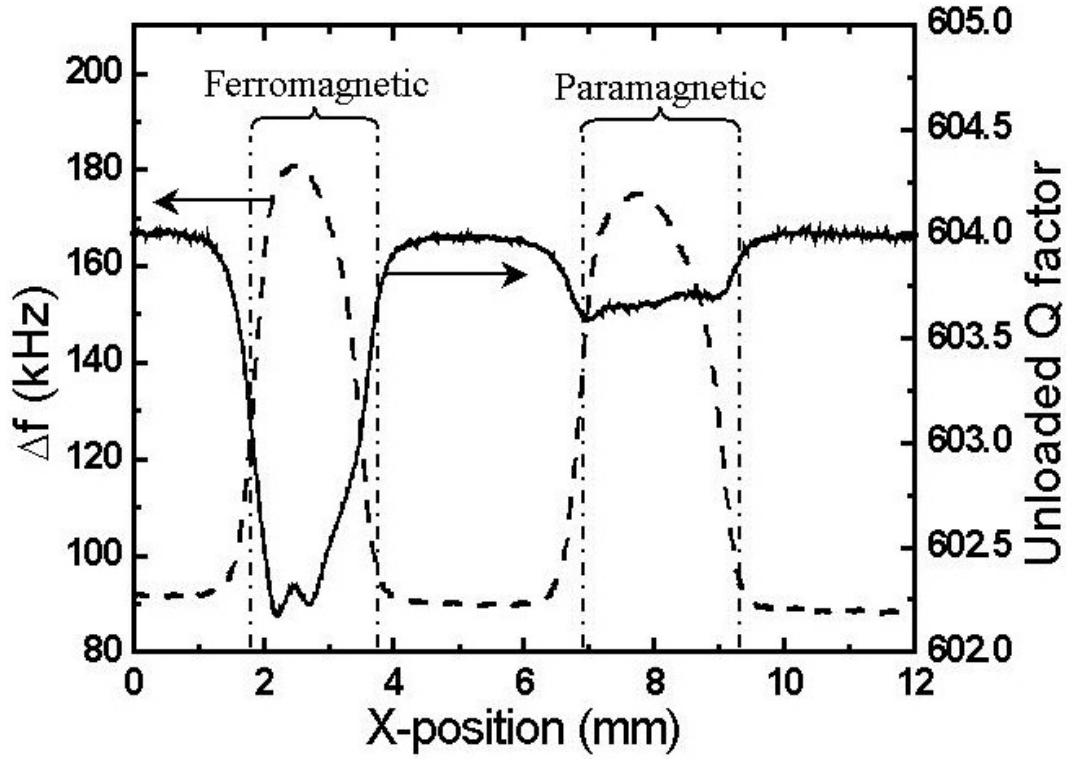


Fig. 1.6 A line scan of  $\Delta f$  (dashed) and  $Q$  (solid) across the ferromagnetic (left) and paramagnetic (right) metal glass tapes using a loop probe made of the same coaxial cable as the electric probe.

To understand the result with a loop probe, we note that the coupling coefficient  $k$  is similar for both materials due to the similar topography of the tapes. Since the imaginary part in the second term in Eq. 1.2 is small, i.e.  $k^2 X_x \ll \omega L_0(1 - k^2)$ , and  $k^2 \ll 1$ , the change of the total imaginary part of  $Z_{Load}$  due to the variation in  $X_x$  is very small in percentage. As mentioned previously,  $\Delta f$  is mostly determined by the imaginary part of  $Z_{Load}$ ; hence we don't expect a clear difference in  $\Delta f$  between the tapes because the difference in  $\mu$  is a very small perturbation. On the other hand, though both  $R_x$  and  $X_x$

change with microwave permeability, the variation in  $R_X$  is measurable for it is the only term determining the real part of  $Z_{Load}$  (Eq. 1.2). Since  $Q$  is mostly determined by the real part of  $Z_{Load}$ , and the tapes have similar  $k$ , the variation in  $R_X$  (due to their different permeability) is revealed in the difference in  $Q$ , consistent with Fig. 1.6. The larger  $\mu$  translates into a larger  $R_X$  in the ferromagnetic tape, accounting for the larger drop in  $Q$ .

As a further test, we measured  $\Delta f$  and  $Q$  versus the probe-sample separation  $h$ , at frequencies of 4.04, 7.08, and 10.34 GHz. We found an increase in  $\Delta f(10\mu m) - \Delta f(500\mu m)$  as the frequency increased, and a decrease in  $Q(500\mu m) - Q(10\mu m)$  (Fig. 1.7). The increase of  $\Delta f(10\mu m) - \Delta f(500\mu m)$  is due to the increase of change in the imaginary part of  $Z_{Load}$  as the frequency is increased (Eq. 1.2). However, the decrease of  $Q(500\mu m) - Q(10\mu m)$  is not so easily understood, and may be dominated by ferromagnetic resonant (FMR) phenomena in  $|Z_x| \propto \sqrt{\mu_r(\omega)\omega}$ .

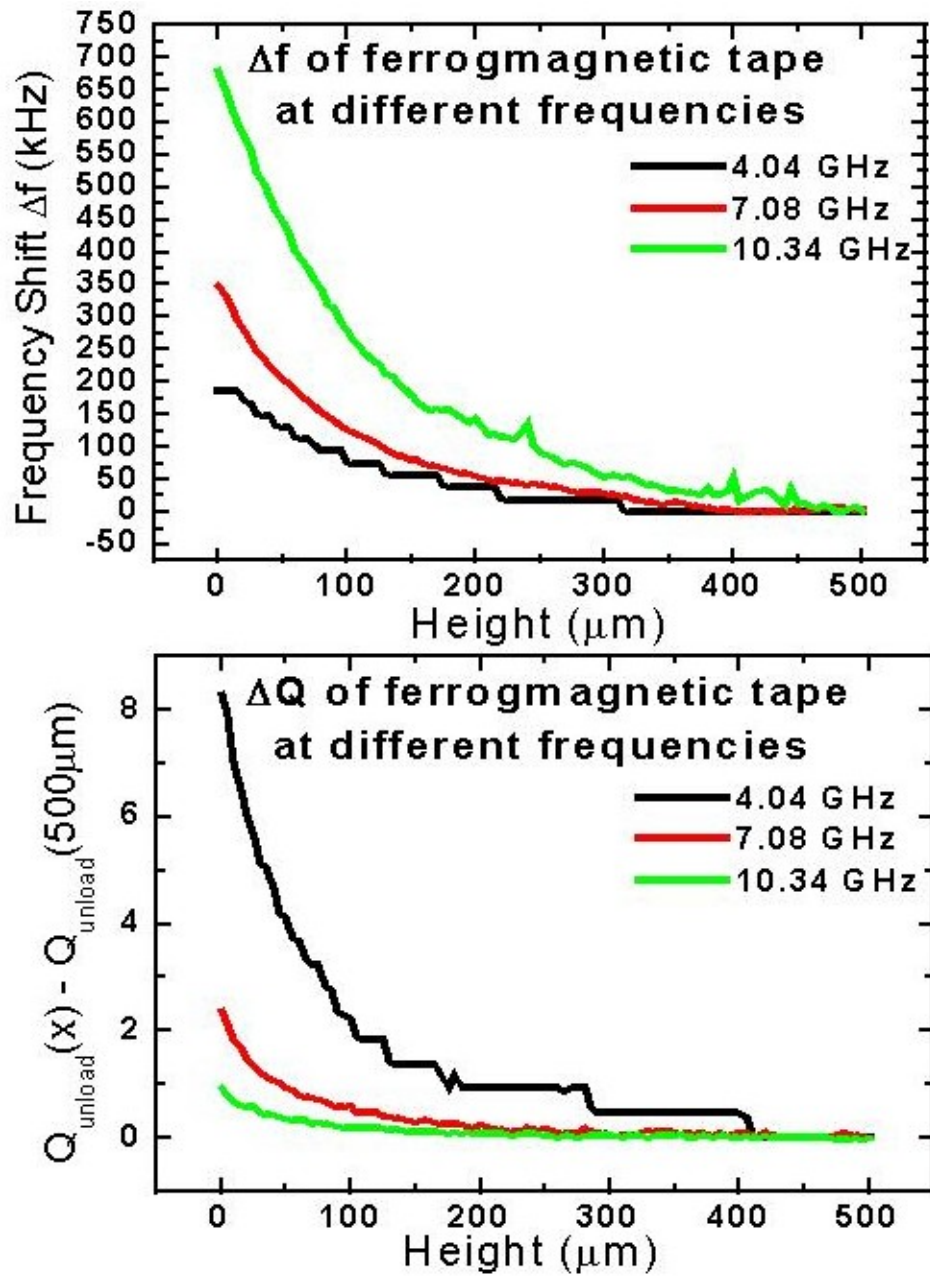


Fig. 1.7 Distance dependence of the frequency shift and  $Q$  factor measured at different frequencies. The step-like feature in 4GHz measurement is due to the setting of the lock-in amplifiers. It was not optimized and gave discrete output.

### 1.2.5 CMR Field Imaging

To quantitatively evaluate our understanding of the microscope, I examined a single crystal of the colossal magneto-resistive material  $\text{La}_{0.8}\text{Sr}_{0.2}\text{MnO}_3$  (LSMO) with diameter  $\sim 2$  mm, in the vicinity of its ferromagnetic resonance (FMR). The probe used in this measurement is made of a non-magnetic coaxial cable with 0.034" outer diameter. The imaging was performed at  $301.500 \pm 0.005$  K, just below the Curie temperature 305.5 K. With the probe positioned  $\sim 20$   $\mu\text{m}$  above the center of the sample, we measured  $\Delta f$  and  $Q$  as a function of the external magnetic field  $H_{ext}$  (Fig. 1.8), and the probing microwave frequency  $\sim 6.07$  GHz. The external magnetic field is applied uniformly by placing the sample in the center of two 5cm diameter magnet poles, which are 1cm apart. The field direction is parallel to the sample surface and the plane of the loop probe (Fig. 1.2). In a separate experiment [24,25], the complex surface impedance of this sample was also measured. The FMR phenomenon is clearly observed as a minimum in  $Q(H_{ext})$  and a point of maximum slope of  $\Delta f(H_{ext})$  (see Fig. 1.8).

We can compare the measured  $\Delta f$  and  $Q$  versus  $H_{ext}$  of LSMO with model predictions based on the independently measured complex surface impedance and permeability on the same sample. In our model, the  $\mu_r$  dependence only appears in the surface impedance  $Z_X$ . To test whether or not this model properly describes the experiment, we evaluated the transmission line model with the measured  $Z_X$ . It is known from David Steinhauer's work [19-21] that the decoupler capacitance  $C_D \approx 10^{-13}$  F (see Fig. 1.2). According to my

calculation, which is discussed in later chapters,  $L_0 \sim 10^{-10} - 10^{-9} H$  and  $M \sim 10^{-11} - 10^{-10} H$ , and the resonator cable attenuation  $0.1 < \alpha < 0.2$  nepers/m. However, here I treated them as fitting parameters, since none of them were known exactly. I find that the full model prediction fits the experimental results very well with  $C_D = 2.94 \times 10^{-13} F$ ,  $L_0 = 6.5 \times 10^{-10} H$ ,  $M = 1.3 \times 10^{-10} H$ , and  $\alpha = 0.1967$  nepers/m. The data (open circles) and fit (solid line) are shown together in Fig. 1.8. This demonstrates that we have a good qualitative understanding and reasonable quantitative understanding of how our microscope is sensitive to magnetic permeability.

I have also developed a technique to image the spatial variation of FMR resonant field in a sample by using either the frequency shift or  $Q$  data. In Fig. 1.8, I observe that the field of the minimum  $\Delta f(H)$  correspond to the approximately linear range with the steepest slope of  $Q(H)$  (see the vertical line at  $H_I$ ). When the FMR field (the minimum of  $Q$ ) varies over the sample, the frequencies will shift with location. By fixing the homogenous external field at the minimal  $\Delta f$  (or  $Q$ ) while scanning over the sample, I observe the spatial variation in  $Q$  (or  $\Delta f$ ) due to the shift of the local FMR resonant field. Using the approximate linear relationship  $\Delta f(H_{ext})$  at  $H = H_2$  or  $Q(H_{ext})$  at  $H = H_I$ , I can convert the  $\Delta f$  or  $Q$  images to the variation of the FMR resonant field.

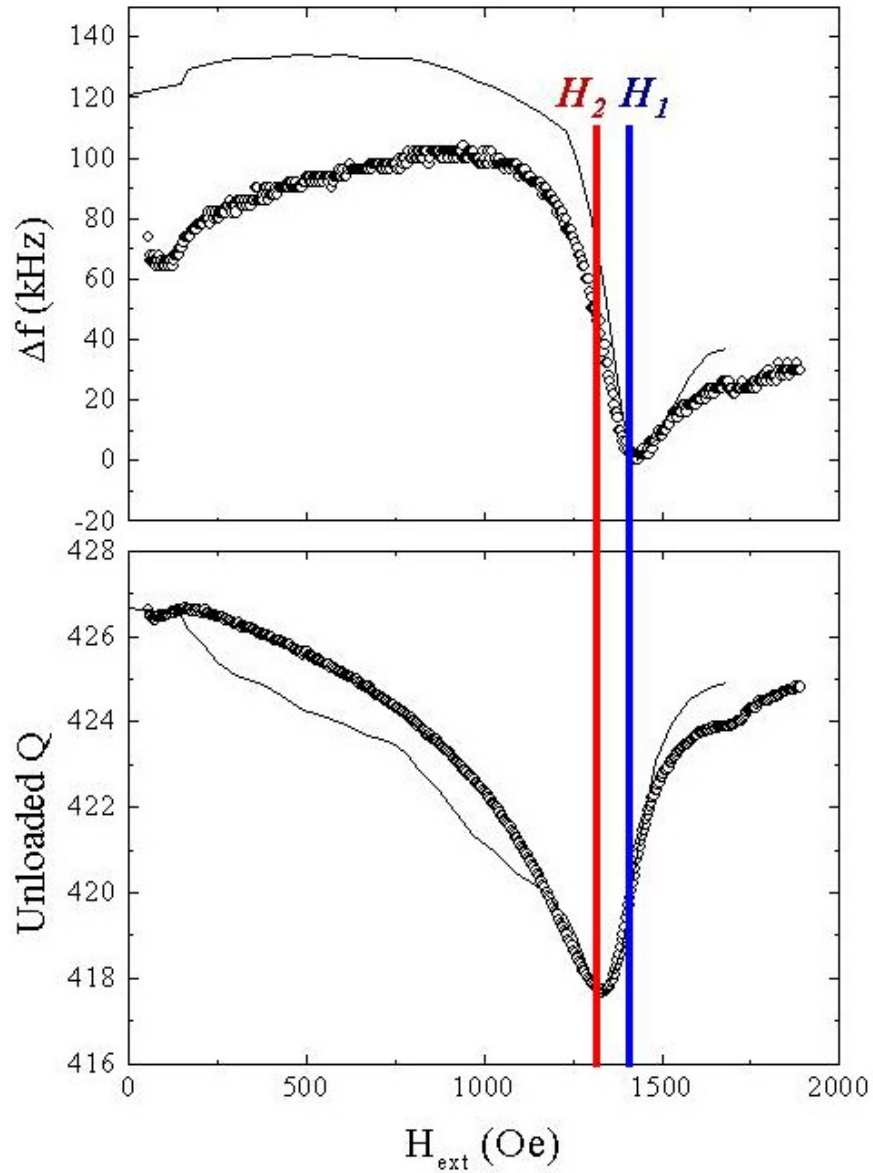


Fig. 1.8 FMR phenomenon observed in the microwave microscope on a LSMO single crystal in  $\Delta f(H)$  and  $Q(H)$  measurements at  $T = 301.5\text{K}$ ,  $f \cong 6.035\text{GHz}$  using the magnetic loop probe. The open circles are the experimental data, and the solid line is the model calculated with parameters and bulk surface impedance data discussed in the text. The solid lines are model calculation based on the field dependent permeability measured by Andy Schwartz.[24, 25] The vertical lines represent the corresponding magnetic fields  $H_1$  and  $H_2$  at which  $\Delta f(H)$  and  $Q(H)$  are minimal.



Figure 1.9 shows  $\Delta f$  and  $Q$  images taken at different fixed external magnetic fields,  $H_{ext} = H_2 \cong 13170e$  and  $H_{ext} = H_1 \cong 14110e$ , corresponding to the minima in  $Q(H_{ext})$  and  $\Delta f(H_{ext})$  measured at the center of the sample simultaneously. The linear relations between  $\Delta f/Q$  and  $H_{ext}$  are obtained from Fig. 1.8:  $|\Delta H_{ext} / \delta(\Delta f)|_{H=H_2} \approx 2.37 Oe / kHz$  and  $|\Delta H_{ext} / \Delta Q|_{H=H_1} \approx 25 Oe / Q$ . While the  $\Delta f$  and  $Q$  images show similar spatial variations, from these linear relations, I also find that the maximum variation of the FMR field in both images is consistent and approximately  $230 Oe$ .

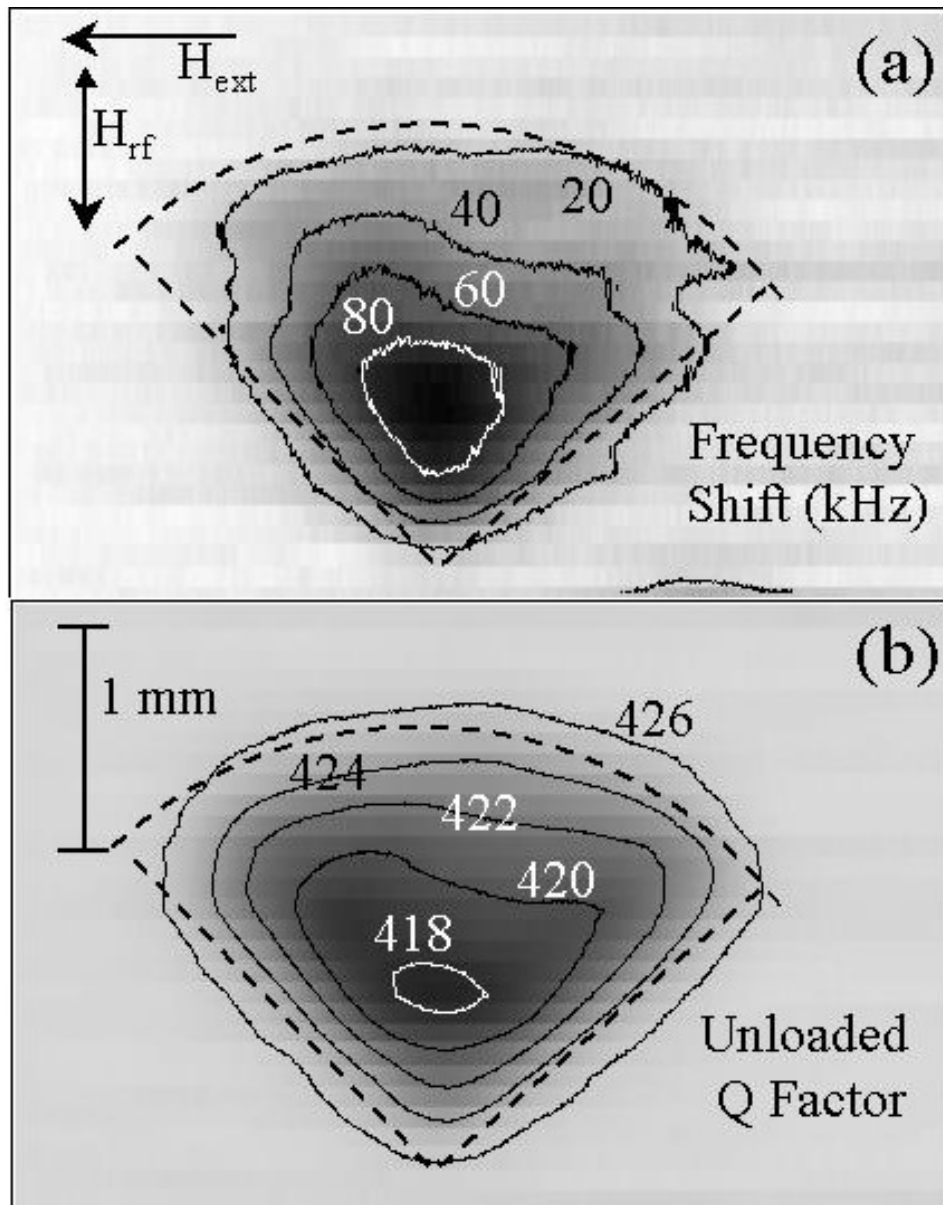


Fig. 1.9 Images of variations in  $\Delta f$  and  $Q$  demonstrating the variation in the FMR field. The dashed line is the outline of sample. The images are taken at 301.5K,  $f \cong 6.035\text{GHz}$ . The external field is  $H_{ext} = H_2 = 1317\text{ Oe}$  in a) and  $H_{ext} = H_1 = 1411\text{ Oe}$  in b). Note that for clarity, not all contour lines are shown.

### 1.2.6 Conclusions

Although the quantitative calibration of this system for measuring local permeability hasn't been accomplished, the sensitivity of this microscope to local permeability is demonstrated by the significant contrast between ferromagnetic and paramagnetic metallic tapes measured by the loop probe. In addition to measuring the local permeability, I extended the use of this microscope to measure local FMR resonant fields in an LSMO single crystal. Qualitative and quantitative understanding of our permeability and FMR data are demonstrated.

## 1.3 The Nonlinear Near-Field Microwave Microscope

### 1.3.1 Introduction

Nonlinear AC properties of superconductors are important for understanding the fundamental physics of superconductors (discussed later in Chapter 2). In microwave measurements, higher harmonics (single-tone input) and intermodulation signals (two-tone input with frequencies very close to each other) are usually observed as a consequence of the nonlinear properties. The prediction of such harmonics also has important implications for applications of superconductors to microwave filters.

The advantages of a microwave microscope employing a resonant technique, as described in the previous sections, are the great amplification of signals in the resonant mode, and the enhanced field intensity at the probe tip. However, the frequency range for

utilizing these advantages is limited due to the narrow bandwidth nature of a resonator. To measure the nonlinear properties of materials without losing these advantages, one can measure the intermodulation distortion (IMD) with two tones,  $f_1$  and  $f_2$ , which are close to each other, applied near the resonant frequency of a superconducting resonator. If the sample is nonlinear, the strongest IMD signals will be generated at  $2f_1-f_2$  and  $2f_2-f_1$ , which are nearby the resonant frequency.

Roughly speaking, IMD measurements are equivalent to measuring the third-order harmonic generation. However, to measure nonlinear properties which generate second order harmonic signals, the IMD technique is not useful, since the corresponding IMD signals are far outside the resonant band. Secondly, all resonant techniques using superconducting transmission line resonators suffer from the problem of strongly enhanced edge screening currents. Since the currents are mostly flowing along the edges of the transmission line to prevent magnetic fields from penetrating into the sample, the nonlinear responses measured by such techniques are mostly from the edge. The large majority of the sample makes essentially no contribution to the measured nonlinear response, and the part that does contribute is damaged and not representative of the bulk.

To identify different types of local nonlinearities, we want to simultaneously and locally measure the second and third harmonic signals in the sample. To do this, we modify the

microscope described in the previous section to work in a non-resonant configuration. This is essentially a change from configurations (c) to (b) in Fig. 1.1.

### 1.3.2 Experimental Setup

Unlike the magnetic microscope discussed in the previous section, this modified version works without the decoupling capacitor, which was used to define a resonator. Therefore, this microscope is not working in the resonant mode.

In this microscope, as shown in Fig. 1.10, microwave signals (generated by the HP83620B Microwave Synthesizer at  $f \cong 6.5 \text{ GHz}$ ) are sent to the sample directly through the probe/sample coupling. Since the microwave synthesizer also generates higher order harmonics, we use two low-pass filters (cutoff frequency  $\sim 8.5 \text{ GHz}$ ) to prevent these harmonic signals from entering the sample. We measure the reflected signals from the surface, which contain higher order harmonics due to the nonlinear properties on the surface. The reflected signals are directed by the directional coupler to the high-pass filters (cutoff frequency  $\sim 12 \text{ GHz}$ ), amplifiers and spectrum analyzer. Since there is a mixer, which is a nonlinear component, in the input of the spectrum analyzer, we would like to minimize the signal at the fundamental frequency ( $\sim 6.5 \text{ GHz}$  in my experiments) getting into the mixer, which could generate higher harmonics. We use two high-pass filters to reduce  $P_f$  significantly ( $> 70 \text{ dB}$ ) without losing signals at the  $2f$  and  $3f$  frequencies. The

signals are amplified by  $\sim 65\text{dB}$  with two microwave amplifiers after being high-pass filtered, and then measured by the spectrum analyzer.

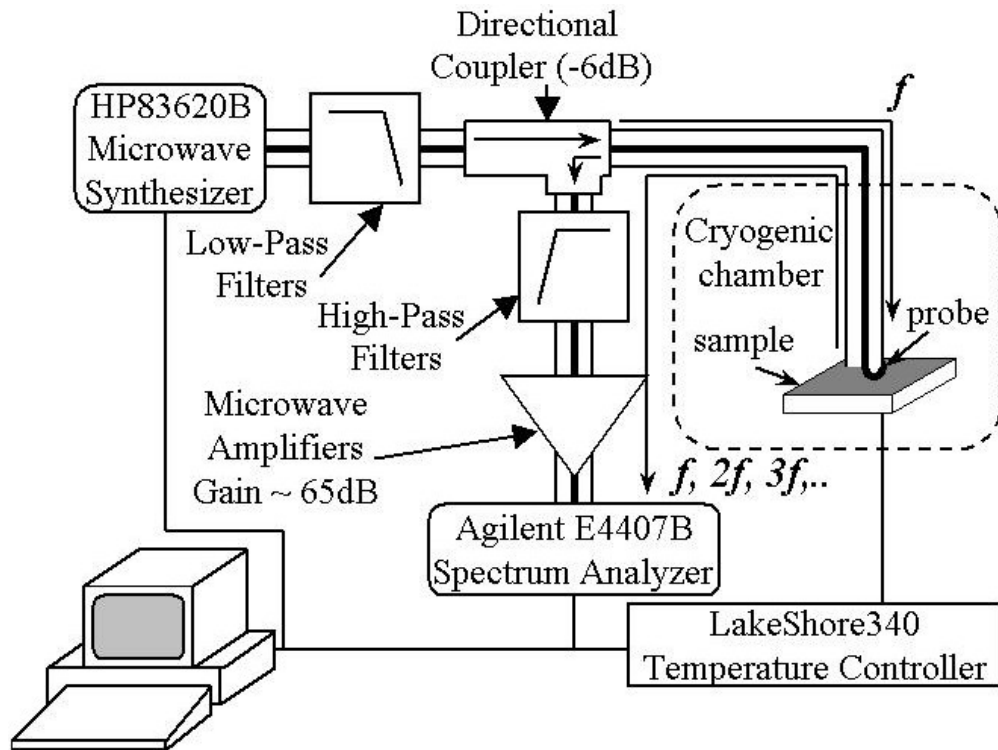


Fig. 1.10 Schematic of the nonlinear near-field microwave microscope.

Shown in Fig. 1.11 are the pictures of my system. Microwave Electronics, the cryogenic chamber, and a picture of the loop probe are shown.

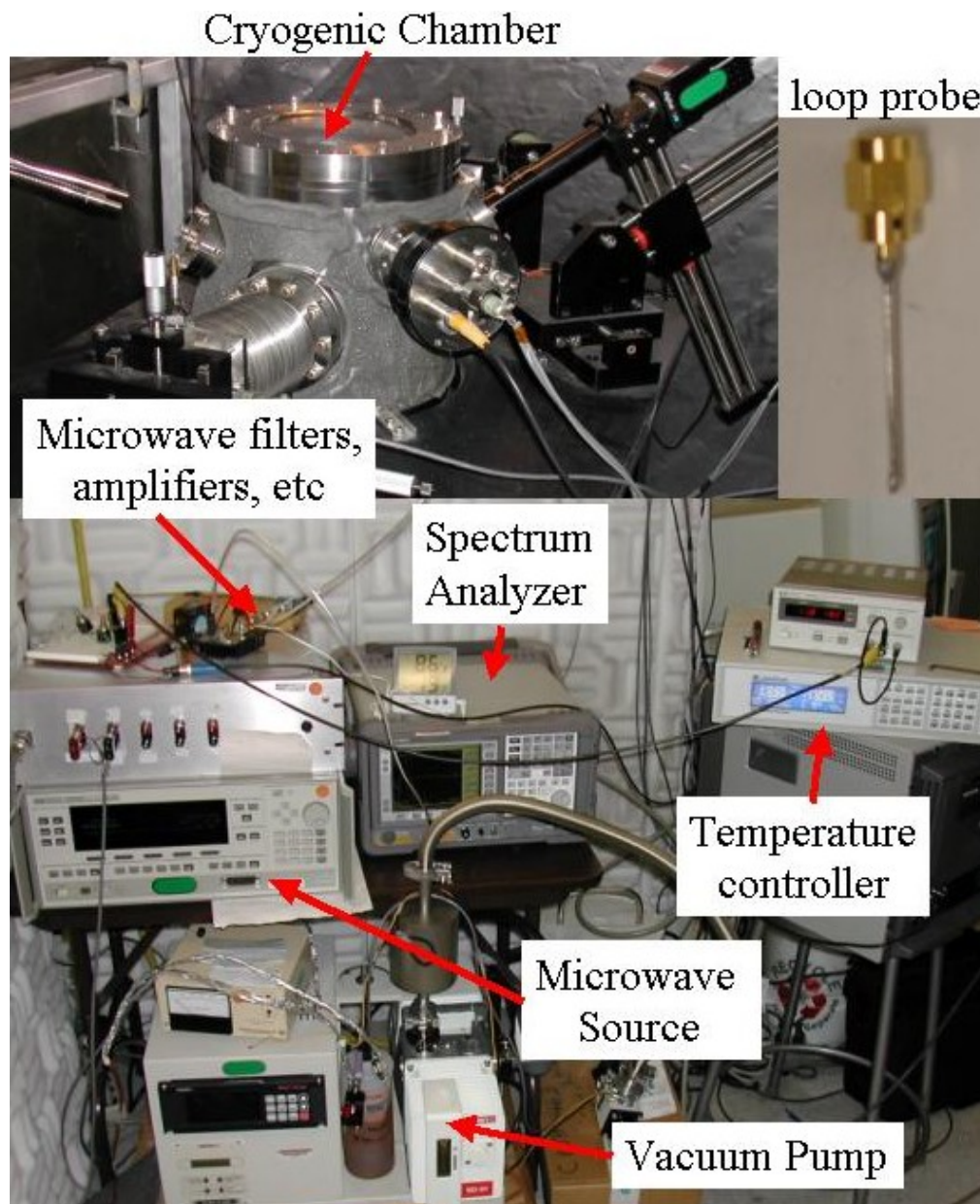


Fig. 1.11 Pictures of the microscope. The bottom shows the microwave electronics, mechanical vacuum pump, and the temperature controller. The upper left is the cryogenic chamber and the turbo pump (not shown) is located right beneath the chamber. The upper right is a picture of the non-magnetic loop probe that I used in both permeability imaging and nonlinear measurements.

The probe of this microscope is similar to the one discussed in the previous section (Fig. 1.11). It is made of a non-magnetic semi-rigid coaxial cable, with its inner conductor forming a semi-circular loop, shorted with the outer conductor. With this arrangement, the probe couples to the sample via the magnetic fields generated in the vicinity of the probe, and induces currents flowing on the sample surface. This feature is especially important for studying the nonlinear electrodynamics in superconductors. We can perturb the superconducting state with these locally induced currents, and study the local nonlinear response due to any existing nonlinear mechanisms. In addition, the direction of the induced currents is determined by the orientation of the loop probe, since the sample is approximately modeled as an image loop of the loop probe. Thus, we expect that anisotropy in the screening response of cuprate superconductors can also be investigated with this microscope.

In our experiment, the sample is kept in a high-vacuum cryogenic chamber (Fig. 1.11). The pressure can be as low as  $10^{-7} \sim 10^{-8} \text{ Torr}$ , and the temperature ranges from  $3.5\text{K}$  to room temperature. This continuous flow cryostat was designed and built in collaboration with the late Eric Swartz of Desert Cryogenics. Both the frequency and power of the input signal and the sample temperature are controlled by LabView<sup>®</sup> programs via GPIB interfaces.

### 1.3.3 Principle of Operation



The samples that we want to study are superconducting thin films (for reasons explained in Chapter 3). To avoid the edge effect, mentioned previously, and to directly examine the material properties, we would like to locally apply currents on the surface of the films and study their electromagnetic response. I note that this is in contrast to almost all other work on intrinsic nonlinearities in superconductors, which generally employ global magnetic fields or currents to induce nonlinear response. We apply the currents only locally to the film through the coaxial loop probe, which is placed very close to the sample surface ( $12.5 \mu\text{m}$ , spaced by a Teflon<sup>TM</sup> sheet). When we apply a single-toned sinusoidal microwave signal to the film through the probe, a localized microwave current distribution is induced on the sample surface beneath the probe. In this way, we are only studying the local sample properties, and avoiding the edge current buildup effect, which is encountered in all global measurement techniques.

If there is any nonlinear mechanism locally present in the sample, the electromagnetic response from the sample surface will be modulated, and this couples back to the loop probe. The modulation of the electromagnetic response can be divided into two categories: one that preserves the time-reversal symmetry, and another one that breaks it. The former reflects the presence of nonlinearities which preserve the time-reversal symmetry, and appears as higher odd harmonics. What if some nonlinearities break the Time-Reversal symmetry? The key signature of such nonlinearities is the presence of spontaneous local currents flowing on or in the sample. While such currents are present, the surface

electromagnetic responses will not be time-reversal invariant any more, and result in  $2f$ ,  $4f$  etc, signals. In our measurements, we measure both  $2f$  and  $3f$  signals to address the presence of both types of nonlinearities.

## CHAPTER 2

### INTRODUCTION TO NONLINEAR SUPERCONDUCTIVITY

Nonlinearities in superconductivity have been of great concern because of both industrial applications and the need to elucidate the fundamental physics of high- $T_c$  superconductors. There have been great efforts devoted from the industrial side in making passive microwave devices, for instance, microwave filters and resonators, with high- $T_c$  superconductors. For modest power levels ( $< 1$  W circulating power), the performance of such devices is much better than that of conventional devices made from ordinary metals. In particular, superconducting filters have extremely sharp filtering bands, excellent frequency selectivity, and much lower loss and greater  $Q$ .

However, as the power is increased, nonlinear behavior becomes a serious issue. For example, cellular phone service providers would like to have individual channels as close as possible in frequency, so that within a limited bandwidth, one can service more customers. To accomplish this goal, microwave band-pass filters with excellent frequency selectivity are required. However, if there are two signals very close to each other (at frequencies  $f_1$  and  $f_2$ ), and the microwave filter is nonlinear, an effect called intermodulation distortion occurs. The superconducting films making up the filter generate

third and fourth signals at frequencies  $2f_1-f_2$  and  $2f_2-f_1$ , and these signals may be interpreted as “ghost” users in the same band. This is the main reason why the nonlinear behavior of superconductors can restrict the microwave applications of superconductors.

After more than one decade of effort, it is now widely agreed that the nonlinearities causing trouble for industrial applications are mainly extrinsic in nature. They are dominated by structural defects, for instance, the grain boundaries that can form a weak-link network and introduce Josephson junction-like nonlinearity. Another extrinsic source of nonlinearity originates in the geometry of the device, which may build up large currents at edges and around corners and allow vortices to enter and exit the films. However, while all these extrinsic nonlinearities are being explored and discussed, one question remains: what are the intrinsic nonlinearities in superconductors? In other words, what sets the ultimate limit of the nonlinear response of a superconductor to external electromagnetic disturbances?

In this chapter, I discuss the nonlinear Meissner effect, which is an intrinsic nonlinearity expected to be present in all superconductors. Different treatments of this fundamental nonlinearity are discussed, including the Ginzburg-Landau theory, BCS theory, and a representative phenomenological model suggested by an Italian research group.

## 2.1 Nonlinear Meissner Effect

As mentioned above, the nonlinear Meissner effect (NLME) is a phenomenon expected to be present in all superconductors. The qualitative picture of this effect is that the screening currents flowing in a superconductor, due to either the presence of external magnetic fields or applied currents in the Meissner state, act as pair-breakers, destroying Cooper pairs. This screening current, therefore, reduces the super-fluid density and high frequency conductivity ( $\sigma_2$ ) of the superconductor. As a result, the super-fluid density becomes a function of the external current or magnetic field. This leads to a number of measurable consequences, including field- and current-dependence in the surface impedance, penetration depth, and harmonic generation.

### 2.1.1 The Ginzburg-Landau Theory

The NLME can be described by the Ginzburg-Landau (GL) theory. GL theory is a phenomenological theory intended to describe superconductivity near  $T_c$ , although it often works reasonably well at lower temperatures. Superconductivity is described by a complex order parameter  $\psi$  that is zero above  $T_c$  and non-zero below  $T_c$  in the equilibrium state. The basic postulate of GL theory is that if  $|\psi|$  is small and varies slowly in space, the free energy density of the superconductor  $f$  can be expanded in a series of the form

$$f = f_{n0} + \alpha|\psi|^2 + \frac{\beta}{2}|\psi|^4 + \frac{1}{2m^*} \left| \left( \frac{\hbar}{i} \nabla - q^* \vec{A} \right) \psi \right|^2 + \frac{\mu_0 H^2}{2} + \dots, \quad (2.1)$$

where  $f_{n0}$  is the free energy density in the normal state in the absence of magnetic fields,  $m^*$

and  $q^*$  are effective mass and charge of Cooper pairs,  $\vec{A}$  is the vector potential,  $H$  is the magnetic field, and  $\psi$  is the GL order parameter ( $|\psi|^2 = n_s$ , the super-fluid density) [26,27].  $\alpha$  and  $\beta$  are coefficients in the expansion, and  $\alpha$  is positive in the normal state and negative in the superconducting state, while  $\beta$  is always positive.

The GL theory is capable of dealing with inhomogeneous superconductors. In the presence of fields, currents, or gradients of the GL order parameter,  $\psi(\vec{r}) = |\psi(\vec{r})|e^{i\phi(\vec{r})}$  will adjust itself to minimize the total free energy, which can be calculated by the volume integral of Eq. 2.1. By a standard variational method, this leads to the GL differential equations

$$\alpha\psi + \beta|\psi|^2\psi + \frac{1}{2m^*} \left( \frac{\hbar}{i} \vec{\nabla} - q^* \vec{A} \right)^2 \psi = 0 \quad (2.2)$$

$$\text{and } \vec{J} = \vec{\nabla} \times \vec{h} = \frac{q^* \hbar}{2m^* i} (\psi^* \nabla \psi - \psi \nabla \psi^*) - \frac{q^{*2}}{m^*} \psi^* \psi \vec{A} \quad (2.3)$$

$$\text{or } \vec{J} = \frac{q^*}{m^*} |\psi|^2 (\hbar \nabla \phi - q^* \vec{A}) = q^* |\psi|^2 \vec{v}_s. \quad (2.4)$$

From the second term ( $|\psi|^2 \psi$ ) and the presence of the vector potential in Eq. 2.2, we can conclude that the GL equations are intrinsically nonlinear.

Gittleman *et al.* [28] solve the GL equations for an infinitely wide slab (Fig. 2.1) of s-wave, type II superconducting thin film with thickness  $d < \lambda$ , and a parallel magnetic field

applied on one side. They found that

$$|\psi|^2 \cong \left( \frac{\lambda_0}{\lambda(\tau)} \right)^2 \left[ 1 - \frac{\lambda_0^2}{2H_0^2} f(\tau) J^2 \right], \quad (2.5)$$

in the limit  $\frac{\lambda_0^2}{2H_0^2} f(\tau) J^2 \ll 1$ , where  $\psi$  is the Ginzburg-Landau order parameter,  $\tau = T/T_c$ ,

$|\psi|^2$  represents the super-fluid density,  $\lambda(\tau)^2 = \lambda_0^2 (1 - \tau^4)^{-1}$  is the temperature-dependent penetration depth, and  $f(\tau) = (1 - \tau^2)^{-2} (1 - \tau^4)^{-1}$ , provided the thermodynamic critical field is  $H_c(\tau) = H_0 (1 - \tau^2)$ .

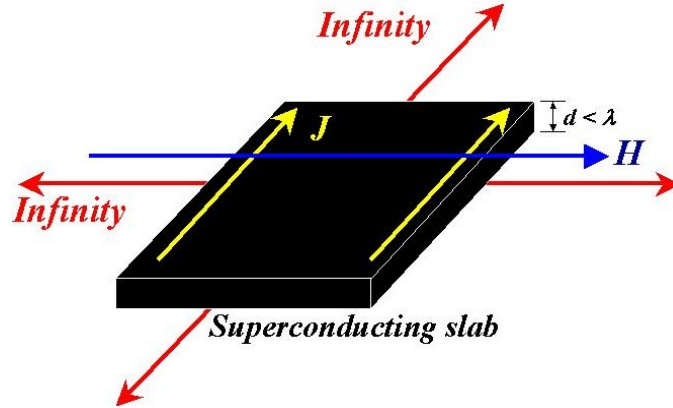


Fig. 2.1 Schematics of the GL calculation performed by Gittleman *et. al.*

Rewriting this equation in terms of a temperature and current density dependent super-fluid density, we have

$$\frac{n_s(\tau, J)}{n_s(\tau, 0)} = \frac{\lambda^2(\tau, 0)}{\lambda^2(\tau, J)} \cong 1 - \frac{1}{2} \frac{J^2}{J_0^2 (1 - \tau^2)^2 (1 - \tau^4)} \cong 1 - \frac{1}{2} \frac{J^2}{J_c^2(\tau)}, \quad (2.6)$$

with  $\frac{1}{2} \frac{J^2}{J_c^2(\tau)} \ll 1$ , where  $J_0 = H_0/\lambda_0$  is the zero-temperature de-pairing critical current

density, and  $J_c(\tau)$  is the temperature dependent de-pairing critical current density. I note that  $J_c(\tau)$  sets the current scale required to observe the NLME.

Equation 2.6 shows a quadratic current-dependent term, which describes the suppression of the super-fluid density in the NLME. Since Ginzburg-Landau theory is a phenomenological theory that works for temperatures near  $T_c$ , this equation is most applicable for  $\tau \lesssim 1$ . Hence the asymptotic temperature dependence,  $(1-\tau^2)^2(1-\tau^4) \sim (1-\tau)^3$  as  $\tau \rightarrow 1$ , is most important near  $T_c$ . The fitting of the GL theory to my experimental data can be found in Chapter 5.

### 2.1.2 The Bardeen-Cooper-Schrieffer (BCS) Theory

A more detailed description of the NLME can be drawn from the Bardeen-Cooper Schrieffer (BCS) microscopic theory of superconductivity. Consider an s-wave superconductor in the Meissner state for simplicity. When a current is flowing in a superconductor, represented by a super-fluid velocity  $v_s$ , the energy of a Cooper pair at the forward end of the Fermi surface (along the current direction) is higher than at the back end by

$$\Delta E = \frac{1}{2}m(v_f + v_s)^2 - \frac{1}{2}m(v_f - v_s)^2 = 2mv_f v_s = 2p_f v_s, \quad (2.7)$$

where  $v_f$  and  $p_f$  are the Fermi velocity and momentum,  $m$  is the effective mass of the



Cooper pairs, and  $v_s$  is the super-fluid velocity. Since quasiparticles are created by thermal excitation over the energy gap at finite temperatures in superconductors, and their excitation is easier upon going from below the gap on the front end to above the gap on the back end, this energy difference leads to an additional quasiparticle current flowing from the forward to the back end of the Fermi surface [28]. Therefore, the net screening current consists of a forward super-fluid current and a quasiparticle backflow current

$$\mathbf{J}_{total} = \mathbf{J}_s - \mathbf{J}_{qp}, \quad (2.8)$$

where  $J_s$  is the super-fluid current density, and  $J_{qp}$  is the quasiparticle backflow. Xu, Yip and Sauls [29,30] calculated the contribution from  $J_{qp}$  for both s-wave and d-wave superconductors, whose energy gaps on the Fermi surface are shown in Fig. 2.2. In the low temperature limit, Yip and Sauls gave a general expression for calculating the total currents flowing in both s- and d-wave superconductors [29]:

$$\begin{aligned} \bar{\mathbf{J}} &= \bar{\mathbf{J}}_s + \bar{\mathbf{J}}_{qp} \quad (2.9) \\ &= -eN(0) \int d^2\Theta n(\Theta) \bar{\mathbf{v}}_f(\Theta) \times \\ &\quad \left\{ \bar{\mathbf{v}}_f(\Theta) \cdot \bar{\mathbf{v}}_s + \int_0^\infty d\varepsilon \left[ f(\sqrt{\varepsilon^2 + |\Delta(\Theta)|^2} + \bar{\mathbf{v}}_f(\Theta) \cdot \bar{\mathbf{v}}_s) - f(\sqrt{\varepsilon^2 + |\Delta(\Theta)|^2} - \bar{\mathbf{v}}_f(\Theta) \cdot \bar{\mathbf{v}}_s) \right] \right\}, \end{aligned}$$

where  $N(0)$  is the density of states of quasiparticles at the Fermi surface,  $n(\Theta)$  is the angle-resolved density of states normalized to unity,  $\bar{\mathbf{v}}_f(\Theta)$  is the angular dependent Fermi velocity on the Fermi surface, and  $\Delta(\Theta)$  is the angular dependent gap function. The angle  $\Theta$  is defined in Fig. 2.2. By expanding Eq. 2.9 to leading order in  $\bar{\mathbf{v}}_s$ , we can re-write Eq. 2.9

as  $\vec{J} = n_s(J) e^* \vec{v}_s$  and derive the current-dependent super-fluid density  $n_s(J)$ . For s-wave superconductors, the field (or current) dependence of the penetration depth

$\lambda(J) \propto 1/\sqrt{n_s(J)}$  derived from Eq. 2.9 is

$$\lambda(T, H) - \lambda(T, 0) \cong a(T) \left( \frac{H}{H_0(T)} \right)^2, \quad (2.10)$$

for  $H \ll H_0(T)$ , where  $a(T)$  is a coefficient. This leads to the same form as that obtained from the GL theory, Eq. 2.6.

The situation is different for a d-wave superconductor. Due to the presence of the nodes in the Fermi surface of d-wave superconductors, the energy required for quasiparticle excitations is extremely small near the nodes. Since the quasiparticles can be thermally excited, and the nodes allow quasiparticles to be excited at very low energies, the difference becomes very important in the low temperature limit. Yip and Sauls showed that the calculation of the field-dependence of the penetration depth for d-wave superconductors at  $T = 0$  does not depend on the field quadratically, but linearly on the magnitude of the field:

$$\lambda(H) - \lambda_0 \cong b \left| \frac{H}{H_0} \right|, \quad (2.11)$$

where  $b$  is a coefficient.

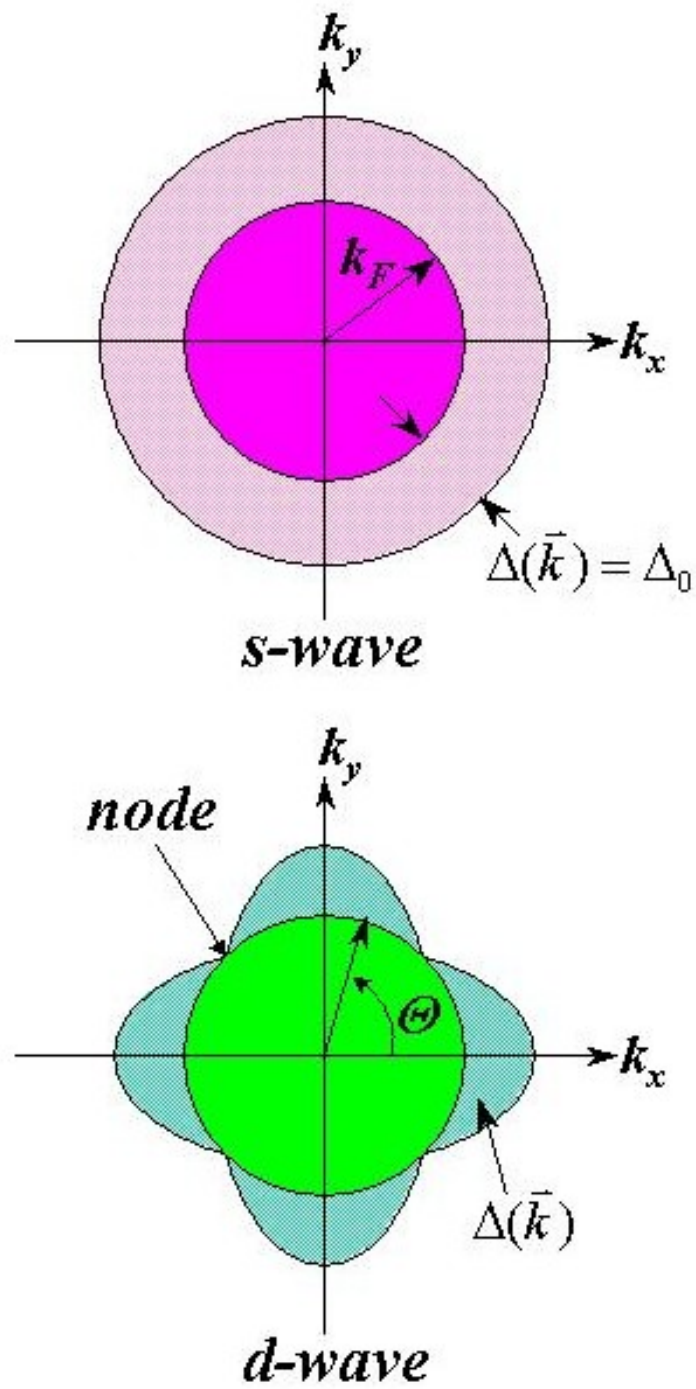


Fig. 2.2 Fermi surfaces of s-wave (nodeless) and d-wave (node) superconductors (not to scale).

In these equations,  $H_0(T)$  is of the order of the thermodynamic critical field,  $a(T)$  is a coefficient which is proportional to  $e^{-\Delta/k_B T}$  ( $\Delta$  is the superconducting gap) in the low temperature limit and monotonically increases as a function temperature, and  $b$  is a coefficient of the order of unity for fields parallel to the node direction. However, since the superconducting gap function of d-wave superconductors is anisotropic,  $b$  is also anisotropic and reduced by a factor of  $1/\sqrt{2}$  for fields parallel to the anti-node direction. This conclusion not only indicates the fundamental difference between the s-wave and d-wave superconductors in terms of their electromagnetic response to the externally applied field/current, but also the coefficient  $b$  in d-wave superconductors turns out to be anisotropic in the ab-plane. However, it is now believed that Yip and Sauls' prediction can only be observed in very clean crystals, at very low temperatures (reduced temperature  $\ll 10^{-2}$ ), which makes conclusive temperature-dependent measurements of the NLME very difficult to carry out experimentally.

I give a summary of the electrodynamic responses of the penetration depth  $\lambda$  expected from the NLME calculated by Yip and Sauls in Table 2.1. The harmonic generation predictions will be discussed in Chapters 5 and 6.

Table 2.1 Summary of Yip and Sauls' [4, 5] predictions for the NLME in d-wave and s-wave superconductors

	$T < 0.01T_c$	$T = 0;$ $\vec{B} \parallel \text{node}$	$T = 0;$ $\vec{B} \perp \text{node}$	Expected Harmonics at $T < 0.01T_c$
d-wave superconductor	–	$\lambda(H) - \lambda_0$ $\propto b H/H_0 $	$\lambda(H) - \lambda_0$ $\propto \left(\frac{b}{\sqrt{2}}\right) H/H_0 $	$P_{3f} \propto P_f^2$
s-wave superconductor	$\lambda(T, H) - \lambda(T, 0)$ $\propto a(T) \left(\frac{H}{H_0(T)}\right)^2$	–	–	$P_{3f} \propto P_f^3$

Recently, similar theoretical work done by Dahm and Scalapino predicts that for both s-wave and d-wave superconductors, the imaginary part of the conductivity,  $\sigma_2$ , or equivalently the super-fluid density  $n_s = m\omega\sigma_2(\omega)/e^2$ , should retain a quadratic dependence on the screening current density as [31,32]

$$\frac{n_s(j, T)}{n_s(0, T)} = \frac{\sigma_2(j, T)}{\sigma_2(0, T)} \cong 1 - b_\Theta(T) \left(\frac{j}{j_c}\right)^2, \quad j \ll j_c, \quad (2.12)$$

at temperatures higher than Yip and Sauls' regime ( $t > 10^{-2}$ ). Here  $b_\Theta(T)$  is an angle- and temperature-dependent function, which is different for s- and d-wave superconductors, and  $\Theta$  is the angle indicated in Fig. 2.2. For s-wave superconductors  $b_\Theta(T)$  is angle-independent, and monotonically decreases with decreasing temperature, which means that

the NLME is weaker at low temperatures. On the other hand,  $b_{\phi}(T)$  is expected to rise dramatically at low temperatures in d-wave superconductors as shown in Fig. 2.3.

This difference in  $b_{\phi}(T)$  in the low temperature regime (but not as low as the Yip and Sauls' regime) serves as a clear distinguishing signature of s-wave or d-wave superconductors. Additionally, the Dahm and Scalapino theory works in a much wider temperature range, so that conclusive experimental measurements are possible. Since d-wave superconductors have an anisotropic gap in the ab-planes,  $b_{\phi}(T)$  is an angle-dependent function, and is larger for currents flowing along the node-line at lower temperatures. It is also worth noting that in the low temperature limit, Dahm and Scalapino's work is consistent with Yip and Sauls' result [32].

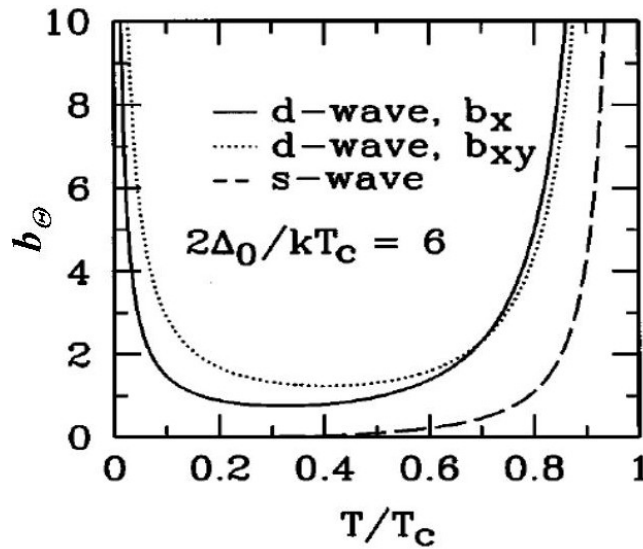


Fig. 2.3 Calculation of  $b_{\phi}(T)$  for s-wave and d-wave (with currents flowing in different directions) superconductors from Dahm and Scalapino [31].

Listed in Table 2.2 are some of the signatures of the NLME expected to be observed experimentally. The 1<sup>st</sup> and 4<sup>th</sup> signatures are discussed in detail in Chapters 5 and 6. The 2<sup>nd</sup> and 5<sup>th</sup> signature are expected to be observed in the low temperature limit. Since the sensitivity of my system is not good enough at such low temperatures, I could not test the theory in this regime. I provide a more detailed discussion of how to improve the sensitivity in Chapter 7. The observation of the 3<sup>rd</sup> signature requires an angular resolved measurement which is not presently available in my system. In principle, further modifications can be done to perform such measurements.

Table 2.1 Summary of expected experimental signatures of the NLME.

Signature of the NLME	Measured Effect
1. Temperature-Dependent Scaling Current Density $J_{NL}$	Absolute $P_{IMD}(T)$ and $P_{3f}(T)$ measurements directly relate to $J_{NL}(T)$
2. Temperature Dependence of $P_{3f}$ at Low Temperatures	Expect upturn of NLME coefficient at low temperatures
3. Angular Dependence	$\sqrt{2}$ angular variation of NL response [29]
4. RF Magnetic Field Dependence	Distinguish trapped flux from intrinsic effects. Examine the power-dependences of the second- and third-order nonlinearities.
5. Dirt Dependence	Impurities should increase field scale $H_1$ for $\Delta\lambda \sim H/H_1$ [33]

### 2.1.3 Prior Experiments on the Nonlinear Meissner Effect

The earliest work on the nonlinear response of superconductors in the Meissner state dates back to Pippard [1] (1947), Spiwak [34] (1958), Sharvin and Gantmaker [35] (1961), and Gittleman [28] (1965). Their work focused on s-wave, type-I superconductors in high fields and temperatures close to  $T_c$ . In general, these results were consistent with the simple picture for the nonlinear Meissner effect (NLME) discussed above. A comprehensive study of the nonlinear Meissner effect at low fields and lower temperatures in s-wave superconductors was done by Sridhar with the surface impedance technique [36]. His results showed that the basic NLME predictions were correct, although corrections from non-equilibrium effects can be important for type-I superconductors. Recently, measurements of the change in penetration depth of the conventional type-II superconductor  $V_3Si$  showed a quadratic nonlinearity, as expected for an s-wave superconductor [37]. The temperature dependence of the prefactor agreed with theory over the limited range of the experiment,  $0.5 < T/T_c < 0.85$ .

Early work on the non-linear Meissner effect in d-wave superconductors was carried out with an rf resonator technique to measure the change in penetration depth with applied dc field [38]. Ref. [39] is the first measurement using this technique and the authors claimed good qualitative agreement between the data on  $YBa_2Cu_3O_7$  crystals and the Ginzburg-Landau theory. Maeda, *et al.*, [40] had measurements on  $Bi_2Sr_2CaCu_2O_8$ , and claimed that  $\Delta\lambda(T,H) \sim H^2$  at high temperatures and  $\Delta\lambda(T,H) \sim H$  at lower temperatures, qualitatively in agreement with the Yip and Sauls prediction for the NLME in d-wave superconductors.



However, the magnitude of the observed nonlinearity was much greater than predicted, the linear-in-H behavior persisted to too high a temperature, and considerable hysteresis was seen in the  $\lambda(H)$  curves, suggesting that vortex entry and motion into the crystals dominated the response.[40]

Carrington, *et al.* [41] carried out sensitive measurements of the change in penetration depth of a YBCO crystal as a function of applied dc field. Their results show a linear increase in penetration depth at low temperatures, but the magnitude of the effect is smaller than that predicted by Yip and Sauls. Moreover, they did not see the quadratic dependence of  $\Delta\lambda(H)$  expected at higher temperatures. Similar measurements of the magnetic penetration depth nonlinearity in untwinned single crystals of  $\text{YBa}_2\text{Cu}_3\text{O}_7$  at UBC [42] show a NLME consistent with the Yip and Sauls prediction for the field dependence at 1.2 K, but did not show the expected temperature dependence or low-field behavior.[43] These measurements also revealed enhanced nonlinearities at higher temperatures, possibly due to extrinsic effects. However, all of these experiments suffer from the use of a globally applied magnetic field (as discussed in Section 1.2) to measure the NLME; the edges and corners of the sample invite vortices to enter the sample. It is well established that vortex entry and motion creates a very strong nonlinear response [44,45]. The UBC group saw that the magnitude of their nonlinear penetration depth signal dropped dramatically when they polished away the corners of their single crystal sample [42].

The apparent absence of a linear-in-H NLME may be explained by the calculations done by Li *et al.* [46], following Kosztin and Leggett [47]. They suggest that the linear-in-H NLME may be suppressed by the non-local effects. They also pointed out that the NLME might still be visible for currents flowing parallel to the nodal direction. Hence the NLME as predicted by Yip and Sauls has not been demonstrated experimentally.

## 2.2 Vigni's model of modulating normal fluid density by external AC fields

In addition to the NLME in the low temperature limit, in Fig. 2.4, I show a  $P_{3f}(T)$  data of NbN near  $T_c \sim 10.5\text{K}$ , which demonstrates the enhanced NLME near  $T_c$ . Many empirical models exist to explain observation of the NLME near  $T_c$  [33,48]. Here we focus on one model typical of this genre.

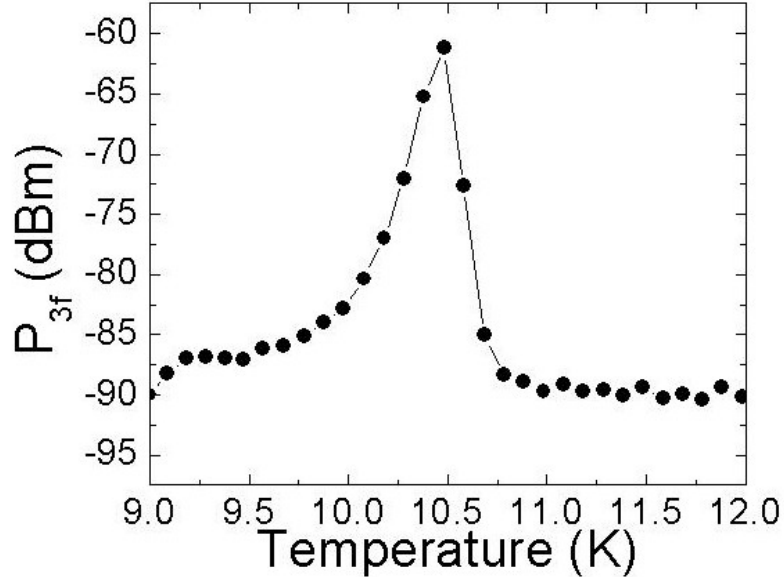


Fig. 2.4  $P_{3f}(T)$  measured on an unpatterned NbN thin film near the  $T_c \sim 10.5\text{K}$ .

A purely empirical model based on the two-fluid model is used by Vigni *et al.* [48] to describe the electromagnetic response of the super-fluid density to external magnetic fields. Considering the same basic idea as the NLME, which is that the quasiparticle excitations are enhanced due to the presence of external fields and currents, Vigni *et al.* assume that the enhancement of the excitation quasiparticle density is dependent on the absolute value of the instantaneous external magnetic field as,

$$w_n(T, t) = w_n(T) + |\gamma H \cos(\omega t)|, \quad (2.13)$$

where  $w_n$  is the normalized quasiparticle density,  $T$  is the temperature,  $t$  represents time, and  $\gamma$  is a constant, that serves as a fitting parameter in this model. I note that the  $|H|$  dependence of  $w_n$  was chosen to fit their particular data, which shows  $P_{3f} \sim P_f^2$ . This is different from our data, and that of many other researchers, which show  $P_{3f} \sim P_f^3$  near  $T_c$ . In addition, this model assumes that the super-fluid and quasiparticle densities come to equilibrium with the external current/field density instantaneously. This approximation may break down as the order parameter relaxation time grows near  $T_c$ . The suppression of the super-fluid density is given by,

$$w_s(T, t) = w_s(T) - |\gamma H \cos(\omega t)|, \quad (2.14)$$

where  $w_s = 1 - w_n$  is the normalized super-fluid density.

By solving Maxwell's equations for a polarized electromagnetic plane wave propagating normal to the surface of an infinite isotropic superconducting slab of thickness  $D$ , Vigni *et al.* calculated the induced magnetic field in the superconductor. Since the super-fluid

density is suppressed by the field as above, the induced magnetic field is no longer purely sinusoidal, and contains higher order harmonic content

$$\langle B \rangle = \frac{2\mu_0 H \cos(\omega t + \varphi(t)/2)}{D[a^2(t) + b^2(t)]^{1/4}}, \quad (2.15)$$

where  $\langle B \rangle$  is the averaged magnetic field in the sample,  $H$  is the magnitude of the applied field,

$$a(t) = \frac{w_s(T, t)}{\lambda^2},$$

$$b(t) = -\frac{2w_n(T, t)}{\delta^2},$$

$$\tan \varphi(t) = \frac{b(t)}{a(t)},$$

$\lambda$  is the London penetration depth, and  $\delta$  is the normal metal skin depth.

By calculating the Fourier components of  $\langle B \rangle$  at the third harmonic frequency,

$$a_3 = \frac{1}{\pi} \int_0^{2\pi} \langle B \rangle \cos(3\omega t) d(\omega t), \quad (2.16)$$

$$b_3 = \frac{1}{\pi} \int_0^{2\pi} \langle B \rangle \sin(3\omega t) d(\omega t), \quad (2.17)$$

one finds the power of the third harmonic signal becomes

$$P_{3f} \propto a_3^2 + b_3^2. \quad (2.18)$$

It is worth noting that  $a_3$  and  $b_3$  peak at different temperatures according to this calculation.

Therefore, phase-sensitive harmonic measurements can be performed to further test this

model.

It is worth noting that Vigni's model is claimed to work near  $T_c$  with isotropic superconductors, or for special configurations (for instance,  $H(\omega)$  parallel to the c-axis of YBCO crystals) in strongly anisotropic superconductors. However, this model is significantly different from the GL or BCS theory. The most important difference is the power dependence of the third harmonic signal on the magnetic field. While both GL and BCS theory predict a power-3 dependence near  $T_c$ , this model yields a power-2 dependence due to the linear modulation of the super-fluid density by  $|H(\omega)|$ , which was motivated to better fit Vigni's experimental data. Of course, this model is phenomenological and not based on any microscopic theory of superconductivity.

### 2.3 Andreev Bound State Nonlinearities

In addition to the NLME for bulk superconductors, surface states called Andreev bound states (ABS) are formed on certain surfaces of d-wave superconductors in the low temperature regime. The ABS are also nonlinear in nature. Here we would like to calculate their contribution to our harmonic response measurements.

Andreev bound states are a result of Andreev reflection at the normal/superconducting (N/S) interface of a d-wave superconductor. They only occur where there is a  $\pi$  phase shift between different lobes of the  $d_{x^2-y^2}$  order parameter for a quasiparticle undergoing specular reflection at the interface. Consider an N/S interface as in Fig. 2.5 with carriers incident

from the normal layer to the superconducting layer at point A. When carriers are Andreev reflected from point A, they experience a  $+\Delta$  order parameter. Then the carriers are normally reflected by the N/I interface and Andreev reflected again at point B, where they experience a  $-\Delta$  order parameter. As a result, the quasiparticles in the normal region experience a potential well with depth  $+\Delta(-\Delta)$ , and are bound to this normal region. Theoretical works [49] indicate that in the limit where the thickness of the normal region approaches zero, this bound state still exists. The energy of the bound state is the Fermi energy. Hence a d-wave superconductor with a [110] exposed surface is expected to host an Andreev bound state.

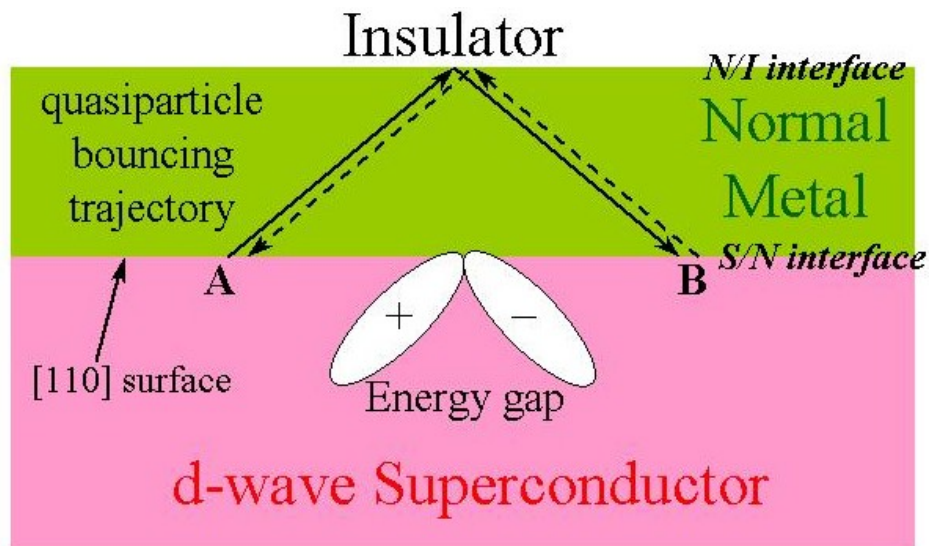


Fig. 2.5 Quasiparticles in the normal metal are specularly reflected at the N/I interface, and Andreev reflected at the S/N interface. Because the superconducting order parameter changes its sign between subsequent Andreev reflections, the quasiparticles form a bound state in the normal metal. [49]

One signature of the presence of the ABS is a non-zero quasiparticle density of states (DOS) at zero energy, which can be detected as a zero-bias conductance peak (ZBCP) in the tunneling spectrum through the surface containing the ABS. One implication of this signature is that even at very low temperature ( $kT \ll \Delta$ ), the non-zero DOS of quasiparticles can allow a quasiparticle current to flow into this surface state, and this will lead to nonlinear behavior of the super-fluid density and London penetration depth.

In the absence of impurities, the modification to the low energy quasiparticle DOS of d-wave superconductors ( $\propto |E|$ , measured from the Fermi energy) due to the ABS is represented as an additional  $\delta$ -function,  $\delta(E)$ , in the DOS. Since disorder is inevitable, this  $\delta$ -function in the quasiparticle DOS is expected to be broadened, and becomes finite at zero-energy. The surface DOS of normal electrons (the quasiparticles in superconductors) can be directly measured via tunneling into the surface and measuring the differential conductance,  $dI/dV$ , which is proportional to the surface DOS. If the ABS does exist on certain surfaces, then the tunneling spectrum ( $dI/dV$  vs. biasing voltage) of these surfaces should demonstrate a singular peak near zero-bias voltage (the ZBCP), meaning tunneling quasiparticle currents are allowed to flow at zero energy, rather than  $dI/dV=0$  for an ordinary tunneling spectrum for d-wave superconductors.

Various tunneling experiments have been performed to confirm the presence of this surface state. L. Greene *et al.* [50,51,52] and Deutscher *et al.* [53,54,55,56] performed

planar junction tunneling experiments on [110] and other orientation surfaces of YBCO, and repeatedly found the zero-bias conductance peak (ZBCP). They did not find a ZBCP for tunneling into [001] oriented surfaces. Wei *et al.* [57] also performed Scanning Tunneling Microscopy (STM) experiments onto [001] YBCO surfaces with terrace-like features, and claimed to see ZBCP on the terraces, where the [110] surfaces may be exposed, but not on the plain areas.

However, in addition to seeing the ZBCP, a spontaneous splitting of the ZBCP at zero magnetic field is also observed on some occasions. This splitting is commonly understood as resulting from the presence of a so-far-uncertain time-reversal-symmetry breaking (TRSB) mechanism.

According to Deutscher *et al.*, who examined YBCO films with different doping levels, from slightly under-doped to slightly over-doped, only in over-doped YBCO films is the splitting observed. They claim that there is a critical doping level for the TRSB mechanism to emerge.

On the other hand, L. Greene *et al.* focused on optimally doped YBCO films, and observed spontaneous splitting only under certain conditions. They attribute the difference to the details of the tunnel-junctions. Though both Greene *et al.* and Deutscher *et al.* observed the spontaneous ZBCP splitting at temperatures just below 10K, there are significant differences between their results. In Deutscher's work, even when the ZBCP



doesn't show a spontaneous splitting, the splitting can be induced by external magnetic fields. On the other hand, in Greene's work, the ZBCP splits in an applied magnetic field only if the spontaneous splitting is observed. If the spontaneous splitting is not observed, the ZBCP is only broadened, not split, by applying external fields.

Theoretical work has not yet resolved the controversy. Greene *et al.* claimed that their results are consistent with the model of a sub-dominant order parameter with a  $\pi/2$  phase difference from the dominant d-wave order parameter in the ABS. The idea is that, since the de-pairing mechanism for the d-wave order parameter is so strong in this surface state, the existence of this sub-dominant interaction gives the quasiparticle in the ABS an alternative pairing-interaction for forming Cooper pairs. It is the  $\pi/2$  phase difference between the dominant and sub-dominant order parameters ( $d+is$ ) that leads to a spontaneous flowing surface current [58]. However, this model doesn't imply any doping dependence of TRSB in the ABS, and neither do other models to my knowledge.

It is also believed that a TRSB surface state will break into domains.[59] This will insure that no bulk spontaneous surface current will be created, but that small circulating currents will exist on the length scale of the domain size. Because of this, one does not expect to detect the TRSB signal from a macroscopic measurement (such as magnetization). However, the near-field microwave microscope creates RF currents on a variety of length scales (all shorter than the free-space wavelength), determined by the geometry of the near-field probe. Hence our microscope can be sensitive to the local TRSB domains as long as

the probe creates significant current components on spatial frequency scales comparable to, or smaller than, the TRSB domain size.

Another sign of the ABS is an upturn of the London penetration depth at temperatures lower than  $\sqrt{\xi_0/\lambda_0} T_c$ , where  $\xi_0$  and  $\lambda_0$  are the zero temperature coherence length and London penetration depth.[60] For HTSC,  $\xi_0/\lambda_0$  is on the order of  $10^{-2}$ ; hence the upturn of the penetration depth should be observed for  $T \leq 0.1T_c$ . To understand this upturn of the penetration depth, we start with the formulation of the temperature dependent penetration depth for d-wave superconductors.

At low temperature, the increase of  $\lambda$  due to the thermal excitations of quasiparticles is[61]

$$\frac{\Delta\lambda(T)}{\lambda_0} = -\int_{-\infty}^{\infty} \frac{N(E)}{N(0)} \frac{\partial f}{\partial E} dE, \quad (2.19)$$

where  $f$  is the Fermi function  $f(E) = 1/(e^{E/k_B T} + 1)$ ,  $\lambda_0$  is the zero temperature penetration depth, and  $N(E)$  is the d-wave DOS  $\propto |E|$  ( $E$  is measured relative to the Fermi energy),

which leads to  $\frac{\Delta\lambda(T)}{\lambda_0} = a \frac{T}{T_c}$ . This is the famous linear-in-T penetration depth temperature dependence, first observed in YBCO crystals by the UBC group [62] and later by our group [63]. Here,  $a$  is a coefficient of the order of unity. Its value depends on the shape of the Fermi surface and the angular slope of the gap function near the nodes. For a 2D  $d_{x^2-y^2}$

tetragonal superconductor with a cylindrical Fermi surface and order parameter

$\Delta(\phi) = \Delta_0 \cos(2\phi - 2\theta + \pi/2)$ , where  $\theta$  is the angle that the normal vector of the exposed surface of the superconductor makes with the [110] direction,  $a$  is around 0.32[60].

The above picture gets modified because the ABS adds a  $\delta(E)$ , to the DOS in Eq. 2.19. Ultimately this leads to an additional term to  $\Delta\lambda$  that scales as  $1/T$ :

$$\frac{\Delta\lambda(T)}{\lambda_0} = a \frac{T}{T_c} + \frac{\beta}{4T}, \quad (2.20)$$

where  $\beta = \hbar v_f \left| \cos^3(\theta) - \sin^3(\theta) \right| / [6k_B \lambda_0]$ . The ABS thus contributes a small paramagnetic Meissner effect at low fields.

In the presence of a DC magnetic field in the Meissner state, the  $\delta$ -function is modified by the shift in the quasiparticle spectrum due to the Doppler shift, and becomes

$\delta(E + e\vec{v}_f \cdot \vec{A})$ , which leads to

$$\begin{aligned} \frac{\Delta\lambda(T, H)}{\lambda_0} &= a \frac{T}{T_c} + \frac{\beta}{4T} \cosh^{-2} \left[ \frac{\mu_0 e \lambda \vec{H} \cdot \vec{v}_f}{2k_B T} \right] \\ &\cong a \frac{T}{T_c} + \frac{\beta}{4T} \left[ 1 - \left( \frac{\mu_0 e \lambda \vec{H} \cdot \vec{v}_f}{2k_B T} \right)^2 \right], \quad \frac{\mu_0 e \lambda \vec{H} \cdot \vec{v}_f}{2k_B T} \ll 1, \end{aligned} \quad (2.21)$$

showing that the  $1/T$  term of  $\lambda$  is suppressed by the externally applied field. A characteristic field scale is introduced here:  $k_B T / \mu_0 e \lambda v_f = H_0 (T/T_c)$ , where  $H_0$  is of the order of thermodynamic critical field  $\mu_0 H_c = \Phi_0 / \lambda \xi$ . The  $1/T$  upturn in the penetration depth, and

its suppression due to the external DC magnetic field have been clearly observed by Carrington *et al.* in measurements of  $\lambda(T, H)$  on YBCO crystals with exposed [110] surfaces.

To explore the possibility of using our microscope to study this type of nonlinearity, I rewrite Eq. 2.21 in the perturbation limit ( $\frac{\mu_0 e \lambda \vec{H} \cdot \vec{v}_f}{2k_B T} \ll 1$ ). The contribution of ABS can be expressed as

$$\frac{\Delta\lambda_{ABS}(T, H)}{\lambda_0} \cong \frac{\beta}{4T} \left[ 1 - \left( \frac{HT_c}{2H_0T} \right)^2 \right], \quad (2.22)$$

assuming  $\vec{H} \cdot \vec{v}_f = H v_f$ . This is the change in  $\lambda$  due to the destruction of the ABS by an applied field  $H$  at low temperatures. It demonstrates a similar time-reversal symmetric (TRS) third order nonlinearity as seen in the NLME, although it has a very different temperature dependent pattern.

To express this ABS nonlinearity in the same manner as for NLME, I rewrite the equation as follows,

$$\begin{aligned} \frac{\lambda^2(T, H)}{\lambda^2(T, 0)} &= \left( \frac{\lambda_0 + \Delta\lambda(T, H)}{\lambda_0 + \Delta\lambda(T, 0)} \right)^2 \cong \left[ \frac{\lambda_0 \left( 1 + a \frac{T}{T_c} + \frac{\beta}{4T} - \frac{\beta}{4T} \left( \frac{HT_c}{2H_0T} \right)^2 \right)}{\lambda_0 \left( 1 + a \frac{T}{T_c} + \frac{\beta}{4T} \right)} \right]^2 \\ &\cong 1 - \frac{2}{1 + \frac{4T}{\beta} + \frac{4a}{\beta} \frac{T^2}{T_c}} \left( \frac{HT_c}{2H_0T} \right)^2 = 1 - \left( \frac{H}{H_{NL}(T)} \right)^2, \end{aligned} \quad (2.23)$$

which indicates a scaling field or current density, which scales with temperatures as

$$H_{NL}(T) = 2H_0(T/T_c)\sqrt{(1/2) + (2T/\beta) + (2aT^2/\beta T_c)}. \quad (2.24)$$

Measurement of this nonlinearity field/current scale can serve as the sign of the presence of Andreev bound states if observed by our near-field microwave microscope. I note that the d-wave NLME is not included in this expression.

It is also worth noting that in Barash's framework [60] of another TRSB order parameter, which is the surface magnetization, emerges in the ABS at temperatures below  $(\xi_0/\lambda_0)T_c \approx 0.01T_c$ . This order parameter modifies the penetration depth as  $\Delta\lambda(H)/\lambda \propto H^{-2/3}$ . However, the temperature range required to explore this effect is beyond my current capabilities.

#### 2.4 Another Potential TRSB Nonlinearity – Varma's proposal

The above ABS nonlinearities do not have any doping dependence. In contrast, Varma *et al.* [64] proposed a nonlinear mechanism present only in under-doped cuprates, not over-doped ones. In this model, Varma defines a quantum critical point in the HTSC phase diagram, and proposes the presence of 2D micro currents flowing along Cu-O co-valence bonds in the Cu-O plane (ab-plane) in HTSC for doping levels below the critical point. These currents are arranged so that there is no net flux observable in the global sense, but microscopically, time-reversal symmetry is broken. The onset of these currents is marked by the pseudo-gap temperature, which varies from  $\sim 100K$  to  $> 300K$  for YBCO, and they

persist to zero temperature. In other words, with doping levels below the critical point (which occurs approximately at optimal doping), the time-reversal symmetry is broken at temperatures below the pseudo-gap temperature, even in the superconducting state. According to Varma, such a broken symmetry should not be seen in over-doped HTSC.

To test this model, Varma also proposed an experiment to be done by Angular Resolved Photo Emission Spectroscopy (ARPES). Details can be found in Ref. [64] and [65]. Briefly speaking, the onset of the proposed TRSB mechanism is probed with ARPES using circularly (left and right) polarized light. Varma proposed a sophisticated ARPES arrangement, in which if the response measured from the HTSC sample with the left- and right-polarized light shows a difference, the time-reversal symmetry is broken.

Experiments done by Kaminski *et al.* based on Varma's idea claimed to support this proposal. However, another ARPES group, Borisenko *et al.* [66], following the same idea, but concluded that the proposed TRSB mechanism is not observed. While this is still a controversial issue, we believe that our microscope has promising potential to provide an independent way to test if this proposal is valid.[67]

## CHAPTER 3

### THE NONLINEAR SCALING CURRENT DENSITIES

As I mentioned in the previous chapter, nonlinearities in superconductors, especially high- $T_c$  superconductors, are of interest not only because of their implication for applications, but also because they give insights into the physics of these mysterious materials. However, it has been recognized that most of the work striving to find the most intrinsic nonlinear mechanisms in High-Temperature Superconductors (HTSC) has to face the much stronger nonlinear mechanisms caused by extrinsic features of the samples. For instance, the granular nature and inhomogeneity of the HTSC's lead to strong nonlinearities. Therefore, it becomes imperative to positively identify the cause of the observed nonlinear phenomena.

In the mid 1990's, Dahm and Scalapino [31] proposed an expression for the Nonlinear Meissner Effect (NLME) in terms of a scaling current density,  $J_{NL}$ , which is the de-pairing current density of the HTSC.

$$\frac{\lambda(J,T)^2}{\lambda(J,T=0)^2} \cong 1 + \left( \frac{J}{J_{NL}(T)} \right)^2, \quad J \ll J_{NL}(T) \quad (3.1)$$

This concept was later extended and used by various researchers [68,69] to identify the

dominant mechanism in their nonlinear measurements of HTSC's. It turns out to be very useful because this scaling current density should be measurement technique-independent, and provide a common ground for researchers to compare results obtained from various experimental approaches. In 2001, James C. Booth [69] used an algorithm to convert the results of his harmonic measurements into the scaling current density in Eq. 3.1. We have found that this algorithm can be applied to our experiment with some slight modifications. The details will be described in this chapter.

I note, however, that Booth's algorithm is only applicable in the superconducting state since the dominant nonlinear behavior is assumed to be inductive. This assumption is only true in the superconducting state for two reasons. First, there is very little energy dissipated, hence the resistive nonlinearity is not important. Secondly, most of the energy is stored in the kinetic energy of the current density, and its nonlinearity is dominated by that of the kinetic inductance and the super-fluid density. At temperatures above  $T_c$ , materials become very dissipative. Although there might be residual  $\sigma_2$  for  $T > T_c$  allowing super-current screening to exist in the sample, the electrodynamics are no longer dominated by the inductive response, but must include the dissipative channel. Therefore, for nonlinearities proposed to be present in the normal state or the pseudo-gap state, for example, Varma's micro current model, this algorithm may not be sufficient. Another algorithm treating the nonlinear resistance as an additional source is needed. In my research, I focus on the nonlinear phenomena observed in the superconducting state.



## 3.1 Time-Reversal Symmetric (TRS) Nonlinearities

### 3.1.1 Introduction

Nonlinearities in high- $T_c$  superconductors generally result from the perturbation and suppression of the super-fluid density, so that the electromagnetic response of the superconductor is no longer linear. The simplest way of expressing the effect of various nonlinearities in superconductors is to expand the perturbed quantity, i.e. the super-fluid density, in terms of the perturbing quantity, i.e. external currents or fields.

For the Time-Reversal Symmetric (TRS) nonlinearities, the super-fluid density is written as

$$\rho_s(T, J) / \rho_s(T, 0) \cong 1 - (J / J_{NL}(T))^2 + \dots,$$

where  $\rho_s$  is the super-fluid density, and  $(J / J_{NL}(T))^2$  is the leading perturbing term, which preserves the Time-Reversal Symmetry. I justified this general approach on microscopic grounds in Chapter 2. It is worth noting that since I am treating the nonlinearities as a perturbation to the super-fluid density by external currents,  $J$  must be much smaller than  $J_{NL}$  to validate the truncation of the expansion. Further analysis shows that  $J_{NL}(T)$ , which serves as a scaling current density, is of the order of the critical current of the responsible nonlinear mechanism [29-32].

As an example, consider the nonlinear Meissner effect. In this case,  $J_{NL}(T)$  is the de-pairing critical current density of the superconductor. This  $J_{NL} \approx 10^9$  A/cm<sup>2</sup> for cuprates, and  $10^7$  A/cm<sup>2</sup> for low- $T_c$  superconductors, for  $0.3T_c < T < 0.7T_c$ . However, at lower temperatures, this quantity behaves differently in s- and d-wave superconductors (see Fig. 3.1). While  $J_{NL}(T)$  increases as  $T \rightarrow 0$  in s-wave superconductors, it decreases in d-wave superconductors due to the presence of the nodes in the energy gap on the Fermi surface, as discussed in Chapter 2.

The Ginzburg-Landau (GL) theory can also be used to estimate  $J_{NL}(T)$  for the NLME. While the magnitude of this estimate might be trustworthy, it only gives a reliable description near  $T_c$ . On the other hand, for a 1D Josephson junction array combined in series, Willemsen [68] found that  $J_{NL}$  is around  $10^5$ - $10^6$  A/cm<sup>2</sup> for  $0.3T_c < T < 0.7T_c$  (See Fig. 3.1). These different predictions mean that if one can extract  $J_{NL}(T)$  from experimental results, the nonlinear mechanism responsible for the observed behavior can be identified.

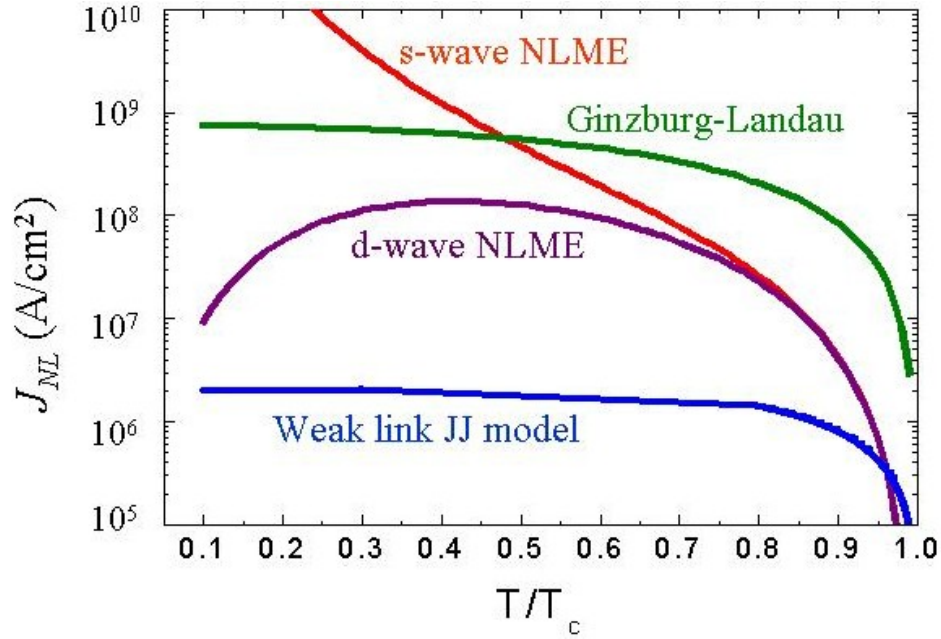


Fig. 3.1 Schematic representation of the expected  $J_{NL}(T)$  for various nonlinear mechanisms in HTSC. Weak-link model is described in Ref. [68].

### 3.1.2 Algorithm for Extracting $J_{NL}$ from Experimental Data

The measured quantities in my experiment are the harmonics generated from the sample when I apply a microwave current at frequency  $\omega = 2\pi f$ . To proceed, I must find a way to relate  $J_{NL}$  to my experimental harmonic data. To do this, I adopt Booth's algorithm [69]. The essential assumption is that the nonlinear reactance of a superconductor dominates its nonlinear electromagnetic response. This assumption was later confirmed by Booth's experimental work [70], and that of other groups.

Following this algorithm, the nonlinear reactance (due to a nonlinear inductance in our case) of the superconductor can be calculated through the energy stored in the inductance:

$$l = \mu_0 \iint_{\text{cross section}} (H^2 + \lambda^2 J^2) ds \bigg/ \left( \iint_{\text{cross section}} \vec{J} \cdot d\vec{s} \right)^2, \quad (3.2)$$

where  $l$  is the inductance per unit length,  $\lambda$  is the penetration depth,  $J$  is the current density, and  $d\vec{s}$  is an element of cross-sectional area. The cross-sectional integral is on the surface indicated in Fig. 3.2. The integral in the denominator is the total current flowing through the cross section. The first term in the numerator leads to the field (geometrical) inductance of the superconductor and is determined by the magnetic field configuration in the superconductor due to the Meissner screening. This inductance is not changed significantly by nonlinearities in superconductors [71]. However, the second term is the kinetic inductance of the superconductor and it is determined by the current distribution and the penetration depth (super-fluid density). We can write:

$$\frac{\lambda^2(T, J)}{\lambda^2(T, J=0)} = \frac{\rho_s(T, J=0)}{\rho_s(T, J)} \cong 1 + \left( \frac{J}{J_{NL}(T)} \right)^2, \quad J \ll J_{NL}(T).$$

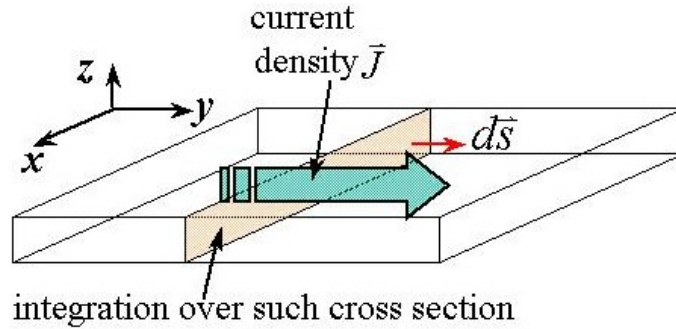


Fig. 3.2 The inductance per unit length of a superconducting slab is estimated by integrals over the cross section perpendicular to the current direction.

To obtain the total inductance of the superconductor, we integrate  $l$ , the inductance per unit length, over the  $y$ -direction. For  $J \ll J_{NL}(T)$ , the total inductance is written as

$$L \cong \mu_0 \int \left[ \frac{\left( \iint_{\text{cross section}} (H^2 + \lambda^2(T)J^2) ds \right) + \left( \iint_{\text{cross section}} \frac{\lambda^2(T)J^4}{J_{NL}^2(T)} ds \right)}{\left( \iint_{\text{cross section}} \vec{J} \cdot d\vec{s} \right)^2} \right] dy, \quad (3.3)$$

$$\equiv L_0 + \Delta L I_0^2,$$

where  $I_0 \equiv \text{Max} \left( \iint_{\text{cross section}} \vec{J} \cdot d\vec{s} \right)$  is the total current flowing through a cross section right

beneath the bottom of the loop probe,  $L_0$  is the linear inductance, and  $\Delta L$  is the coefficient of the current-dependent inductance:

$$L_0 = \mu_0 \int \frac{\iint_{\text{cross section}} (H^2 + \lambda^2(T)J^2) ds}{\left( \iint_{\text{cross section}} \vec{J} \cdot d\vec{s} \right)^2} dy, \text{ and}$$

$$\Delta L = \frac{\mu_0 \lambda^2(T)}{I_0^2 J_{NL}^2(T)} \int \frac{\iint_{\text{cross section}} J^4 ds}{\left( \iint_{\text{cross section}} \vec{J} \cdot d\vec{s} \right)^2} dy. \quad (3.4)$$

All of this assumes that the penetration depth  $\lambda$  and the scaling current density  $J_{NL}$  are both uniform over the cross-section integration. I have also used the simplified notation  $\lambda(T) = \lambda(T, J=0)$  in the above equations.

In my experiment, I drive the superconducting sample with an induced microwave current, and measure the harmonic content in the potential difference. Using a simple AC circuit model with a driving current source  $I(t) = I_0 \sin(\omega t)$ , at frequency  $f = \omega/2\pi$ , I can model the potential difference generated in the superconducting sample as

$$V(t) = L \frac{dI(t)}{dt} = L_0 \frac{dI(t)}{dt} + (\Delta L) I^2 \frac{dI(t)}{dt}. \quad (3.5)$$

From this results, we find the third harmonic content is  $V_{3f}(t) = -\frac{\omega(\Delta L) I_0^3}{4} \cos(3\omega t)$  (see

Appendix A). I note that there is a  $\pi/2$  phase shift in the harmonic content ( $\sin \rightarrow \cos$ ).

This is because of the assumed dominant inductive response of the sample. If the nonlinear response is dominated by the resistive channel, then no phase shift is expected. This suggests that the measurement of relative phase between the driving signal and the harmonic response will give the relative contribution of the inductive and resistive nonlinearities. This would be a different measurement but may be pursued in the future.

I measure  $V_{3f}$  by monitoring the third harmonic power  $P_{3f}$  using a coaxial transmission line system. Assuming for the moment that all of the signal generated in the sample couples back to the transmission line, I can then write

$$P_{3f} = \frac{|V_{3f}|^2}{2Z_0} = \frac{|\omega(\Delta L) I_0^3 / 4|^2}{2Z_0} = \left| \frac{\omega \mu_0 \lambda^2(T) I_0}{4 J_{NL}^2(T)} \int \frac{\iint_{cross\ section} J^4 ds}{\left( \iint_{cross\ section} \vec{J} \cdot d\vec{s} \right)^2} dy \right|^2 \times \frac{1}{2Z_0}, \quad (3.6)$$

where  $Z_0$  is the characteristic impedance of the transmission line and the matched spectrum analyzer input impedance.

The above equation can be simplified if the thickness of samples are less than their penetration depth. The current can then be treated as uniformly distributed in thickness, and the integrals of the current density  $J$  can be rewritten as integrals of the surface current density  $K$ :

$$\iint_{\text{cross section}} J^4 ds = \iint_{\text{cross section}} \left( \frac{K}{t} \right)^4 t dx = \frac{1}{t^3} \int K^4 dx, \text{ and} \quad (3.7.1)$$

$$\iint_{\text{cross section}} \bar{J} \cdot d\bar{s} = \iint_{\text{cross section}} \left( \frac{K_y}{t} \right) t dx = \int K_y dx, \quad (3.7.2)$$

where  $t$  is the film thickness, and  $K$  is the surface current density. With this simplification, Eq. 3.6 becomes

$$P_{3f} = \left( \frac{\omega \mu_0 \lambda^2(T)}{4t^3 J_{NL}^2(T)} \right)^2 \Gamma^2 / 2Z_0, \quad (3.8a)$$

$$\text{where } \Gamma \equiv I_0 \int \frac{\int K^4 dx}{\left( \int K_y dx \right)^2} dy. \quad (3.8b)$$

I note that  $\Gamma$  serves as a figure of merit for the sensitivity of my system in measuring TRS nonlinearities. I estimate  $\Gamma$  using High-Frequency-Structure-Simulator (HFSS) software by Ansoft, which will be discussed later. The figure of merit  $\Gamma$  depends on the

power level and the geometry of the probe-sample coupling (the probe size and probe/sample distance). A larger value of  $\Gamma$  means that a greater amount of third harmonic power ( $P_{3f}$ ) is measured for a given nonlinear source ( $J_{NL}$ ). Hence we want  $\Gamma$  to be as large as possible.

Equation 3.8 implies that sensitivity to nonlinearities will be improved by reducing the film thickness  $t$ , increasing the frequency  $\omega$ , increasing the current density  $K$ , approaching closer to  $T_c$  (where  $\lambda(T)/J_{NL}(T)$  is large), and by decreasing the volume in which the current flows. It is worth mentioning that an independent calculation done by Pestov *et al.* [72] for this situation demonstrates the same relations between  $P_{3f}$ ,  $J_{NL}$ , the film thickness  $t$ , and the penetration depth  $\lambda$ . Additionally, he also shows that  $P_{3f} \propto 1/h^6$ , where  $h$  is the probe/sample distance. Thus we expect that the microscope is more sensitive when the probe is closer to the sample, which is included in my Eq. 3.8b for  $\Gamma$ .

I'm also aware of an independent work by C. Collado, J. Mateu, and J. M. O'Callaghan. [73,74] They calculated the expected the intermodulation distortion and third harmonic generation from superconducting films in certain patterned geometries, based on Eq. 2.12.

## 3.2 Time-Reversal Symmetry-Breaking (TRSB) Nonlinearities

### 3.2.1 Introduction



A similar analysis can be made for the TRSB nonlinearities. Once again I assume the inductive response dominates the nonlinear behavior of TRSB mechanisms in superconductors. As long as the TRSB nonlinearities manifest themselves in a way that only slightly modifies the super-fluid density, the super-fluid density can be written as

$$\frac{\rho_s(T, J)}{\rho_s(T, 0)} \cong 1 - \frac{J}{J_{NL}'(T)} - \left( \frac{J}{J_{NL}(T)} \right)^2, \quad (3.9)$$

where this is valid only for  $J \ll J_{NL}(T), J_{NL}'(T)$ , where  $J / J_{NL}'(T)$  is the leading perturbing term, which breaks Time-Reversal Symmetry, and  $J_{NL}'(T)$  is a new scaling current density, introduced to quantify the mechanism responsible for TRSB nonlinearities.

While  $J_{NL}'(T)$  represents the strength of various TRSB nonlinearities quantitatively, the theoretical foundation is not available for relating the magnitude of  $J_{NL}'(T)$  to any proposed TRSB mechanisms. Our intuitive thought is that the NLME is modified due to the presence of spontaneous currents  $J_{TRSB}(T)$  from the TRSB mechanisms. This suggests that instead of  $(J / J_{NL}(T))^2$ , the nonlinear term becomes

$$\frac{\rho_s(T, J)}{\rho_s(T, 0)} \cong 1 - \left( \frac{J + J_{TRSB}(T)}{J_{NL}(T)} \right)^2 \cong 1 - \frac{2J J_{TRSB}(T)}{J_{NL}(T)^2} - \left( \frac{J}{J_{NL}(T)} \right)^2. \quad (3.10)$$

Comparing Eq. 3.9 and 3.10, one sees that the  $J_{NL}'(T)$  in Eq. 3.9 is replaced by  $J_{NL}(T)[J_{NL}(T)/2J_{TRSB}(T)]$  in Eq. 3.10. One might expect that  $J_{NL}'(T) > J_{NL}(T)$  because the TRSB mechanisms are likely to produce a spontaneous current that is lower than the

de-pairing critical current, i.e.  $2J_{TRSB}(T) < J_{NL}(T)$ . This is confirmed in our data discussed in Chapter 6.

### 3.2.2 Algorithm for Extracting $J_{NL}'$ from Experimental Data

To extract  $J_{NL}'$  from my data, I used essentially the same algorithm as for TRS nonlinearities. Now since the modulation of super-fluid is represented by two nonlinear terms, the calculation for the nonlinear inductance becomes,

$$L \cong \mu_0 \int \left[ \frac{\left( \iint_{cross\ section} (H^2 + \lambda^2(T)J^2) ds \right) + \left( \iint_{cross\ section} \frac{\lambda^2(T)J^3}{J_{NL}'(T)} ds \right) + \left( \iint_{cross\ section} \frac{\lambda^2(T)J^4}{J_{NL}^2(T)} ds \right)}{\left( \iint_{cross\ section} \vec{J} \cdot d\vec{s} \right)^2} \right] dy$$

$$\equiv L_0 + (\Delta L') I_0 + (\Delta L) I_0^2, \quad (3.11)$$

where this is valid only for  $J < J_{NL}(T), J_{NL}'(T)$ , and where  $\Delta L'$  is the term related to TRSB nonlinearities. Using the same AC circuit model, and this additional nonlinear term in the inductance, the potential difference now contains not only the third, but also the second harmonic content,  $V_{2f}(t) = \frac{\omega(\Delta L') I_0^2}{2} \text{Sin}(2\omega t)$ , obtained by Fourier

Transformation (see Appendix A for details).

Consequently, if all signals couple back to the transmission line, the second harmonic power in the microwave circuit (without attenuation and amplification) is

$$\begin{aligned}
P_{2f} &= \frac{|V_{2f}|^2}{2Z_0} = \frac{|\omega(\Delta L')I_0^2/2|^2}{2Z_0} = \frac{\omega\mu_0\lambda^2(T)I_0}{4J_{NL}'(T)} \int \left[ \frac{\iint_{cross\ section} J^3 ds}{\left( \iint_{cross\ section} \vec{J} \cdot d\vec{s} \right)} \right] dy \times \frac{1}{2Z_0} \\
&= \left( \frac{\omega\mu_0\lambda^2(T)}{4t^2 J_{NL}'(T)} \right)^2 \frac{\Gamma'^2}{2Z_0},
\end{aligned} \tag{3.12}$$

where  $\iint_{cross\ section} J^3 ds = \int K^3 dx / t^2$  for  $t \ll \lambda$ , and  $\Gamma' \equiv I_0 \int \left( \int K^3 dx / \left( \int K_y dx \right)^2 \right) dy$ .

I note that  $\Gamma'$  serves as a figure of merit for the sensitivity of my system to measuring TRSB nonlinearities. I also use the HFSS software to estimate  $\Gamma'$ , as discussed later. Again I want  $\Gamma'$  to be as large as possible to maximize the measured  $P_{2f}$  for a given TRSB nonlinear source ( $J_{NL}'$ ).

Equation 3.12 for  $P_{2f}$  suggests that I should use thinner films, higher frequencies, larger current density  $K$ , temperatures closer to  $T_c$ , and concentrating currents in a smaller volume (smaller probes as we shall see below). These are the same limits I noted above for maximizing the sensitivity to  $J_{NL}$  in  $P_{3f}$ .

### 3.3 Predicted harmonics and measured harmonics: coupling and amplification issues

The harmonic signals generated by a sample have been evaluated above. However, before this signal is measured, it must couple from the sample to the probe. It then gets attenuated

in the coaxial transmission line and filters, and amplified by the microwave amplifiers. To estimate the relation between harmonics in the sample, and the measured harmonic data, we must characterize our transmission line system.

When microwave signals are sent to the sample, microwave currents are induced on the sample surface. It is important to know the magnitudes and distribution of these currents, so that we can determine what will be generated by the sample. On the other hand, before the signal enters the spectrum analyzer, it is picked up via the coupling between the loop probe and sample. I use an analytical model calculated with Mathematica™, and a numerical model simulated by HFSS, to estimate the microwave current distribution and the probe/sample magnetic coupling, and derive other quantities needed to analyze our data.

### 3.3.1 Analytical Model of Loop/Sample Interactions Calculated by Mathematica™

My model consists of an ideal circular loop carrying a current  $I$ , situated above a perfectly conducting plane with the loop axis parallel to the plane, as shown in Fig. 3.3.

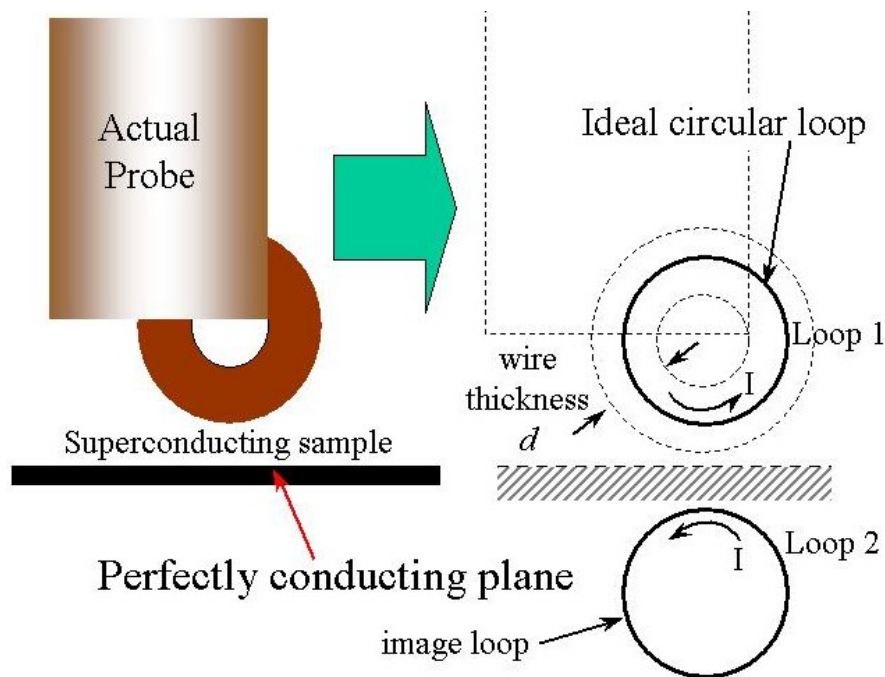


Fig. 3.3 Ideal circular loops represent the physical loop and a perfect conducting plane (image loop).

Using the method of images, the perfectly conducting plane can be replaced with another ideal circular loop, identical to the original one, and carrying currents flowing in the same direction (both clockwise or counter-clockwise) to satisfy the boundary condition that there are only tangential magnetic fields on the surface. In our work, different loop probes are made of different coaxial cables, which have different wire-thickness and outer diameters; hence forming different loop sizes. The ideal loops are assumed to be located at the center of the inner-conducting wire, as indicated in Fig. 3.3, and the distance between the ideal loops and the perfect conducting plane is restricted by the wire-thickness  $d$ . Listed in Table 3.1 is a summary of the probes that I analyzed with help of Greg Ruchti using HFSS

software. Additionally, in my experiment, the bottom of the wire loop is  $12.5\mu\text{m}$  away from the sample surface, separated by a Teflon<sup>TM</sup> sheet, so that the bottom of the ideal loop,

Table 3.1 Important dimensions of simulated coaxial cables.  
 \* These coaxial cables are not commercially available.

Coaxial Cable outer conductor – outer diameter (inch)	Wire Thickness $d$ ( $\mu\text{m}$ )	Radius of the Ideal Loop ( $\mu\text{m}$ )
.085	500	665
.034	200	270
.020	130	172.5
.010*	65	86.25
.005*	32.5	43.125

where the current is flowing, is  $(d/2)+12.5\mu\text{m}$  away from the plane. We can use this model to calculate analytically the current distribution (and therefore the figures of merit,  $\Gamma$  and  $\Gamma'$ ), and loop/sample mutual inductance. These results will be summarized later along with numerical results obtained from HFSS.

### 3.3.2 Numerical Simulation using the High Frequency Structure Simulator (HFSS)

The numerical model simulated by HFSS were done in collaboration with undergraduates Greg Ruchti and Mark Pollak. This model consists of a coaxial cable with the inner

conductor forming a semi-circular loop to the outer conductor at the end of the cable. The bottom of the loop is  $12.5 \mu\text{m}$  above an infinite perfectly conducting plane. The presence of the Teflon™ sheet is ignored in this setup (see Fig. 3.4). A driving port is placed at the top of the coaxial loop probe, and I apply a 1W microwave signal at 6.5 GHz. The coaxial cable and sample are placed in a box, whose walls are defined to be radiation-absorbing boundaries. This means that electromagnetic waves don't return once they propagate to the boundaries. The size of the box was systematically increased until the amount of radiated power through its walls no longer changed.

The HFSS program solves Maxwell's equations at finite frequencies subject to the constitutive relations of the materials, and returns the electric and magnetic field configurations in all space and on all surfaces, and the current distributions on all surfaces. It also has a built-in calculator capable of performing most mathematical manipulations (e.g. cross products, dot products, surface integrals, volume integrals, etc.) on these quantities. In particular, HFSS can calculate all electromagnetic quantities in this setup, including the spatial distribution of the microwave electric and magnetic fields, surface currents flowing on all surfaces, etc. A more detailed description of HFSS simulations can be found in Greg Ruchti's senior thesis [75].

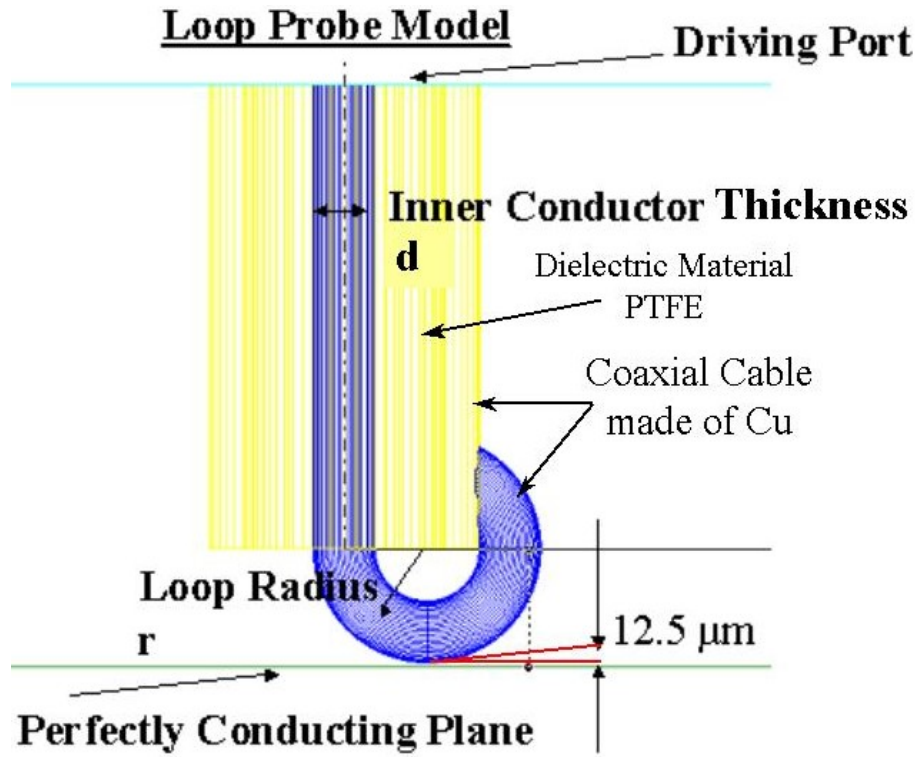


Fig. 3.4 Setup in HFSS to simulate the probe/sample interaction.

### 3.3.3 Estimations of the Figures of Merit: $\Gamma$ and $\Gamma'$

As described in the previous sections, the figures of merit for third and second harmonic measurements,  $\Gamma$  and  $\Gamma'$ , are defined by:

$$\Gamma \equiv I_0 \int \left( \frac{\int K^4 dx}{\left( \int K_y dx \right)^2} \right) dy, \text{ and} \quad (3.13)$$

$$\Gamma' \equiv I_0 \int \left( \frac{\int K^3 dx}{\left( \int K_y dx \right)^2} \right) dy, \quad (3.14)$$



where  $I_0$  is the total current,  $\int K_y dx$  is the total current flowing through the cross section, and  $K$  is the surface current. Since  $\int K_y dx$  might vary along the  $y$ -direction, we choose the maximum of  $\int K_y dx$ , which is beneath the center of the loop, to determine  $I_0$ .

Using the two-identical-ideal-loop analytical model, the surface currents on the plane in the middle of two loops can be easily calculated from the magnetic fields  $H$ , and the boundary conditions that there are only in-plane magnetic fields on the surface. The current distribution is used to calculate  $\Gamma$  and  $\Gamma'$ , and the results are tabulated in Table 3.2.

On the other hand, the HFSS software can also directly calculate the surface currents  $K$  flowing on the perfectly conducting plane. The results of HFSS simulations for the surface current density on the sample show a clear circulating current pattern as shown in Fig. 3.5. To properly calculate the total current, the line integrals  $\int K_y dx$  are performed to the points where the current is about to turn from forward to backward (See the Integration Line in Fig. 3.5). The other integrals in Eq. 3.13 and 3.14 are done with the calculator in HFSS. It is noted that in HFSS, the driving power is fixed at 1W, and the figures of merit  $\Gamma$  and  $\Gamma'$  are power dependent quantities. Therefore, to calculate the  $\Gamma$  and  $\Gamma'$  at the power used in my experiment, we use the scaling relation  $K \propto \sqrt{P}$ . The simulated results of  $\Gamma$  and  $\Gamma'$  from both analytical and numerical models are summarized in Table 3.2, and are discussed later.

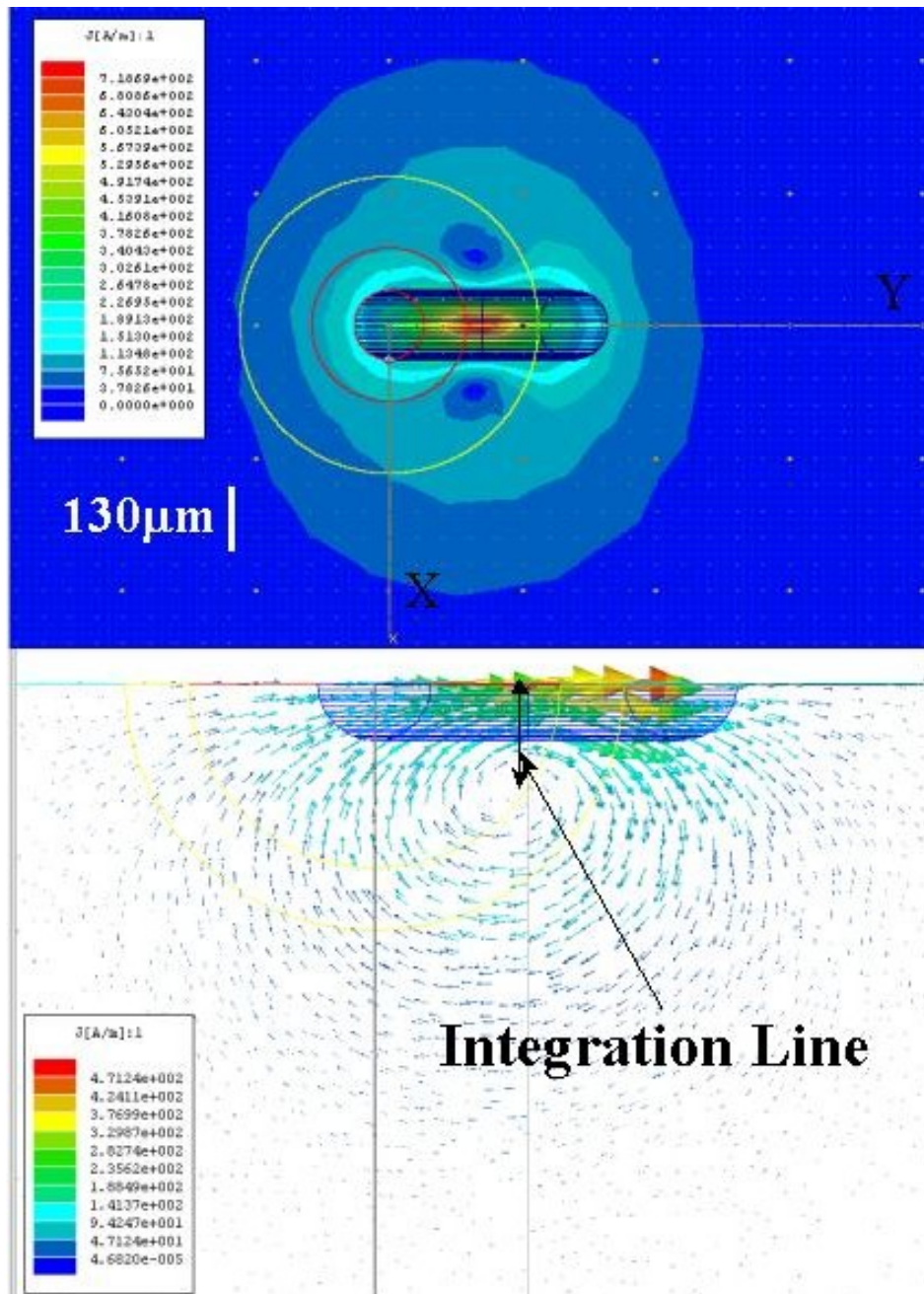


Fig. 3.5 Microwave current distribution  $|K|$  (A/m) induced on a perfectly conducting plane by a 0.034" loop probe. Inset is a vector plot of the surface currents, which show a circular circulation pattern mentioned in the text.

### 3.3.4 Estimations of the Probe/Sample Coupling

Assuming the self inductance of the loop probe is  $L$ , and the mutual inductance between the loop and sample is  $M$ , the voltage signal propagates from the sample to the probe with reduction by a factor of  $M/L$ , and the power signal by  $(M/L)^2$ . To estimate the probe/sample coupling, we use both the analytical and numerical models to calculate this ratio.

In the analytical model, the mutual inductance between loop 1 & 2 in Fig. 3.3 can be calculated exactly using the well-known result [76]:

$$M = \frac{\mu_0}{4\pi} \oint \oint \frac{d\vec{l}_1 \cdot d\vec{l}_2}{|\vec{x}_1 - \vec{x}_2 + \vec{R}|}, \quad (3.15)$$

where  $d\vec{l}_1$ ,  $d\vec{l}_2$ ,  $\vec{x}_1$ ,  $\vec{x}_2$ , and  $\vec{R}$  are indicated as in Fig 3.6.

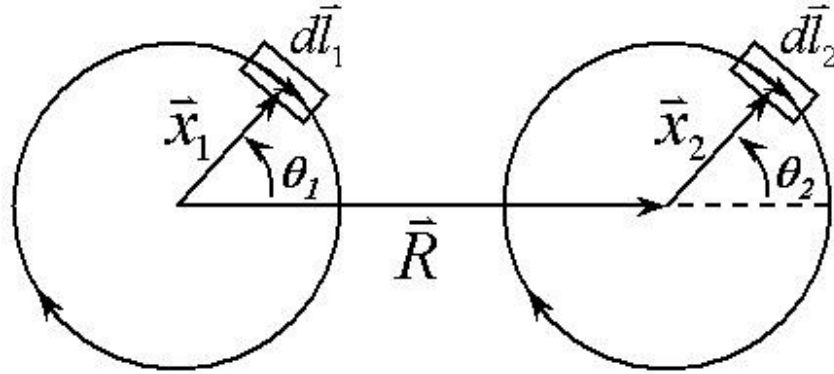


Fig. 3.6 The configuration of two circular loops for calculating the mutual inductance by Eq. 3.15.

While Eq. 3.15 is a general expression for two loops with arbitrary shapes and orientations, we can derive an analytical expression for the configuration shown in Fig. 3.6:

$$M(r) = \frac{\mu_0}{4\pi} \iint \frac{-r^2 \cos(\theta_1 - \theta_2)}{\sqrt{2r^2[1 - \cos(\theta_1 - \theta_2)] + 2rR[\sin\theta_2 - \sin\theta_1] + R^2}} d\theta_1 d\theta_2,$$

where  $r$  is the radius of the loops,  $R$  is the distance between the centers of the loops, and  $\theta_1$  and  $\theta_2$  are as specified in Fig. 3.6.

The self-inductance of the loop  $L_{loop}$  is approximately  $L_{loop} \approx 1.25\mu_0 a$  [23], where  $a$  is the inner diameter of the loop. The results for  $M$  and  $L_{loop}$  are given in Table 3.2.

The calculation of  $M/L_{loop}$  in HFSS, is a little bit more complicated. As with the analytical model, we use an image loop to represent the sample, as shown in Fig 3.7. The driving port is on the coaxial cable supporting the original loop, sending microwave signals at 6.5 GHz with 1W of input power.

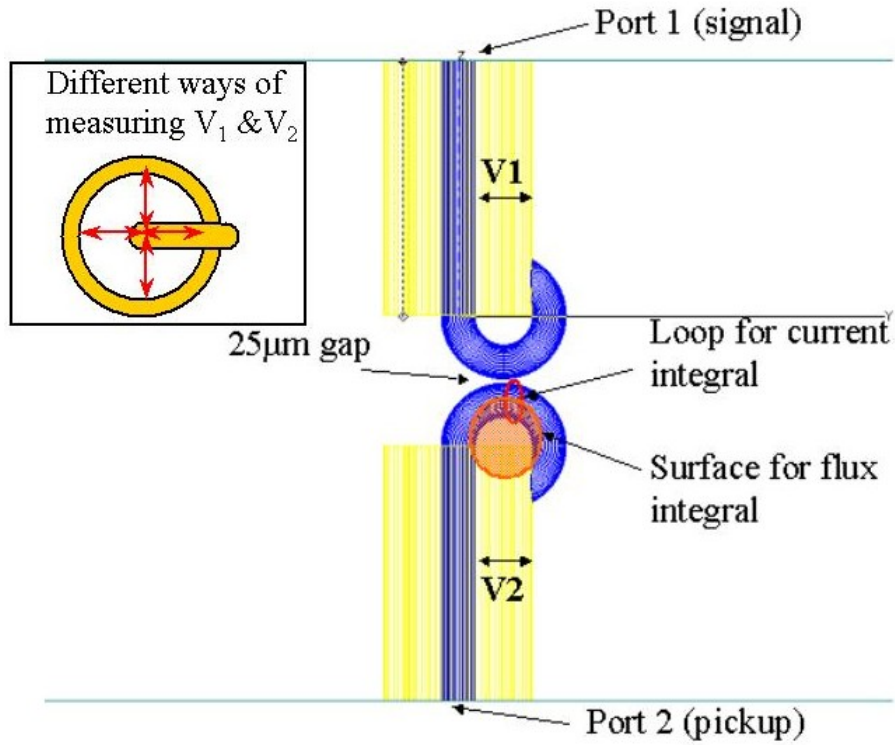


Fig. 3.7 Setup for estimating the coupling coefficient  $M/L_{loop}$  using HFSS. Red arrows in the inset show different ways of measuring  $V_1$  and  $V_2$  (measured at the ends of arrows), which result in slightly different  $M/L_{loop}$ .

The image loop acts as a pick-up loop, and the coupling between two loops,  $M/L$ , is represented by the ratio of the potential differences in each loop,

$$\frac{M}{L} = \frac{V_2}{V_1}, \quad (3.16)$$

where  $V_2$  and  $V_1$  are the potential differences between the inner and outer conductors of the image loop and original loop, respectively. To measure  $V_2$  and  $V_1$ , measure-points are put on the inner and outer conductors, and HFSS calculates the potential difference between

these two points. However, we found that  $V_2$  and  $V_1$  vary somewhat depending on the locations of these points (indicated in the inset of Fig. 3.7). We thus find a range of values for  $M/L$  for each probe. We have seen this effect on numerous occasions with HFSS and attribute it to the finite-element mesh that is used to discretely solve Maxwell's equations.

The results of  $M/L$  calculated from the analytical model and HFSS are summarized in Table 3.2. It is noted that the analytical results show  $M/L$  decreases for smaller loop probes, while the results from HFSS don't change much with loop dimension. To understand this difference, we must consider the difference between the real probe/sample arrangement and the setup in the analytical model. In reality, the probe and the sample are separated by a  $12.5\mu\text{m}$  thick Teflon<sup>TM</sup> sheet, and the loop wire has finite thickness  $d$ . Since the ideal circular loop is placed at the center of the loop wire, the closest distance between these two loops is  $2(12.5\mu\text{m} + d/2)$ . While it is true that when the probe size gets smaller, the wire thickness also gets smaller, the closest distance between these two loops is never less than  $25\mu\text{m}$ . Therefore, as the probe gets smaller, the two loops in the analytical model get farther away in a relative sense; hence the weaker coupling. On the other hand, in HFSS, there is always a significant part of the current flowing on the bottom of the wire, which is always  $25\mu\text{m}$  apart from its image currents. This helps to maintain the coupling within a certain range. This difference will also affect the calculation for  $\Gamma$  and  $\Gamma'$ . In HFSS, the total induced surface current does not change much among the various sizes of probes due to the more-or-less constant coupling, which is not true in the analytical model. Therefore,

to make a relevant comparison between  $\Gamma$  and  $\Gamma'$  calculated from the analytical model and HFSS, the surface currents calculated by the analytical model are multiplied by a factor to maintain a constant total current for all probes. Table 3.2 and Fig. 3.8 show the trends for  $\Gamma$  and  $\Gamma'$  with the radius of the ideal loop probe. The comparison shows a pretty good agreement in the trend toward larger  $\Gamma$  and  $\Gamma'$  for smaller probes, though the details are different.

Table 3.2 Simulated figures of merit ( $\Gamma$  and  $\Gamma'$ ) and coupling coefficient ( $M/L$ ) by analytical (Mathematica™) and HFSS models for different probe sizes.

Outer conductor Outer Diameter (inch)	$\Gamma$ at 1W ( $A^3/m^2$ )		$\Gamma'$ at 1W ( $A^2/m$ )		$M/L_{loop}$ (%)		$K_{max}$ (A/m) Input: 1W HFSS
	Analytical	HFSS	Analytical	HFSS	Analytical	HFSS	
.085	2200	9800	16.7	62.8	3.35	2.8 - 3.7	300
.034	10400	31200	34.8	106.4	3.12	3.13 ~ 3.67	500
.020	23300	37900	52.1	99.7	2.89	2.6 ~ 3.8	800
.010	66100	52100	85.2	95.3	2.40	–	–
.005	161300	166200	129.3	231.3	1.72	–	–

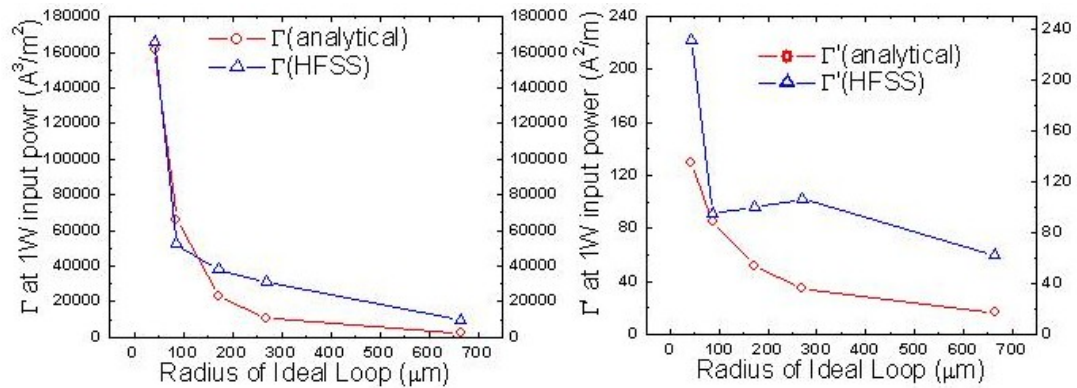


Fig. 3.8 Plot of  $\Gamma$  and  $\Gamma'$  calculated by both the analytical model and HFSS for various probes. Both assume 1W input power.

### 3.3.5 Estimations of Attenuation and Amplification in the Microwave Circuit

The final step to relate our measured harmonic powers to the nonlinearity current density scales is to characterize the attenuation (or gain) of our microwave measurement system.

The microwave signals sent from the synthesizer are attenuated by the coaxial cable, low-pass filters, and directional coupler before reaching the loop probe (see Fig. 1.10). This part of the circuit was characterized by using an Agilent 8722D vector network analyzer through calibrated measurements of  $S_{21}$  in a two-port measurement. I found that the drive signals around 6.5 GHz ( $f$ ) are attenuated by  $\sim -2$  dB while traveling from the source to the probe. Then the signals are reduced by the probe/sample coupling as discussed previously before entering the sample. After the harmonic signals generated on the sample surface are picked up by the loop probe, they propagate along the transmission line through a directional coupler, through two high-pass filters, and two amplifiers, and are then



measured by the spectrum analyzer. I characterized the circuit at 13 GHz ( $2f$ ) and 19.5 GHz ( $3f$ ), where I found the total gain of  $\sim 60$  dB, and  $\sim 52$  dB, respectively.

Considering both the reduction due to the coupling, and the enhancement from the measurement system, the locally generated second and third harmonic signals are enhanced (compared to the signals generated in the sample) by  $\sim (3\%)^2 \times 10^6 = 900$  times and  $\sim (3\%)^2 \times 10^{5.2} \cong 142.6$  times when they are measured by the spectrum analyzer at 13 GHz ( $2f$ ) and 19.5 GHz ( $3f$ ), respectively. This conversion is used to estimate the power level of the harmonics generated in the sample. Using Eqs. 3.8 and 3.12, and the calculated results for  $\Gamma$  and  $\Gamma'$ , we can estimate  $J_{NL}$  and  $J_{NL}'$ , respectively. This will be further discussed in Chapter 5.

## CHAPTER 4

# MICROWAVE NONLINEARITIES OF THE YBCO BI-CRYSTAL GRAIN BOUNDARY

### 4.1 Introduction

As I mentioned in Chapter 1 and 2, the goal of this project is to overcome the obstacles that conventional microwave measurements encounter in studying nonlinear properties of superconductors. Many experiments have studied the intermodulation power, harmonic generation, or the nonlinear surface impedance of superconductors as a function of applied microwave power [77,78,79]. However, most nonlinear experiments are done with resonant techniques, which by their nature study the averaged nonlinear response from the whole sample rather than locally. Such techniques usually have difficulty in either avoiding edge effects, which give undesired vortex entry, or in identifying the microscopic nonlinear sources. A technique that is capable of locally measuring nonlinear properties of samples would prove very helpful for identifying nonlinear mechanisms. In addition, most existing experimental techniques focus on 3<sup>rd</sup> order nonlinearities, which can be conveniently studied by sensitive intermodulation techniques, but rarely address the 2<sup>nd</sup> order nonlinear response.

We think that the near-field microwave microscope is one solution to this challenge. In prior work in our group, Hu *et al.* [80] studied the “local” and “global” intermodulation signal from a high- $T_c$  superconducting microwave resonator using a scanned electric field pick-up probe. However, the local measurements were actually a superposition of nonlinear responses that were generated locally but propagated throughout the microstrip and formed a resonant standing-wave pattern. To avoid this loss of spatial information, I have developed a non-resonant near-field microwave microscope, to non-destructively measure the local harmonic generation from un-patterned samples. Details of this microscope can be found in Fig. 1.10 and Chapter 1.

In this chapter, I present measurements done by this technique to locally characterize 2<sup>nd</sup> and 3<sup>rd</sup> order nonlinearities through spatially localized harmonic generation. The nonlinear mechanism responsible for this work is the Josephson nonlinearity in a long  $\text{YBa}_2\text{Cu}_3\text{O}_{7-\delta}$  (YBCO) bi-crystal grain boundary. It should be noted that there is another work of nonlinear microwave microscopy similar to our setup [72,81]. Instead of forming a loop shorting the inner and outer conductors, they use a straight wire connecting the inner and outer conductors. Although the work is similar, it was done quite independently from our work.

## 4.2 Sample

To evaluate the ability of the nonlinear near-field microwave microscope to distinguish extrinsic local nonlinear features, I measured the local nonlinear response of an artificially made nonlinear feature: a single isolated YBCO bi-crystal grain boundary. The grain boundary shows weak-link Josephson nonlinearity at intermediate temperatures  $0 < T/T_c < 0.9T_c$ . The sample is a  $500\text{\AA}$  thick YBCO thin film deposited by pulsed laser deposition on a  $10\text{ mm} \times 10\text{ mm}$  bi-crystal  $\text{SrTiO}_3$  substrate with a  $30^\circ$ -tilt mis-orientation angle. The distance between the loop probe and the sample is fixed by a  $12.5\mu\text{m}$  thick Teflon<sup>TM</sup> sheet placed between them.

I first measured the temperature dependent 3rd order harmonic power ( $P_{3f}$ ) both above the grain boundary (GB) and far away from the grain boundary (non-GB), as shown in Fig. 4.1(a). The input microwave frequency was  $\sim 6.5\text{ GHz}$  at  $8\text{ dBm}$ , and the loop probe was made of a coaxial cable with  $0.034''$  outer diameter. A strong peak in  $P_{3f}(T)$  is observed around  $T_c \sim 88.9\text{K}$  (measured by ac susceptibility) at all locations on the sample. The  $P_{3f}(T)$  peaks have similar magnitudes at both locations (GB and non-GB) although there is a slight ( $\sim 0.5\text{ K}$ ) shift of  $T_c$ . Note that all measurements are taken near the middle of the film where we have verified that current-enhancement edge effects are absent. [82]

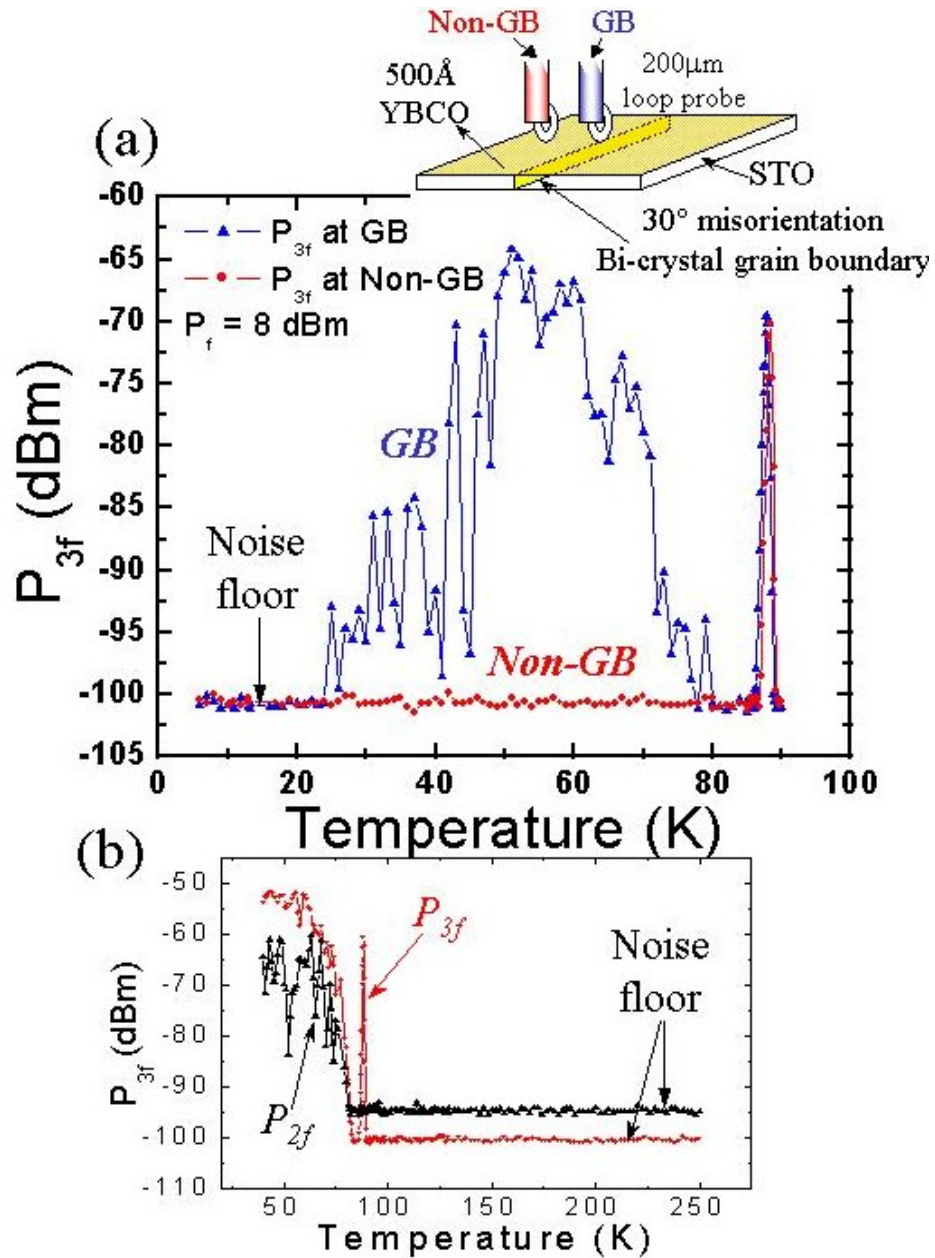


Fig. 4.1 (a)  $P_{3f}(T)$  measured above the YBCO bi-crystal grain boundary (blue, GB) and away from the gain boundary (red, Non-GB). (b)  $P_{3f}(T)$  and  $P_{2f}(T)$  measured above GB up to  $T = 250\text{K}$ . No signals above the noise level associated with the resonant modes due to the nonlinear dielectric constant of STO are observed in this temperature range.

The peak near  $T_c$  is predicted by all models of NLME in superconductors, e.g. the BCS, GL theory, and Vigni's model, and the predicted power-3 dependence (from the BCS and GL theories) of the  $P_{3f}$  on the input microwave power ( $P_f$ ) is observed. I also note that there is no observable signal seen in  $P_{2f}$  near  $T_c$  for both GB and non-GB measurements, as expected for a time-reversal symmetric superconductor.

The SrTiO<sub>3</sub> (STO) substrate is a nonlinear dielectric at low temperatures, and we have measured harmonic response from bare STO substrates below 80K [82]. The nonlinear response is confined to narrow temperature ranges at temperatures when the substrate becomes resonant due to its temperature-dependent, high dielectric constant. Therefore, if the nonlinear response is generated not only from the superconducting film, but also from the STO substrate, spiky features should be observed in  $P_{3f}(T)$  over a series of narrow temperature ranges. These features should be even clearer for  $T > T_c$ , since the screening effect in the normal state is much poorer than in the superconducting state, and more fields are allowed to penetrate into the substrate to generate  $P_{3f}$  signals.

As shown in Fig. 4.1(a), at temperatures below 80K, a strongly temperature dependent  $P_{3f}$  is observed above the YBCO bi-crystal grain boundary, while no detectable  $P_{3f}$  is seen away from the grain boundary. In addition,  $P_{2f}$  and  $P_{3f}$  above the grain boundary were measured between  $T_c$  and 250K, and no nonlinear response due to dielectric nonlinearity was observed (see Fig. 4.1(b)). Taken together, this is evidence that the observed  $P_{3f}$  is

from the grain boundary, not the nonlinearity of the STO substrate. Power dependencies of  $P_{2f}$  and  $P_{3f}$  were also performed at both GB and non-GB at 60K ( $\ll T_c$ ) and 95K ( $> T_c$ ). The measurements taken at 95K do not show  $P_{2f}$  nor  $P_{3f}$  above the noise floor until reaching very high input powers. This nonlinear response comes from the microwave circuit system, which will be discussed later in Chapter 5. It is avoided in the measurements discussed here by applying lower input microwave powers. However, as shown in Fig. 4.2, at 60K, strongly power dependent  $P_{2f}$  and  $P_{3f}$  are observed above the grain boundary, while no response is seen above the background noise level away from the bi-crystal grain boundary.

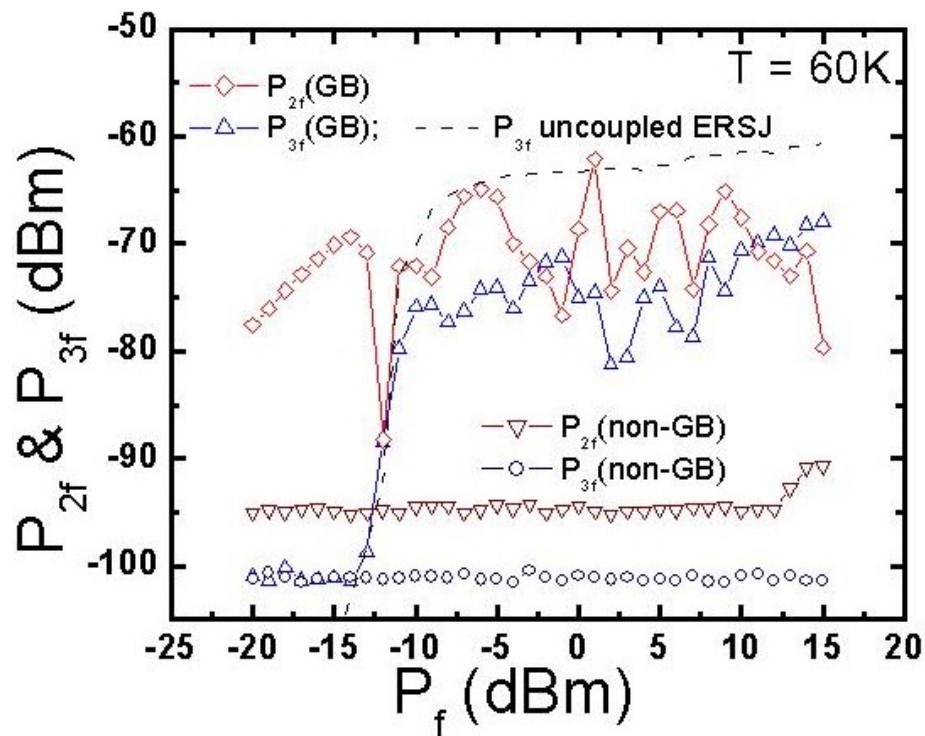


Fig. 4.2 Power dependence of  $P_{2f}$  and  $P_{3f}$  signals measured at and away from the bi-crystal grain boundary at 60K. The driving frequency = 6.5 GHz.

### 4.3 Spatially Resolved Measurement – 1D and 2D measurements

To demonstrate that the microwave microscope is able to spatially resolve a localized source of nonlinearity, a measurement of  $P_{2f}$  and  $P_{3f}$  along a line crossing the grain boundary was performed. As shown in Fig. 4.3, a clear peak in both  $P_{2f}$  and  $P_{3f}$  is observed above the GB, with a width of about  $500\mu m$ . The width of the observed  $P_{2f}/P_{3f}$  peaks are about the size of the loop probe, which determines the spatial distribution of the surface current on the sample. This interpretation is confirmed by reproducing this peak with the extended resistively shunted Josephson junction model (ERSJ) discussed below. A measurement of  $P_{2f}$  and  $P_{3f}$  along the grain boundary was also performed, and variations of both signals are observed, demonstrating its ability to resolve non-uniformity of the grain boundary.

To further address this capability, I imaged the YBCO grain boundary in two dimensions. As seen in Fig. 4.4, the bi-crystal grain boundary is identified in both  $P_{2f}$  and  $P_{3f}$  images as a region of greatly enhanced nonlinear response (orange and red colors), though the spatial resolution is limited by the current probe size.



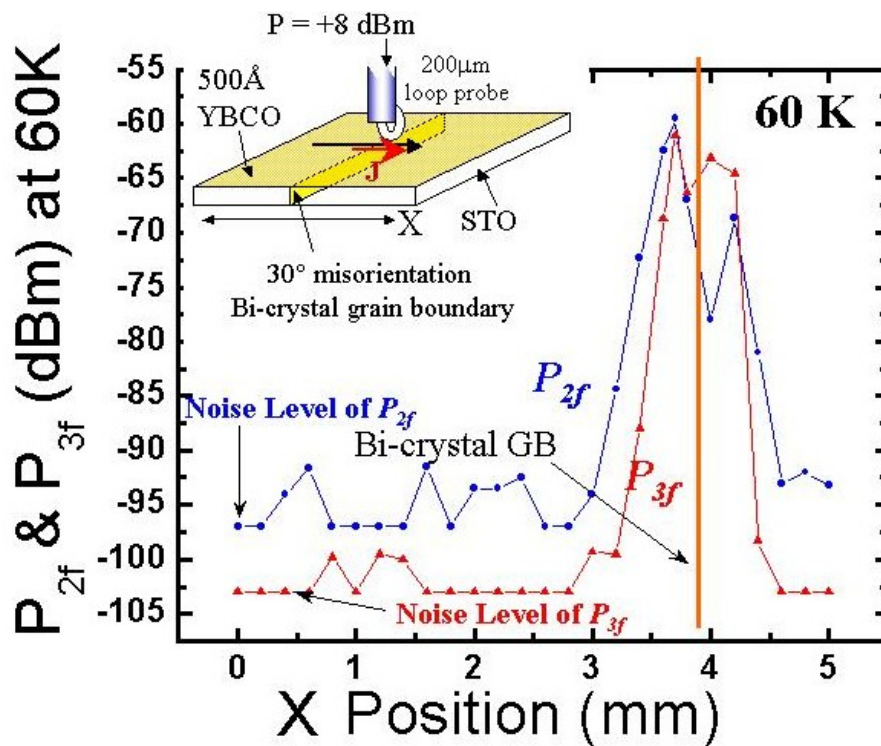


Fig. 4.3 A line-scan of  $P_{2f}(X)$  and  $P_{3f}(X)$  across the bi-crystal grain boundary taken at  $T = 60\text{K}$  with driving frequency = 6.5 GHz. Spatially resolved enhancement of  $P_{2f}$  and  $P_{3f}$  signals around the grain boundary is observed.

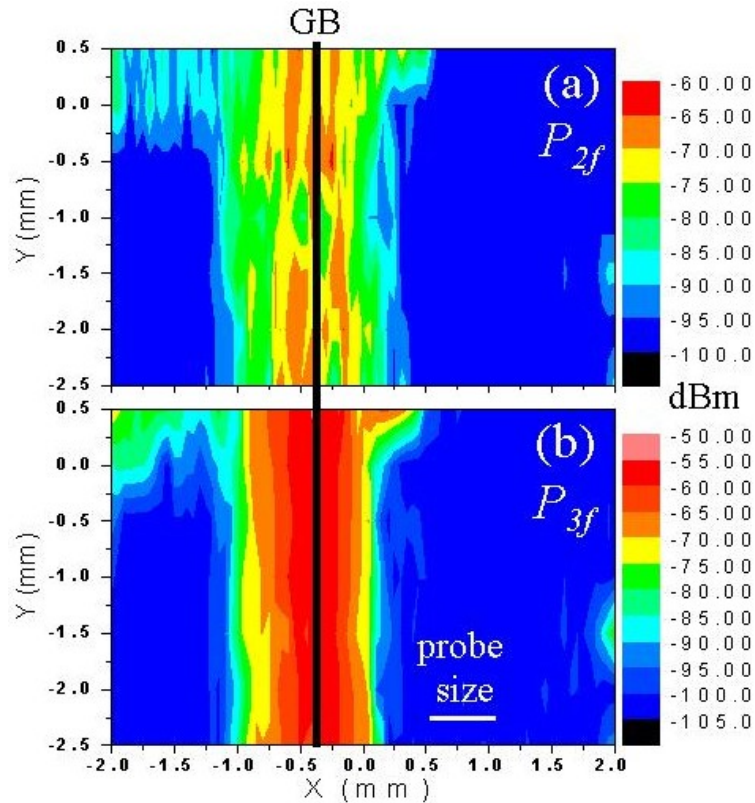


Fig. 4.4 Spatially resolved 2D images of (a)  $P_{2f}$  and (b)  $P_{3f}$  containing the YBCO bi-crystal grain boundary. The enhancement of  $P_{2f}$  and  $P_{3f}$  marks the location of the grain boundary, and the variation of  $P_{2f}$  and  $P_{3f}$  indicates the non-uniformity along the boundary. The temperature of the sample is 60K, and  $f = 6.5$  GHz. The RF currents are flowing against the grain boundary.

It is clearly shown that the harmonic responses due to the nonlinearities of the grain boundary vary along the length of the grain boundary. Since an automated translation stage is not available for my setup and the loop probe size is relatively large ( $\sim 500\mu\text{m}$ ), the spatial resolution along both x- and y-direction are limited to about  $500\mu\text{m}$ . By reducing

the probe size, we can improve the spatial resolution to the scale of  $10\ \mu\text{m}$ , as discussed in Chapter 7.

#### 4.4 Modeling the Origins of Second and Third Harmonic Generation in the Bi-crystal Grain Boundary

It is well known that applying a single-tone microwave current to a single resistively shunted Josephson junction generates harmonics at all odd integer multiples of the drive frequency [44]. To obtain a more comprehensive understanding of weak link junctions, the Extended Resistively Shunted Josephson array (ERSJ) model was introduced to model long Josephson junctions, such as the YBCO bi-crystal grain boundary [45,83]. In this section, I present ERSJ models to simulate a YBCO bi-crystal grain boundary as either an array of identical inductively coupled, or independent (uncoupled), Josephson junctions acting in parallel.

In prior work with these bi-crystal junctions for SQUID microscopy in Prof. Wellstood's group, the characteristics of the YBCO thin films deposited on a  $30^\circ$  mis-oriented STO substrate with our pulse-laser-deposition (PLD) facility were well studied. For a lithographically-defined  $3\ \mu\text{m}$  wide Josephson junction made of a  $1500\ \text{\AA}$  thick YBCO film over a  $30^\circ$  mis-oriented bi-crystal grain boundary, the critical current and shunt resistance of this junction are measured to be about  $50\ \mu\text{A}$  and  $4\text{-}8\ \Omega$  at  $77\text{K}$ , respectively [84]. The

critical current density of this junction can be estimated accordingly,

$$J_c(77K) \cong \frac{50\mu A}{3\mu m \times 150nm} \cong 1.1 \times 10^8 A/m^2.$$

The Josephson penetration depth  $\lambda_J$  is defined by

$$\lambda_J(T) = \sqrt{\frac{\Phi_0}{2\pi\mu_0 J_c(T) d_m(T)}},$$

where  $\Phi_0$  is the flux quantum  $h/2e$ ,  $J_c$  is the critical current density of the junction,  $d_m$  is the magnetic thickness of the junction defined as  $d_m = d + 2\lambda \coth(t/\lambda) \cong 2\lambda \coth(t/\lambda)$ , [85]  $t$

is the film thickness (which is  $500\text{\AA}$  in my case), and  $d$  is the thickness of the bi-crystal junction, which is not more than a few nano-meters. Using the Kulik-Omelyanchuk theory [86] to estimate the temperature dependence of the critical current density, we found that

$J_c(60K) \cong 2.3J_c(77K) \cong 2.53 \times 10^8 A/m^2$ . With the additional assumption that

$\lambda(T=0) = 1800\text{\AA}$  and  $\lambda(T)$  has a GL-like temperature dependence,

$\lambda(T) \cong \lambda(T=0) / \sqrt{1 - (T/T_c)^2}$  ( $T_c \sim 89.5K$ ), the Josephson penetration depth  $\lambda_J$  is

estimated to be around  $0.67\mu m$  at 60K. On the other hand, assuming that the critical current and shunt resistance are simply proportional and inversely proportional to the cross sectional area of the junction, respectively, the critical current and shunt resistance of each junction (with size  $\lambda_J$ ) in the ERSJ model are  $\sim 8\mu A$  and  $\sim 70\Omega$  at 60K, respectively.

The currents applied to each junction in the ERSJ model vary according to the surface current distribution on the film induced by the loop probe. The nonlinear potential differences across all junctions are calculated via different means, which will be discussed later. The expected higher order harmonics are obtained via summation of all potential differences and Fourier transforming this collective nonlinear potential difference at twice and triple the fundamental frequency. The spatial distribution of the surface current density is calculated from a simplified analytical model (discussed in detail in the previous chapter) of an ideal circular loop in a vertical plane, with radius  $270\mu m$ , coupling to a perfectly conducting horizontal plane  $382.5\mu m$  away from the center of the loop. The magnitude of the current density is determined by a much more sophisticated microwave simulation using the Ansoft<sup>TM</sup> High Frequency Structure Simulator (HFSS) software, which also produces a similar surface current distribution.

#### 4.4.1 Uncoupled ERSJ Model Solved by Mathematica

My uncoupled ERSJ model of the grain boundary consists of 1001 equally spaced independent Josephson junctions, with spacing determined by the Josephson penetration depth  $\lambda_J \sim 0.65\mu m$ , as shown in Fig. 4.5.

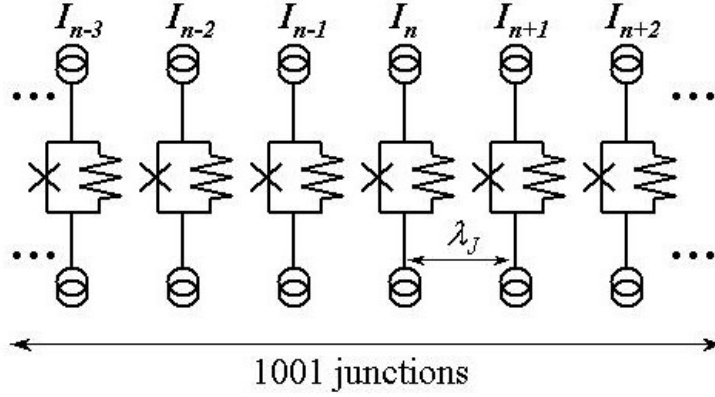


Fig. 4.5 Schematic of the un-coupled ERSJ model. The applied current distribution functional form is represented by the discrete current sources  $I_n$ .

The calculation of  $P_{3f}$  in the uncoupled ERSJ model is performed by Mathematica<sup>TM</sup> by simulating the nonlinear potential difference of each junction governed by the equation

$$I_n \sin(\omega t) = I_c \sin \Delta \gamma_n(t) + \frac{\Phi_0}{2\pi R} \frac{d\Delta \gamma_n(t)}{dt} + \frac{\Phi_0 C}{2\pi} \frac{d^2 \Delta \gamma_n(t)}{dt^2},$$

where  $\Phi_0$  is the flux quantum  $h/2e$ ,  $I_0 \sin(\omega t)$  is the driving AC current which varies in magnitude with junction position,  $I_c$  is the critical current of the junction,  $R$  and  $C$  are the shunted resistance and capacitance of the junction, and  $\Delta \gamma_n(t)$  is the time-dependent gauge invariant phase difference across the  $n$ -th junction. In the range that the driving frequency is small compared to the plasma frequency of the junction,  $\omega \ll \omega_p = \sqrt{2\pi I_0 / \Phi_0 C}$ , the contribution from the shunted capacitance can be ignored, and the equation becomes

$$I_n \sin(\omega t) \cong I_c \sin \Delta \gamma_n(t) + \frac{\Phi_0}{2\pi R} \frac{d\Delta \gamma_n(t)}{dt}.$$

The nonlinear potential differences are obtained by solving this equation for each junction with various driving currents determined by the current distribution mentioned before, and the derivative of  $\Delta\gamma(t)$  gives the potential difference

$$V(t) = \frac{\Phi_0}{2\pi} \frac{d\Delta\gamma(t)}{dt}.$$

By summing up the nonlinear potential differences of all junctions, the second and third harmonic contents are extracted via Fourier transformation at twice and triple the fundamental frequency  $\omega$ . It is found that this model only produces third harmonic generation, which is shown as the dashed line centered around 4 mm in Fig. 4.6, and no second harmonic signal is generated. The spatial dependence in fig. 4.6 is produced by taking different slices through the  $I(x,y)$  current distribution produced by the loop probe, and using them to drive the coupled and un-coupled ERSJ array. The current distribution is calculated by the ideal-loop analytical model.

The absence of  $P_{2f}$  is due to the absence of Josephson vortices in this model. Additionally, this model predicts a narrow spatial distribution of  $P_{3f}$  of greater magnitude (almost 20dB) than is observed experimentally. A power dependence calculation from this uncoupled ERSJ model is also performed and compared with experimental results (dashed line in Fig. 4.2). The comparison shows qualitative agreement with the  $P_{3f}(P_f)$  data taken over the GB. The saturating behavior of  $P_{3f}(P_f)$  in Fig. 4.2 is characteristic of a driven Josephson junction GB.

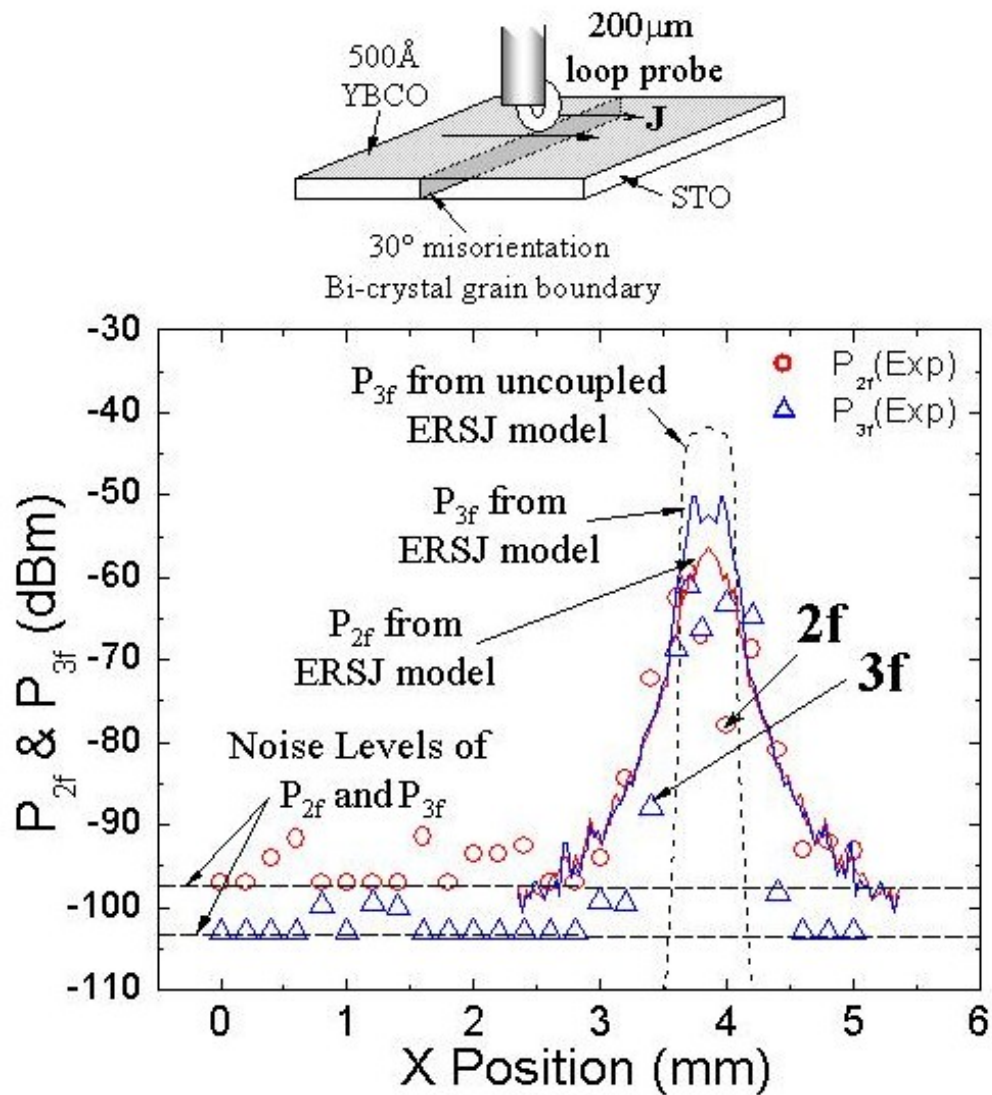


Fig. 4.6 Coupled (solid blue and red lines) and uncoupled (dashed line) ERSJ model calculations compared with the experimental  $P_{2f}$  (red circle) and  $P_{3f}$  (blue triangle) data shown in Fig. 4.3. At top is the schematic of the experiment.

#### 4.4.2 Coupled ERSJ Model by WRSpice®



On the other hand, the calculation with the inductively coupled ERSJ model, which includes Josephson vortices, performed by WRSpice, gives a very good description in both magnitude and spatial resolution of the experimental results for both  $P_{2f}$  and  $P_{3f}$  (the results are shown as solid lines in Fig. 4.6).

The only difference between the uncoupled and coupled ERSJ models is the lateral inductances, which simulate the magnetic coupling between junctions (see Fig. 4.7). The coupling inductances are determined by an algorithm established in Oates' group by considering a single static vortex in an infinite junction. According to this algorithm, the lateral inductance per unit length along both sides of the junction is [45, 85]

$$l_{unit\ length} = \frac{\mu_0 d_m}{2t},$$

where  $d_m = d + 2\lambda \coth(t/\lambda)$  is the magnetic thickness of the junction,  $t$  is the film thickness,  $\lambda$  is the magnetic penetration depth, and  $d$  is the junction thickness, which is a few nano-meters. In my case, this lateral coupling inductance  $l_{cell}$  is about  $2 \times 10^{-11} H$  for each unit cell, which has a size of  $\lambda_j$ .

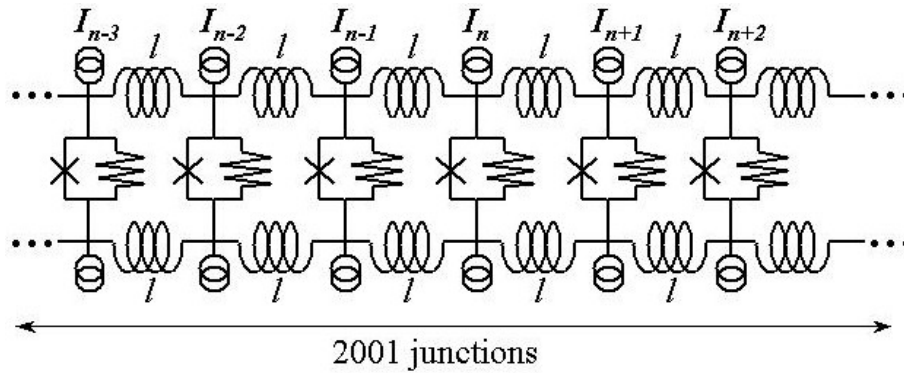


Fig. 4.7 Schematic of the coupled ERSJ model simulated by WRSpice<sup>®</sup>. The X represents a Josephson junction.

With the characteristic parameters of the junction mentioned previously, together with the lateral coupling inductance, I make a circuit consisting of 2001 unit cells as shown in Fig. 4.7, as an estimation of the real Extended Resistively Shunted Josephson junction. This circuit is simulated via software developed by Whitely Research Inc., called WRSpice<sup>®</sup>, which was developed to calculate the electrical response of superconducting Josephson circuits. A detailed description of how to simulate the circuit using this software can be found in Appendix B.

Most parameters used in WRSpice<sup>®</sup> are associated with the sample properties, and are pretty well determined, except for the input currents. Since the input currents are determined by the probe/sample coupling which is not exactly known, I assumed the total input current is roughly estimated as 88 mA, based on the HFSS calculation discussed in Chapter 3.

The results of this model are shown as solid lines in Fig. 4.6. We see that the model correctly reproduces the spatial distribution of  $P_{2f}$  and  $P_{3f}$ , and does a good job of reproducing the magnitude of  $P_{2f}$ . The magnitude of  $P_{3f}$  is overestimated by about 10 dB over the center of the GB.

#### 4.5 Vortex Dynamics Discussion with WRSpice<sup>®</sup> Simulations

To further our understanding of the physics governing the local nonlinearities, especially the  $P_{2f}$  response, we use the ERSJ model calculated by WRSpice<sup>™</sup> to evaluate the nucleation and motion of Josephson vortices in the middle of an infinite junction.

A long Josephson junction can be described by the sin-Gordon equation,[45]

$$\lambda_J^2 \frac{\partial^2 \Delta\gamma(x,t)}{\partial x^2} = \sin \Delta\gamma(x,t) + \frac{L_J}{R_J} \frac{\partial \Delta\gamma(x,t)}{\partial t} + C_J L_J \frac{\partial^2 \Delta\gamma(x,t)}{\partial t^2},$$

where  $\Delta\gamma$  is the gauge-invariant phase difference across the junction,  $\lambda_J$  is the Josephson penetration depth,  $L_J \equiv \Phi_0/2\pi J_c$ ,  $R_J \equiv \rho d$ ,  $\rho$  and  $d$  are the junction resistivity and thickness, and  $C_J \equiv \varepsilon/d$ . The WRSpice<sup>®</sup> model is equivalent to solving this equation on a grid. We calculate the key quantity  $\Delta\gamma(n,t)$ , where  $n$  indicates the  $n$ -th discrete junction, to extract other physical quantities, such as the magnetic field and flux at each junction.

The magnetic field along the grain boundary is given by

$$B(x) = \frac{\Phi_0}{2\pi d_m} \frac{\partial \Delta\gamma(x,t)}{\partial x},$$

where  $\Phi_0$  is the flux quantum, and  $d_m = d + 2\lambda \coth(t/\lambda) \cong 2\lambda \coth(t/\lambda)$  is the magnetic

thickness of the junction. Since the distance between the junctions is  $\lambda_J$  in the model, the flux between adjacent junctions is determined by

$$\Phi(n) = B(n) \times (d_m \cdot \lambda_J) = \frac{\Phi_0 \lambda_J}{2\pi} \left. \frac{\partial \Delta \gamma(x, t)}{\partial x} \right|_{x=n \times \lambda_J}.$$

It is pointed out that the locations where the gauge-invariant phase difference are odd multiples of  $\pi$  are the cores of vortices with a full flux quantum. On the other hand, we think that calculations of the magnetic flux as a function of position and time also directly represent the motion of vortices along the grain boundary.

#### 4.5.1 Oates' ERSJ calculation

To validate our approach, I tried to reproduce the vortex dynamics of the superconducting (YBCO) strip line resonator of Oates, *et al.* with a bi-crystal grain boundary crossing the middle of the resonator (see the inset of Fig. 4.8). This setup allows vortices to enter the YBCO thin film from the edges.

Oates *et al.* calculated the vortex motion along the bi-crystal grain boundary as a function of time (see Fig. 4.8). They found that more vortices enter the sample from the edge as they increased the input power, and also that the vortices go deeper toward the center of the strip line during an RF period.

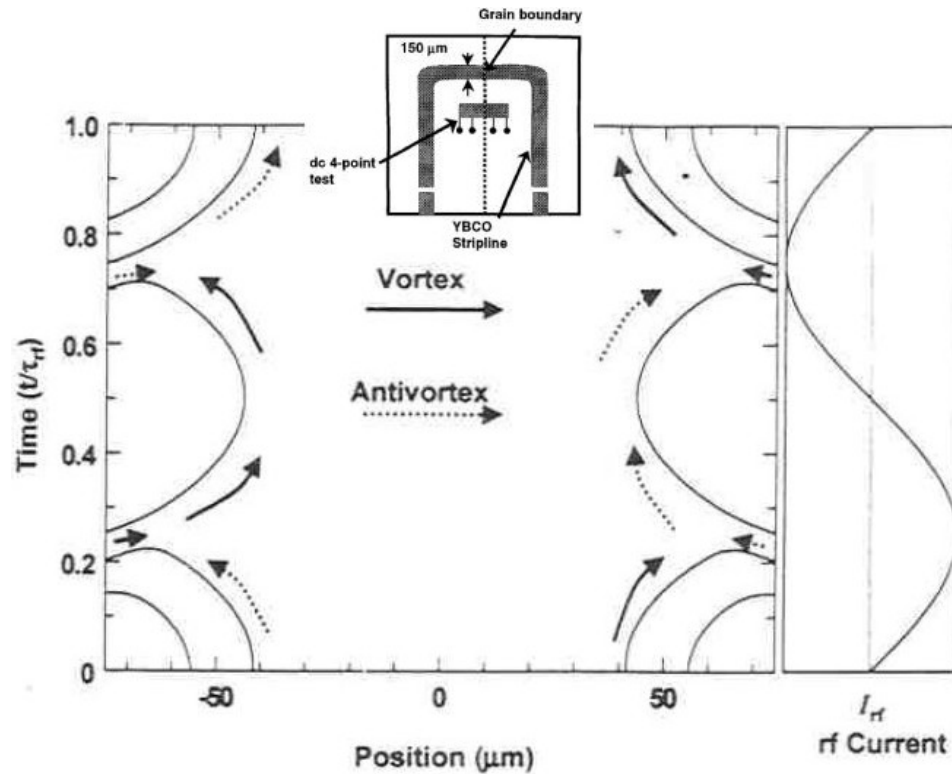


Fig. 4.8 Trajectories of vortices simulated by Oates' group for their superconducting strip line resonator as shown in the inset. The strip has a width of  $150 \mu\text{m}$ . This figure is taken from Ref. [45].

Taking the parameters ( $l = 0.5 \text{ pH}$ ,  $R = 8 \Omega$ ,  $I_c = 40 \mu\text{A}$ ) estimated for Oates' setup [45], I reconstructed and simulated Oates' ERSJ model with WRSpice<sup>®</sup> at different total input currents (1 – 8 mA). Qualitatively, I was able to reproduce the motion of vortices that Oates found. One of the ways to locate the vortex cores is to find the locations where the gauge-invariant phase differences  $\Delta\gamma$  are odd multiples of  $\pi$ . Therefore, by calculating  $\Delta\gamma$  as a function of time for each junction, I can locate the vortex core at any moment. Shown in Fig. 4.9 are trajectories of vortex cores for various total input currents (2 – 8 mA). It is clear

that not only are the trajectories moving towards the center of the strip line resonator as larger currents are applied, but also more and more vortices are generated (one vortex for 2 mA; four vortices for 8 mA) in each RF cycle.

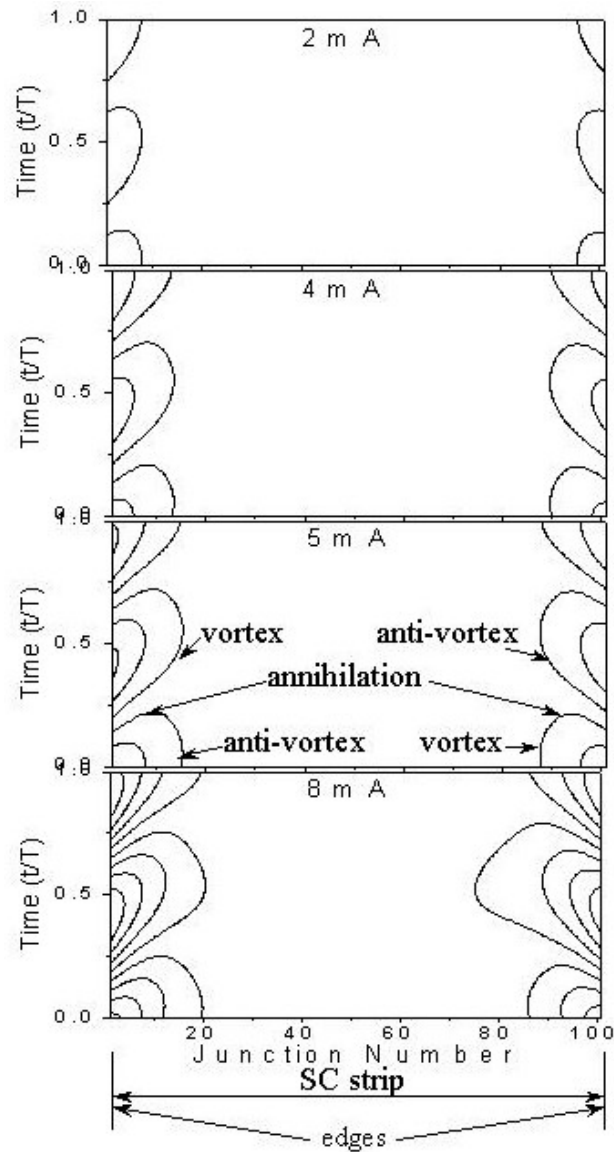


Fig. 4.9 Trajectories of vortices in one RF cycle simulated for different total input currents in Oates' strip line resonator.

#### 4.5.2 Vortex Dynamics in Our YBCO Bi-crystal Grain Boundary

I next used WRSpice<sup>®</sup> to simulate my own setup. In my case, there are no edges that can act as easy nucleation sites for the vortices.

The parameters used in WRSpice<sup>®</sup> are the same as previously stated for the GB junction driven by the loop probe. The lateral coupling inductance in each unit cell is  $2 \times 10^{-11}$  H, the shunt resistance is  $70 \Omega$ , and the critical current of each Josephson junction is  $8 \mu\text{A}$ . The vortex trajectories shown in Fig. 4.10 are simulated with a total current of  $\sim 88$  mA. Also shown is the flux profile along the long junction, in the middle of an RF cycle ( $t = 0.5T$ ). The driving current distribution is peaked at the center of the long junction (junction number = 1001).

From Fig. 4.10, we observe that vortex-anti-vortex (VAV) pairs are generated near the center of the junction, and are then pushed apart pair by pair in the first half of the RF cycle. In the second half of the RF cycle, when the currents reverse direction, the VAV pairs are drawn back and annihilate near the center of the junction. The slope of the trajectories in Fig. 4.10 represents the speed of a vortex. If the trajectory is vertical in the plot, the vortex is stationary. If the trajectory is nearly horizontal, the vortex is moving very fast. It is noted that the simulation does not demonstrate continuous motion of vortices. When the VAV pairs are expelled from or drawn to the center of the junction, they jump

between discrete locations marked by the spikes in the flux profile. The locations of the vortex spikes are fixed throughout the RF cycle.

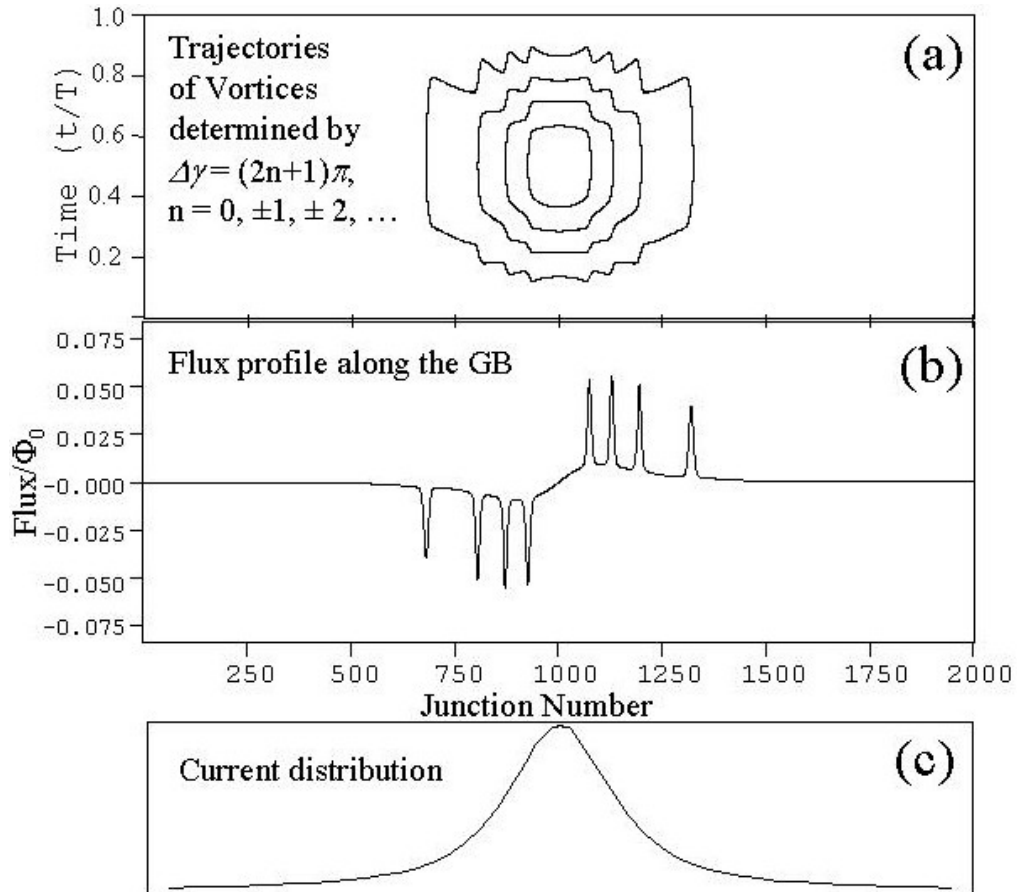


Fig. 4.10 WRSpice<sup>®</sup> simulation for vortex dynamics in a YBCO bi-crystal grain boundary. (a) trajectories of vortex cores, (b) flux profile along the grain boundary at  $t = 0.5T$ . (c) current distribution.

The first three vortices created in the RF cycle show a very complicated history of VAV creation and annihilation. We attribute this complication to the fact that many junctions experience currents near their critical currents nearly simultaneously. In the stripline model,



only a few junctions at the edges are reaching their critical current at a given instant in the RF period.

#### 4.6 Extraction of $J_{NL}$ from the Data

Different microscopic models of nonlinearity predict different values and temperature dependences of the nonlinear scaling current density  $J_{NL}(T)$ . For example, in the nonlinear Meissner effect and Ginzburg-Landau theory,  $J_{NL} \sim 10^8 \text{ A/cm}^2$  or higher, except for temperatures close to  $T_c$ , while the  $J_{NL}$  of a long 1-D Josephson junction array is expected to be about  $10^5 \sim 10^6 \text{ A/cm}^2$  or less [68]. To further evaluate the capability of our microscope to detect intrinsic superconducting nonlinearities due to different mechanisms, I extract a geometry-free scaling current density,  $J_{NL}$ , from our data. Following the algorithm and assumptions described in Chapter 3 and assuming  $\lambda_L(T=0, J=0) = 1500 \text{ \AA}$ , the  $J_{NL}$  of a line-scan across the YBCO bi-crystal grain boundary is extracted from the  $P_{3f}$  data in Fig. 4.3, and shown in Fig. 4.11.

I obtain the dominant  $J_{NL}$  near the grain boundary at 60 K to be  $J_{NL}^{GB} \sim 1.5 \times 10^5 \text{ A/cm}^2$ , which is comparable to Willemsen's result [68], while the sensitivity of our microscope to this sample is currently limited to  $J_{NL} \leq 1.4 \times 10^6 \text{ A/cm}^2$ . However, the model calculation suggests that thinner films and stronger coupling between the film and the loop probe will give stronger nonlinear response from a given mechanism, and improve the sensitivity to the nonlinearities associated with larger values of  $J_{NL}$ .

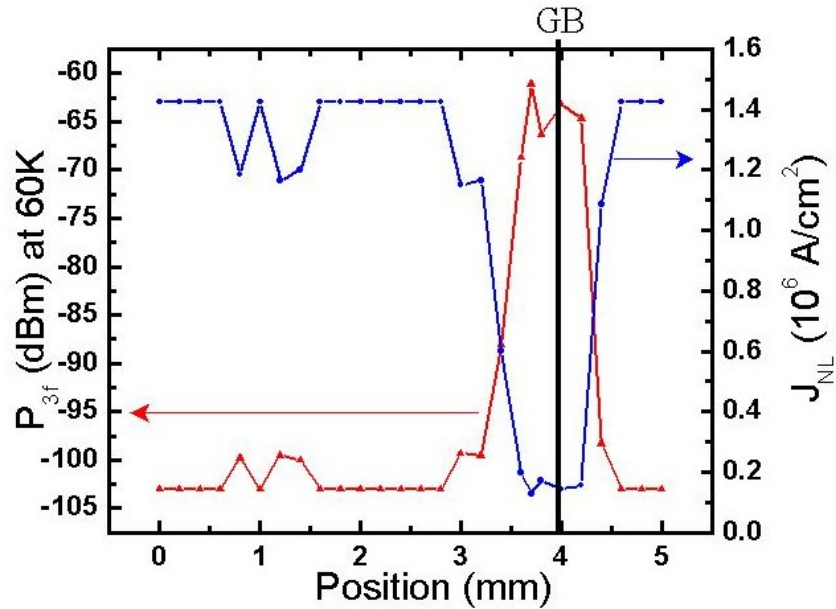


Fig. 4.11 The  $P_{3f}(X)$  (red) experimental data in Fig. 4.3 is shown together with the extracted nonlinear current density scale  $J_{NL}(X)$  (blue). The sample is a YBCO bi-crystal grain boundary junction, measured at 60K with driving frequency = 6.5 GHz.

#### 4.7 Conclusion

I demonstrated the ability of our nonlinear near-field microwave microscope to locally identify the YBCO bi-crystal grain boundary via harmonic measurements. The scaling current density for the grain boundary is extracted and is comparable to what is expected.

The spatially resolved harmonic measurements are interpreted with the ERSJ model simulated by WRSpice<sup>®</sup> software. Both the magnitude and width of the harmonic signals are well reproduced. We also use WRSpice<sup>®</sup> to simulate the vortex dynamics in the grain boundary. The vortex-anti-vortex (VAV) pairs are generated beneath the loop probe (the

center of the current distribution). The VAV pairs are expelled from and drawn to the center in the first and second half of RF cycle respectively. However, the vortices do not move continuously but jump among discrete locations.

## CHAPTER 5

### DOPING DEPENDENT NONLINEARITIES IN HTSC

#### – SYSTEM AND SAMPLE CHARACTERIZATION

As addressed in previous chapters, nonlinearities in high- $T_c$  superconductors (HTSC) have been of increasing interest. In particular, deeper understanding of high- $T_c$  superconductivity may be gained by understanding the distinct nonlinear phenomena present in HTSC. In this chapter I demonstrate how I can use the near-field microwave microscope as an independent means to measure and identify doping-dependent nonlinearities in HTSC.

Many important phenomena in HTSC are found to be doping-dependent. For example, the recently proposed micro-current model by Varma [64] in under-doped HTSC is expected to be a doping-dependent effect. This is expected because of the onset of this micro-current is expected to occur at the pseudo-gap temperature,  $T^*$ , which varies considerably with doping (from greater than 300K to 100K) in under-doped YBCO. C. Nayak has proposed a different micro-current model for the pseudogap phase in HTSC [87]. This phase will break time-reversal symmetry and also be doping-dependent. Another doping dependent nonlinearity observed is in the Andreev Bound States (ABS) proposed by Deutscher *et al.* [56]. They claimed that this time-reversal symmetry-breaking

(TRSB) mechanism in ABS is only seen in over-doped YBCO, but absent in under-doped ones.

In addition to the doping-dependent TRSB mechanisms, recent work by Tallon *et al.* [88, 89] claim that the zero-temperature condensation energy,  $U_0$ , in under-doped HTSC is doping dependent. From Tallon's work, we can conclude that the nonlinear Meissner effect (NLME) should also be doping dependent. This is because the de-pairing critical current density, which sets the scale for the NLME, scales with  $\sqrt{U_0}$ .

## 5.1 Experimental Setup and Sample Description

### 5.1.1 Brief review of the microscope

As described in Chapter 1, our microscope consists of a HP83620B microwave synthesizer, a set of microwave amplifiers from MITEQ, low- and high-pass filters, a probe, and an Agilent E4407B spectrum analyzer. The synthesizer generates a single tone microwave signal at the desired frequency  $f$  (~6.5 GHz), along with additional weak harmonics.

To guarantee high spectral purity in the input signal to the sample, we use low-pass filters to purify the signal going into the sample. To apply this signal to the sample, we use a magnetic loop probe. The probe is made of a semi-rigid coaxial cable with its inner conductor forming a semi-circular loop in contact with the other conductor, to couple the signal to the sample (see Fig. 1.4(a)). By doing so, a microwave current distribution determined by the loop geometry is locally induced on the sample surface. If any local

nonlinear mechanisms are present in the sample, the resulting currents on the sample will contain higher order harmonics (TRS:  $3f$ ,  $5f$ ,  $7f$ ,...; TRSB:  $2f$ ,  $4f$ ,  $6f$ ,...). These signals (the strongest are at  $2f$  and  $3f$ ) couple back to the microwave circuit through the loop probe, and are selected by the high-pass filters (at  $2f$  and  $3f$ ), amplified by the amplifiers by  $\sim 65dB$ , and are finally measured by the spectrum analyzer. The loop probe I used is made of a completely nonmagnetic semi-rigid coaxial cable with 0.037" outer diameter (OD), so that undesired magnetic perturbation from the probe itself is avoided.

### 5.1.2 Samples

Our samples are [001] oriented  $YBa_2Cu_3O_{7-\delta}$  (YBCO) thin films originally prepared by Matt Sullivan in the Center using the pulsed laser deposition (PLD) technique on  $NdGaO_3$  (NGO) and  $SrTiO_3$  (STO) at the optimal-doping level ( $\delta \sim 0.05$ ). After the deposition, some of the samples were treated by Benjamin Palmer to vary the oxygen deficiency using an annealing process he developed in the Laboratory for Physical Science (LPS) [90]. The change in oxygen content has the effect of varying the hole concentration of the films. The AC susceptibility of each film was measured after the re-annealing procedure. We find that some broadening of the transition for lower doping levels was observed.

Figure 5.1 shows the AC susceptibility measurements (imaginary part) of samples MCS1, MCS4, and MCS48, which have different doping levels. The broadening of these peaks marks the broadening of the transition and is quantified by  $\Delta T$ , defined as the full-

width-half-magnitude of the peaks. This broadening can be a result of the residual  $\sigma_2$  in under-doped (UD) HTSC at  $T > T_c$  [91,92], and/or the inhomogeneous oxygen content over the sample due to the re-annealing treatment. Listed in Table 5.1 is a summary of the physical properties of films I've measured as well as their estimated doping levels.

Table 5.1 Parameters of oxygen-doped YBCO thin films. The  $T_c$ 's and  $\Delta T$ 's are determined by AC susceptibility measurements ( $\text{Im}(\chi)$ ). I measured the  $T_c$ 's twice on MCS2, MCS48, and MCS50. The results are separated by “;”. On MCS2, a double peak pattern is observed in  $\text{Im}(\chi)$  in the second measurement, and the corresponding  $T_c$  of each peak is separated by “/”.

Sample	Maker	Substrate	Thickness	$T_c$ (K)	$\Delta T$ (K)	Hole Doping
MCS48	Sullivan	NGO	96 nm	47.86; 45.8	~3	0.082
MCS50	Sullivan	NGO	96 nm	75.7; 74.2	~ 1.3	0.116
MCS1	Sullivan	STO	132 nm	63.1	~1.3	
MCS2	Sullivan	STO	185 nm	81.56; 83.96/82.08	~ 1.3	0.13
MCS3	Sullivan	STO	130 nm	90.5	~ 0.7	0.16
MCS4	Sullivan	STO	95 nm	54.15	~ 1.7	0.088

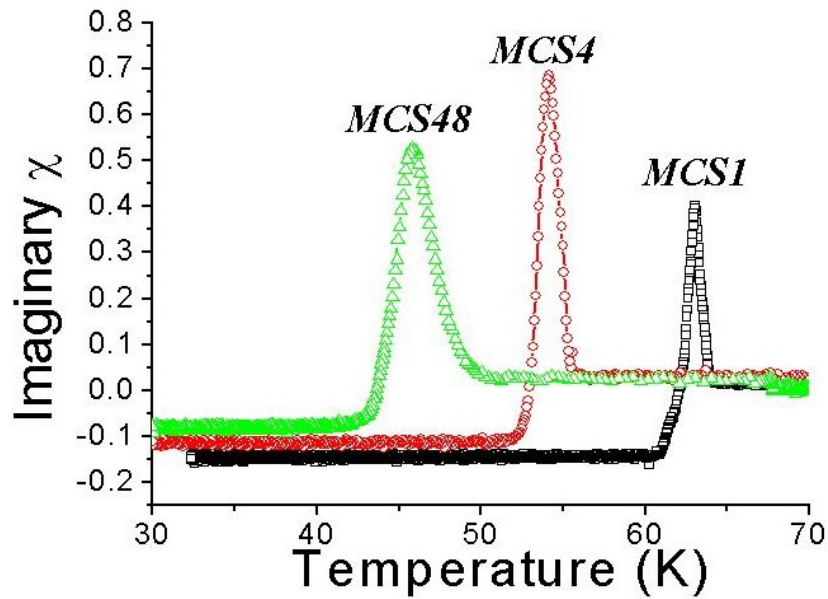


Fig. 5.1 Imaginary part of the AC susceptibility measured for YBCO thin film samples MCS48, MCS4, and MCS1, which have different doping levels. Broadening of the transition is observed as the doping level decreased.

### 5.1.3 Field dependent $P_{2f}$ and Importance of the Magnetic Shielding Assembly

One of the hallmarks of superconductivity is perfect diamagnetism (the Meissner effect). A superconductor immersed in a static magnetic field spontaneously excludes all magnetic fields when it is cooled below  $T_c$ . This phenomenon is sustained by the screening currents flowing in the superconductor, and is therefore limited by the geometry of the superconductor and the magnitude of the fields to be excluded. For a Type II superconductor, when the Meissner screening currents can no longer sustain the perfect diamagnetism because the external magnetic field is too large, the superconductor enters into the mixed state, allowing vortices to penetrate. For a thin film [93] with a magnetic



field normal to the surface, demagnetization factors are important. In particular, the larger the surface area is, the smaller the magnetic field required to induce vortices in the sample.

An estimate of the first vortex entry field,  $B_v$ , is given by

$$B_v \cong \frac{\Phi_0}{A},$$

where  $\Phi_0 = 2.07 \times 10^{-15} \text{ Tm}^2$  is the flux quantum, and  $A$  is the surface area perpendicular to the field.

Given that most of my samples are  $10 \times 10 \text{ mm}^2$  YBCO films, the magnetic field required to induce vortices in the film in the worst-case scenario is  $\sim 0.2 \mu\text{G}$ . This is much smaller than the earth's residual magnetic field (on the order of  $\sim 0.5 \text{ G}$ ). Since the nonlinearities we are looking for include TRSB mechanisms, which usually involve local spontaneous currents or magnetizations, we must be aware of, and do our best to eliminate, the externally induced vortices in the samples.

My early harmonic data on films at various doping levels were taken in the presence of the residual magnetic field of the earth, along with all other possible electromagnetic (EM) disturbances from the equipment in the laboratory. Though the third harmonic measurements are very reproducible, the second harmonic data, which addresses the presence of TRSB mechanisms, are not. As shown in Fig. 5.2, four zero-field-cooled temperature ramps from  $T < T_c$  to  $T > T_c$  were performed under these conditions. Fig. 5.2(a) and (b) were measured on different days. The  $P_{2f}(T)$  data does not show good

reproducibility whether we compare data taken on one day or between different days, while the  $P_{3f}(T)$  data is much more reproducible. Note also that the background  $P_{2f}$  level increased substantially on the second day (Fig. 5.2(b)) and interfered destructively with the signal generated by the sample.

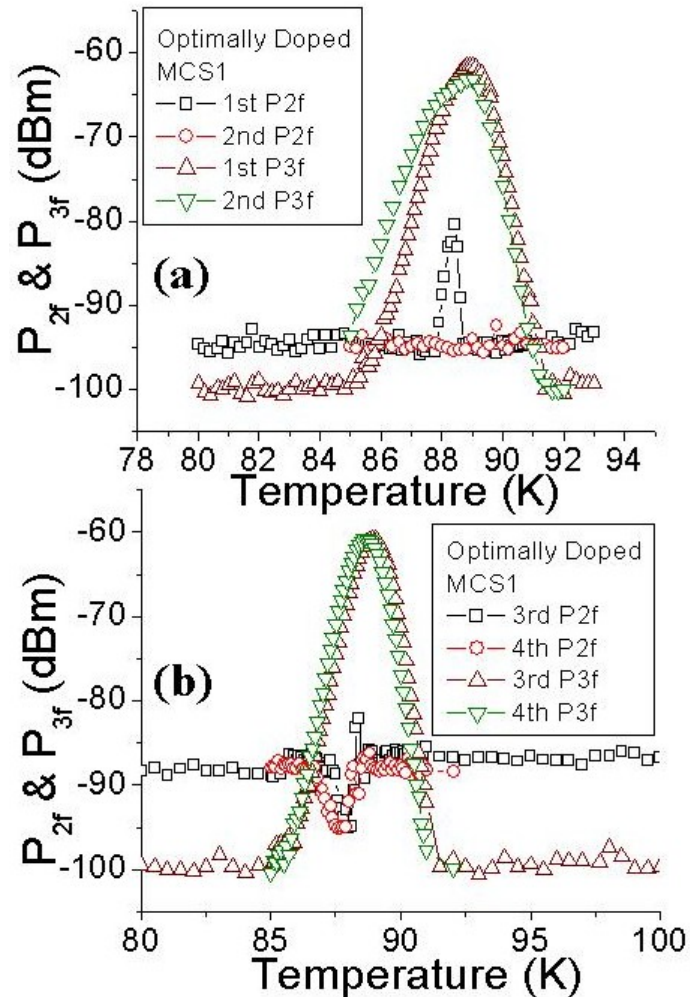


Fig. 5.2 Temperature dependent harmonic measurements of an optimally doped YBCO thin film (MCS1) taken on different days at slightly driving different frequencies (differing by less than 5 MHz). The measurements are performed in an unshielded environment.

In addition, second harmonic data were taken under applied DC magnetic fields, along with the earth's field and all other EM disturbances. The applied DC field is in the direction perpendicular to the film. Strong field dependence is observed in the second harmonic data (Fig. 5.3), which indicates that vortices are involved in the measurement. The inset in Fig. 5.3 shows  $P_2(H)$  measured at  $T = 51\text{K}$ . Different maximum value field-ramps are performed, and hysteretic behavior is observed in both cases, indicating that flux has penetrated to the sample. It is worth noting that no second harmonic generation is observed above  $T_c$  at all DC fields, which means that there is no DC field-dependent background present in our harmonic measurements. Also note that the third harmonic data is rather insensitive to the magnetic field, at least in the vicinity of  $T_c$ .

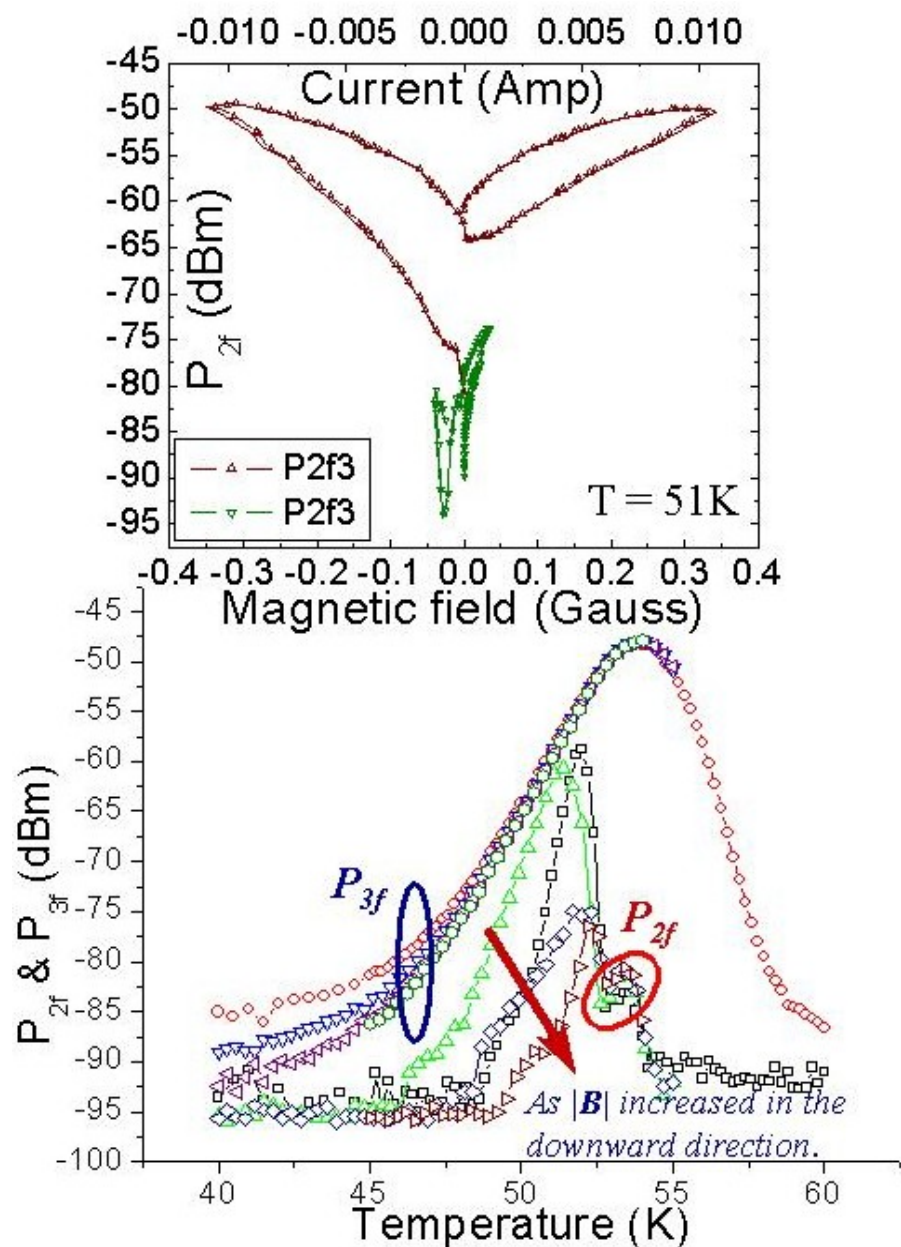


Fig. 5.3 The bottom data demonstrates that  $P_{2f}$  is affected by the applied magnetic field. The sample (MCS4) was cooled through  $T_c$  with various DC magnetic fields (pointing downward) and the temperature dependent harmonic measurements were taken during warming. The top data is a field-dependent measurement on the same sample performed after the sample was cooled through  $T_c$  to  $\sim 51\text{K}$  in the Earth's field.

To eliminate (or at least reduce) the effect of vortices on our harmonic measurements, I designed a multi-layered magnetic shielding assembly, shown in Fig. 5.4. In fact, this was designed and built in collaboration with Amuneal (Philadelphia, PA). This assembly consists of four layers of high permeability metals, which have different magnetic characteristics in different temperature ranges. Two of the layers are made of Amumetal, which have extremely high permeability at higher temperatures ( $\mu_r \sim 90000$ ), including room temperature, but gradually decrease at lower temperature. Another two layers are made of Cryoperm 10<sup>®</sup> metal, and have extremely high permeability at lower temperatures ( $\mu_r \sim 80000$ ), but decreases at higher temperatures. Using both metals in our multi-layered shielding assembly allows us to have a very efficient shielding assembly over a wide temperature range. Finally, the bottom plate of this assembly is made of ultra-low-carbon steel, which has a very high saturation fields, about 22000 Gauss at room temperature. This is not crucial in our experiment because what we want to shield out is merely the earth's residual field. But it will be helpful if one needed to shield out much stronger magnetic fields.

Although my field dependent measurements of the second harmonic data was not performed after the installation of this assembly, we found that the shielded “zero-field” second harmonic data are much more reproducible, which indicates a very minimal contribution from magnetic vortices. Figure 5.5 shows that the  $P_{2f}(T)$  data taken in the shielded environment are much more reproducible.

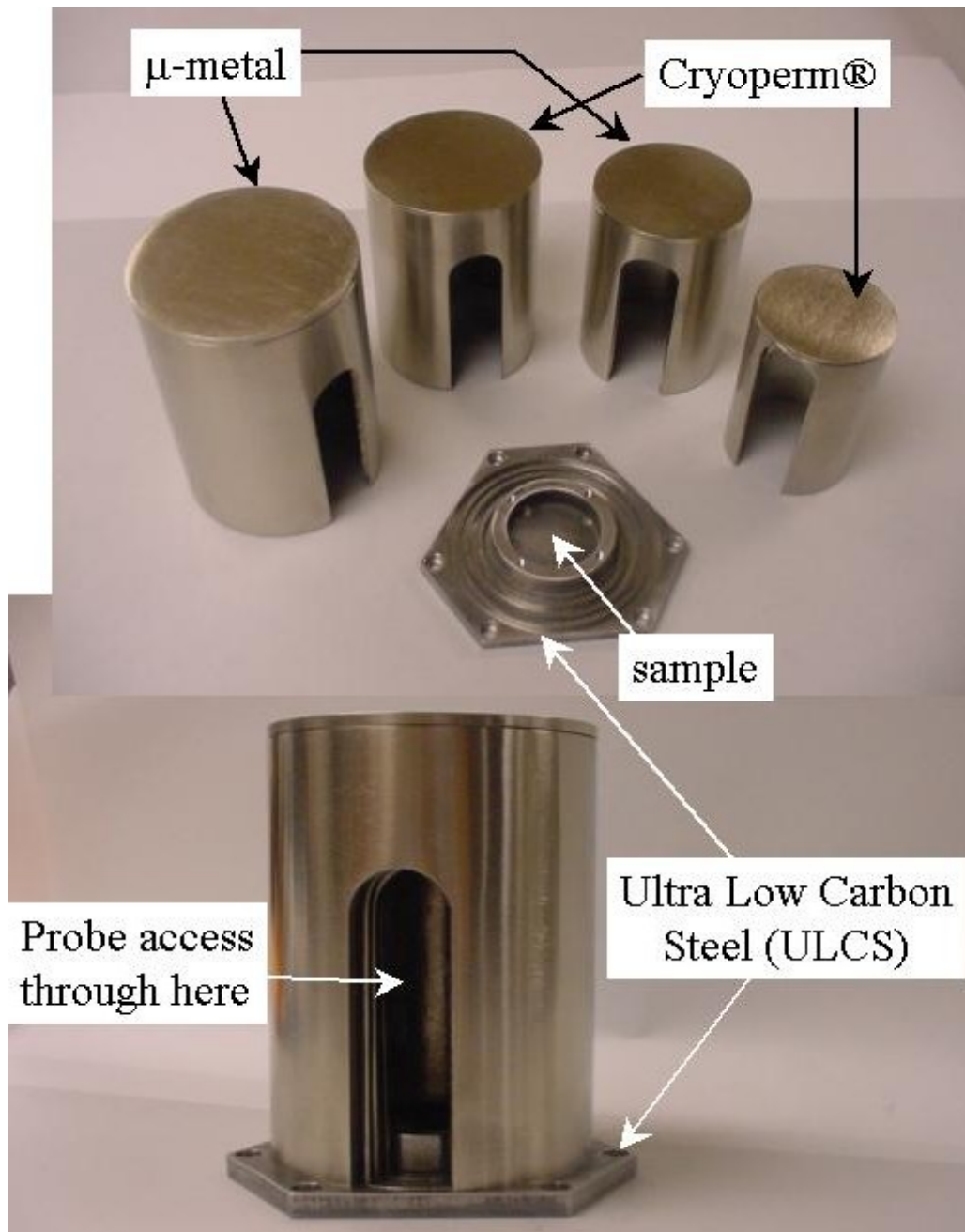


Fig. 5.4 Magnetic shielding assembly made by Amuneal. The lower picture shows the assembled shield. The upper picture shows the un-assembled view of the cylinders before they are nested together on the ultra-low carbon steel sample platform.

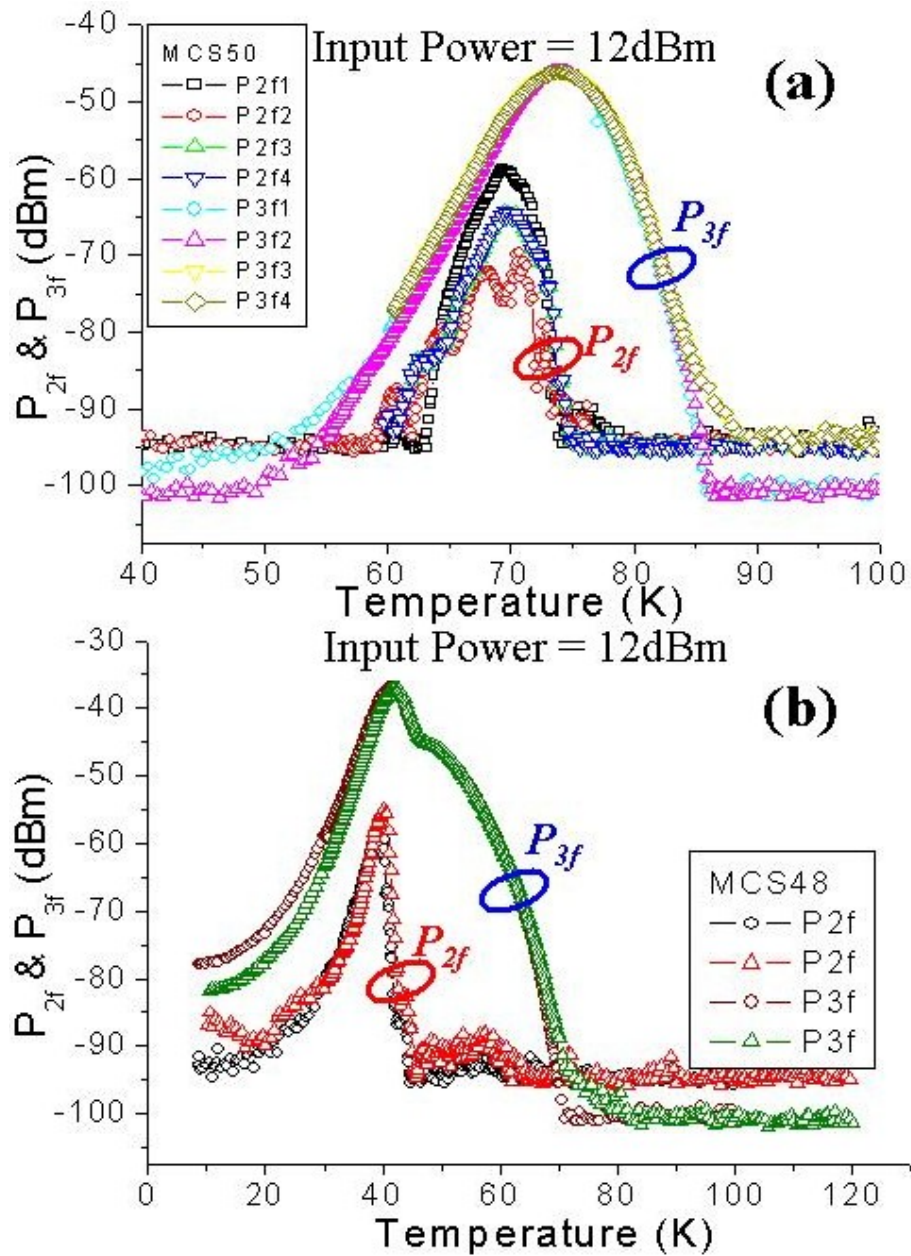


Fig. 5.5 Harmonic measurements of different samples taken after installation of the magnetic shielding assembly. Part (a) shows four runs of  $P_{2f}(T)$  and  $P_{3f}(T)$  on MCS50 while (b) shows two runs of  $P_{2f}(T)$  and  $P_{3f}(T)$  on MCS48, all near  $T_c$ .

#### 5.1.4 Determination of the doping level of $\text{YBa}_2\text{Cu}_3\text{O}_{7-\delta}$

We don't have a means to precisely and directly measure the oxygen deficiency, or the hole concentration,  $x$ . To estimate the hole concentration of our films, I use the approximate universal formula for  $T_c$  of HTSC vs.  $x$  [94],

$$\frac{T_c}{T_c^{\text{optimal}}} = 1 - 82.6(x - 0.16)^2. \quad (5.1)$$

Using this equation, I can convert from  $T_c$  measured by AC susceptibility to  $x$ . This formula was used successfully by an M.S. student in our lab, Senta Karotke [95], although she used it on oxygen-doped YBCO and Ca-doped YBCO crystals.

## 5.2 Doping-dependent quantities in HTSC

In spite of the controversial doping dependent TRSB nonlinearities discussed in Chapter 2, it is well accepted that some important quantities of superconductors vary with hole-concentration. For example, the doping dependence of the London penetration depth in the under-doped cuprates is well studied, although it is less clearly elucidated in the over-doped cuprates. Ultimately, I would like to study the doping dependence of the Meissner-state nonlinearity mechanism. Therefore, it is important to eliminate the doping dependent effect caused by quantities, e.g. the penetration depth, other than the nonlinear mechanism itself, so that the true doping dependence of the nonlinear mechanism can be revealed. In this section, I will discuss how such quantities manifest themselves in the harmonic measurements, and contribute to doping-dependent nonlinearities in HTSC.



### 5.2.1 London Penetration Depth

From Chapter 3 we know that the penetration depth comes into our determination of  $J_{NL}$ ,  $J_{NL}'$ , etc. In the early 90's, Uemura *et al.* [96] performed extensive muon spin relaxation ( $\mu$ -SR) experiments to measure the London penetration depth of HTSC cuprates. They claimed a universal result that  $\lambda(0)^{-2}$  (and by implication the super-fluid density divided by the effective mass) is linearly related to the  $T_c$  in the under-doped regime. Recent research on the effect of doping on the zero-temperature penetration depth,  $\lambda_0$ , of YBCO and  $La_{2-x}Sr_xCuO_4$  (LSCO) by Panagopoulos *et al.* [97] demonstrated similar results. The results on YBCO from various groups are listed in Table 5.2 with references. On the other hand, from the works of Panagopoulos *et al.* and Gou *et al.* [97,98], we find that the temperature dependence of  $\lambda$  is only weakly changed by doping in the under-doped regime, and can be legitimately approximated by the BCS or GL theory near  $T_c$  (most researchers see GL behavior of  $\lambda(T)$  near  $T_c$  in thin films). In the interpretation of data from our experiments, we will need to estimate the doping and temperature dependence of the magnetic penetration depth. We shall use the doping dependence of  $\lambda_0(x)$  from the literature, and the GL expression of  $\lambda(T) = \lambda_0 \left[ 1 - (T/T_c)^2 \right]^{-1/2}$  for temperatures near  $T_c$ .

Table 5.2 Summary of the penetration depth measurements on YBCO ceramics, thin films, and single crystals from various groups.

YBa <sub>2</sub> Cu <sub>3</sub> O <sub>7-δ</sub> samples	$\delta$	$T_c$ (K)	$\lambda_{ab}(0)$ ( $\mu\text{m}$ )	Reference
Aligned grain ceramic	0	92	0.14	[97]
Aligned grain ceramic	0.3	66	0.21	[97]
Aligned grain ceramic	0.43	56	0.28	[97]
Film	0.05	90.5	0.15	[98]
Film	0.2	83	0.216	[98]
Film	0.4	55	0.282	[98]
Crystal	0.05	93.2	0.1315	[99]
Crystal	0.4	59	0.185	[99]

### 5.2.2 Zero-Temperature Condensation Energy

Recent works done by Tallon's group [88, 89] reported the doping-dependent condensation energy in YBCO poly-crystals by measuring the electronic specific heat  $\gamma$ , vs. temperature.

The electronic entropy can be obtained by integrating the electronic specific heat

$S(T) = \int_0^T \gamma(T) dT$ , and the free energy density difference  $F_n - F_s = \mu_0 H_c^2(T)/2$  can be

obtained by integrating the entropy difference  $S_n - S_s$  between  $T_c$  and  $T$ , where  $H_c$  is the

thermodynamic critical field. The zero-temperature condensation energy density

$U(0) = \mu_0 H_c^2(0)/2$  can be derived from the specific heat data, as shown in Fig. 5.6.

Details of how to treat the experimental specific heat data and extract the zero-temperature condensation energy can be found in Ref. [100].

In addition to this data, since  $H_c \cong J_c \lambda$ , where  $J_c$  is the de-pairing critical current density (responsible for the NLME) and  $\lambda$  is the London penetration depth, we can extract the doping dependent de-pairing critical current density (at  $T = 0$ ) from this data,

$$J_c(T = 0, x) \approx H_c(0, x) / \lambda_0(x) = \sqrt{2U(0, x) / \mu_0} / \lambda_0(x),$$

where  $x$  denotes the doping dependence of these quantities. This leads to the conclusion that the NLME will be doping dependent.

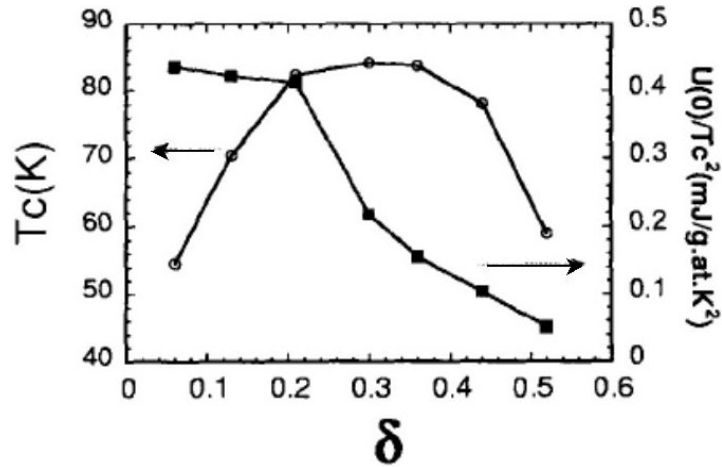


Fig. 5.6 Zero-temperature condensation energy density and  $T_c$ 's determined by Tallon's group [88, 89] via measurements of the specific heat of 30% Ca doped  $Y_{0.7}Ca_{0.3}Ba_2Cu_3O_{7-\delta}$  poly-crystals with various oxygen doping  $\delta$ .

### 5.3 Mechanisms of nonlinear response in under-doped YBCO

Experimentally, it has been a challenge for experimentalists to distinguish the origins of different types of nonlinear mechanisms from their results. The following are candidate nonlinear mechanisms which could be responsible for our results. Some strategies to distinguish between these mechanisms are also proposed.

#### 5.3.1 Background nonlinearity of the experimental apparatus

I am aware of higher harmonics generated by our microwave measurement system. To my knowledge, there are three main reasons for a circuit to respond in a nonlinear manner.

As mentioned earlier, my system consists of various microwave devices, which are most likely nonlinear to some extent. For example, transistors are used in amplifiers, which are known to be nonlinear devices. Secondly, if magnetic materials are present in the microwave circuit, the enhanced second and third harmonic signals are expected because of the hysteretic behavior of magnetic materials. I did my best to replace the coaxial cables, adapters, and connectors, which were made of magnetic materials (such as Ni plating), with ones made of non-magnetic materials. However, there are still some connectors that I could not replace with commercially available non-magnetic equivalents. Therefore, I must be aware of the harmonic signals generated by these connectors. Thirdly, it is also known that a bad electrical contact may also generate higher harmonics because of the presence of metal/insulator/metal interface in such contacts. Therefore, soldering is preferred to

mechanical clamping in making electrical contacts in coaxial connectors. However, there are places in our microwave circuit where devices and coaxial cables are connecting to each other directly or via adapters. In these cases, mechanical clamping is the only way to make electrical contacts (e.g. coaxial center conductor pin is clamped by the female receptacle). Therefore, while the best I can do is to clean the contact interfaces thoroughly, these contacts are still potentially troublesome in terms of harmonic generation. Articles regarding these issues can be found in Ref. [101], [102], and [103].

Despite these efforts, there is still non-linear background response from my measurement system. The way I treat this problem is to measure the harmonics generated by the system as a function of the driving frequency and amplitude. Though I did not intentionally make my microscope to be a microwave resonator, standing wave patterns are still present in the microwave circuit due to the inevitable impedance mismatches between devices. They are probably due to non-perfect electrical contacts or the impedance mismatch on the input/output ports of the amplifiers. By changing the driving frequency, we are changing the standing wave patterns in the circuit, and hoping to find some frequencies at which the harmonics generated by the three troublemakers discussed above are minimal. Shown in Fig. 5.7 is a measurement of the reproducible background harmonics generated by the system as a function of the driving frequency. This characteristic doesn't change much as the temperature is varied in my cryostat. From this, and other data, we know that the background harmonics come mainly from the microwave circuitry kept at room

temperature. Therefore, for all of my harmonic measurements, the driving frequency is fixed around 6.5GHz, where both  $P_{2f}$  and  $P_{3f}$  show no signals above the noise floor in Fig.

5.7.

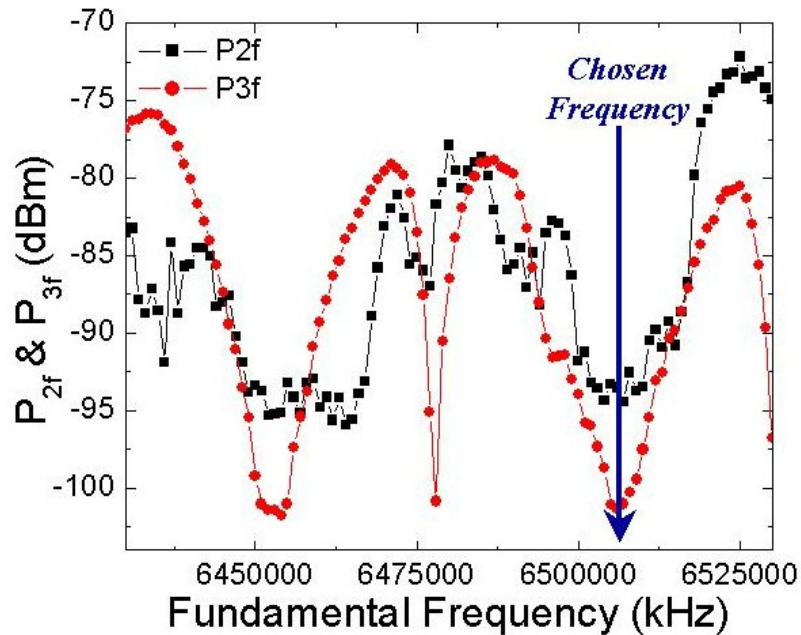


Fig. 5.7  $P_{2f}$  and  $P_{3f}$  generated by the system (background nonlinearity) as function of the driving frequency. No sample is present, and the microscope is at room temperature. The input power is 12 dBm.

### 5.3.2 Granularity and weak links

It is well known that the HTSC films of cuprates can be granular, which means grains and grain boundaries are naturally found in films deposited by various techniques [104]. The superconducting properties due to such granularity in thin films are usually modeled by a 2D network of weak links, each of which can be represented as a Josephson junction.

Through the work on an artificially prepared 1D weak-link feature, the bi-crystal YBCO grain boundaries (presented in the previous chapter) we have shown that an ERSJ model well describes the observed second and third harmonic generations from such features [7]. In the model, the second harmonic generation is attributed to the time-irreversible motion of the Josephson vortices along the boundary, while the third harmonic is expected from the nonlinear inductance of the Josephson junction. This work indicates that for a granular HTSC film, if a weak-link network is formed, and the Josephson effect dominates the behavior of this network, both second and third harmonic generations are likely to be observed because of the presence of Josephson junctions and Josephson vortices.

### 5.3.3 TRSB Physics

As described in Chapter 2, the TRSB nonlinear mechanisms in HTSC are not well understood. The proposal of Varma [64] claims the presence of a TRSB mechanism in all under-doped cuprates at all temperatures below the pseudo-gap temperature,  $T^*$ . This proposal has been tested by ARPES groups [65, 66], but no consensus has been reached on the interpretation of the data. With the capability to measure both TRS and TRSB nonlinear mechanisms, validated by our work on the YBCO bi-crystal grain boundaries, we should be able to test this proposal with our microscope.

Another proposal, also described in Chapter 2, is the Andreev Bound states nonlinearity. It is claimed by tunneling experimentalists [52, 56] that there are spontaneous surface

currents flowing in this surface state, which break the time-reversal symmetry. This may be an observation of the spontaneous surface magnetization proposed by Barash [60] for  $T \leq 0.01T_c$  in ABS. This TRSB state likely breaks up into domains on the surface. However, the doping dependence of these phenomena is controversial. Though my current set up does not allow me to extensively investigate nonlinear properties at such low temperatures (below 7K for Laura Green's proposal, below 1K for Barash's proposal), this microscope is potentially capable of such investigations.

#### 5.3.4 Tests to distinguish which model is most viable

As mentioned above, it is important to distinguish different mechanisms involved in our measurement. From the literature [105] and my work [7] on YBCO bi-crystal grain boundaries, harmonic generation, especially the second, from the weak-links should have a non-monotonic dependence on the input microwave power (see Fig. 4.2). On the other hand, since there are spontaneous currents or magnetizations associated with those intrinsic TRSB mechanisms in HTSC, it is likely that there is a characteristic scaling current density associated with each one. If these mechanisms manifest themselves in a manner as mentioned in Chapter 3, a monotonic power-2 dependence of the second harmonic signal on the input power is expected, and the magnitude of  $J_{NL}'$  should be in agreement with the theoretical predictions.



In the next chapter, I will present detailed analysis of the  $P_{2f}$  and  $P_{3f}$  data taken on variously doped YBCO thin films. Both  $J_{NL}$  and  $J_{NL}'$  ( $J_{TRSB}$ ) will be extracted and discussed in detail.

## CHAPTER 6

### DOPING DEPENDENT NONLINEARITIES IN HTSC

#### – DISCUSSION OF 2<sup>ND</sup> AND 3<sup>RD</sup> HARMONIC DATA

Taking the issues discussed in Chapter 5 into account, including proper magnetic shielding, selection of fundamental frequency, and estimates of the doping-dependent penetration depth, we can now perform reliable and reproducible harmonic measurements on YBCO thin films. Show in Fig. 6.1 is a typical harmonic data of an under-doped YBCO thin film. AC susceptibility data is also shown in this figure to determine  $T_c$  independently from the harmonic data. Both  $P_{2f}$  and  $P_{3f}$  data show a peak near  $T_c$ . The significant difference between them is that  $P_{3f}$  extends to  $T > T_c$  and  $P_{2f}$  drops to noise floor at  $T_c$ . Systematic study and analysis of  $P_{2f}$  and  $P_{3f}$  data will be discussed in this chapter.

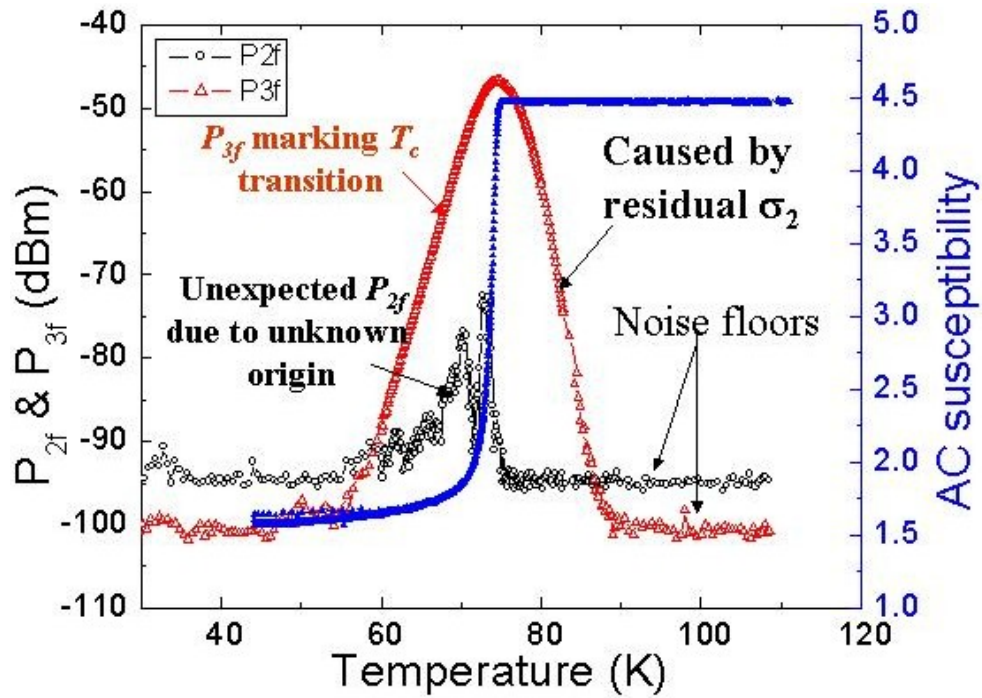


Fig. 6.1 A typical harmonic data (both  $P_{2f}$  and  $P_{3f}$ ) of an under-doped YBCO thin film with  $T_c \sim 75\text{K}$ . AC susceptibility data is shown to independently determine  $T_c$ .

### 6.1 Magnitude of $P_{3f}$ varies with doping levels

When harmonic measurements are performed on superconducting samples as a function of temperature, one signature is always seen. This signature marks the presence of the normal/superconducting phase transition, and appears as the enhanced  $P_{3f}(T)$  peaked at  $T_c$ , and dropping to the noise level at  $T \gg T_c$ . This phenomenon is qualitatively understood as follows. As the temperature approaches  $T_c$  from below, the super-fluid density is reduced, and the same perturbation (e.g. applied current) will cause a greater percentage suppression in super-fluid density, which leads to a stronger nonlinear response. Qualitative

descriptions are given by both the BCS and GL theories mentioned in Chapter 2, that the nonlinear response is basically determined by a scaling current density,  $J_{NL}(t)$ ,

$$\frac{n_s(t, J)}{n_s(t, 0)} = \frac{\lambda^2(t, 0)}{\lambda^2(t, J)} \cong 1 - \frac{J^2}{J_{NL}^2(t)}, \quad J \ll J_{NL},$$

where  $J$  is the applied current density,  $n_s$  is the super-fluid density,  $\lambda$  is the London penetration depth, and  $t=T/T_c$  is the reduced temperature. Since  $J_{NL}(t)$  goes to zero as  $t \rightarrow 1$ , the same amount of perturbation, which is  $J$ , produces greater change in the super-fluid density; producing a greater nonlinear response in harmonic measurements. [106]

### 6.1.1 Fitting and Temperature Normalization of the $P_{3f}(T)$ Measurements

In our typical third harmonic measurements (Fig. 6.1), such a peaked pattern as a function of temperature is certainly observed in all YBCO thin films.[106] We successfully fit these harmonic data with the Ginzburg-Landau theory, taking into account that there is a finite temperature range,  $\Delta T$ , over which the phase transition occurs. This finite temperature range is modeled as a Gaussian distributed  $T_c$  around the average  $T_c$ , with a width  $\Delta T$ . The temperature-dependent scaling current density is given in Eq. 2.6. Considering the fact that the  $P_{3f}(T)$  does not diverge, but shows a maximum near  $T_c$ , I must assume that the magnetic penetration does not diverge and the scaling current density does not go to zero at  $T_c$ . Therefore, additional parameters, which are the cut-off penetration depth and current density, are introduced as two fitting parameters in this model.

However, we also observed that the magnitudes and widths of the third harmonic responses are different for differently doped YBCO thin films. Optimally doped samples are fit well with  $T_c \cong 90\text{K}$  and a spread of  $T_c \cong 0.5\text{K}$  (Fig. 6.2(a)). In particular, the data just above  $T_c$  is fit well, all the way down to the noise floor. However, for the samples that are more under doped, the  $P_{3f}(T)$  tends to extend to  $T > T_c$ , and can no longer be fit with the GL theory above  $T_c$  (see Fig. 6.2(b); also in Fig. 6.1), and the  $P_{3f}(T)$  are more symmetric about their maximum value. This suggests the presence of residual  $\sigma_2$  above  $T_c$  [91], which strongly depends on the driving currents, and allows superconducting screening currents to flow.

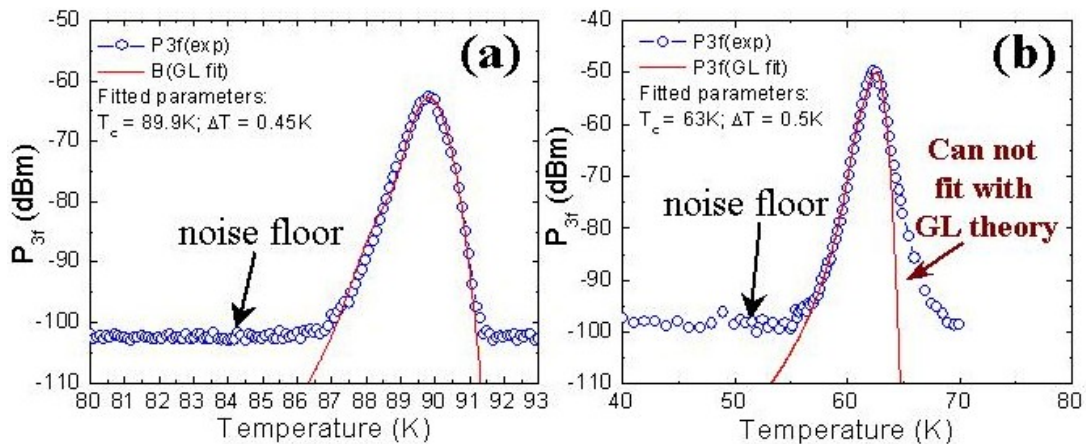


Fig. 6.2 Typical  $P_{3f}(T)$  data fitted by the Ginzburg-Landau theory, assuming finite phase transition width  $\Delta T$ . a) is an optimally-doped film, while b) is an under-doped film. As the films are more under doped, the residual  $P_{3f}$  extends to  $T > T_c$ , which cannot be fit by the GL theory anymore, and may indicate residual  $\sigma_2$  above  $T_c$ .

Fitting parameters for all samples are listed in Table 6.1. Note that the  $J_{NL}(0)$  – fit parameter generally increases as the  $T_c$  of the film increases. We shall see a similar trend from a different (and more reliable) analysis of the data later.

Table 6.1 Summary of the fitting parameters used in the Ginzburg-Landau model for  $P_{3f}(T)$  near  $T_c$  for most of my samples. The only one that can not be fit by this model is MCS48 because of its unusual  $P_{3f}(T)$  pattern, shown in Fig. 5.5.

	$T_c$ (K)	$\Delta T$ (K)	$J_{NL}(0)$ (A/m <sup>2</sup> )	$\lambda(0)$ ( $\mu\text{m}$ )	$\lambda(\text{cutoff})$ ( $\mu\text{m}$ )	$J_{NL}(\text{cutoff})$
MCS4	55.7	1.3	$6.5 \times 10^9$	0.286	0.45	$0.02J_{NL}(0)$
MCS1	63	0.5	$8.5 \times 10^9$	0.254	1.3	$0.019J_{NL}(0)$
MCS50	76.8	1.3	$4.7 \times 10^9$	0.222	0.43	$0.025J_{NL}(0)$
MCS2	85	0.48	$1.5 \times 10^{10}$	0.189	1.8	$0.019J_{NL}(0)$
MCS3	89.9	0.45	$9 \times 10^{10}$	0.12	2.5	$0.008J_{NL}(0)$

Presented in Fig. 6.3 and Fig. 6.4 are  $P_{3f}(T)$  measurements taken with and without the magnetic shielding assembly, where the temperatures are normalized by the  $T_c$ 's of the samples. Because the reproducibility of  $P_{3f}(T)$  near  $T_c$  is not sensitive to the presence of the magnetic shielding assembly, we include both types of data here.

Since the key quantities, such as the super-fluid density, of superconductors change rapidly near  $T_c$ , and significantly influence the data analysis, it is important to properly determine the  $T_c$ 's of the samples. Two different ways are used to determine the  $T_c$ . One is

to use the temperature of the maximum of  $P_{3f}(T)$ , which shall be referred to as  $T_c(pk)$ . The other is to independently perform the AC susceptibility  $\chi(T)$  measurements on the samples, and use the temperatures where the imaginary part of  $\chi(T)$  is peaked as the  $T_c$ , which shall be referred to as  $T_c(ac)$ . The data vs. temperature normalized by  $T_c(pk)$  is shown in (a), while normalized by  $T_c(ac)$  is shown in (b) in Figs. 6.3 and 6.4. We find that the  $T_c(ac)$  values are within the range  $T_c \pm \Delta T$  fitting parameter in the GL model for  $P_{3f}(T)$  near  $T_c$ . We expect the  $\Delta T$  – fit parameter to be smaller than that measured by ac susceptibility because the measured sample area by my loop probe is smaller than that of the ac susceptibility measurement. Independent of the temperature normalization, a common trend of increasing magnitude and width of  $P_{3f}(T/T_c)$  in under-doped YBCO thin films is observed (see Figs. 6.3 and 6.4), which will be discussed in detail later.

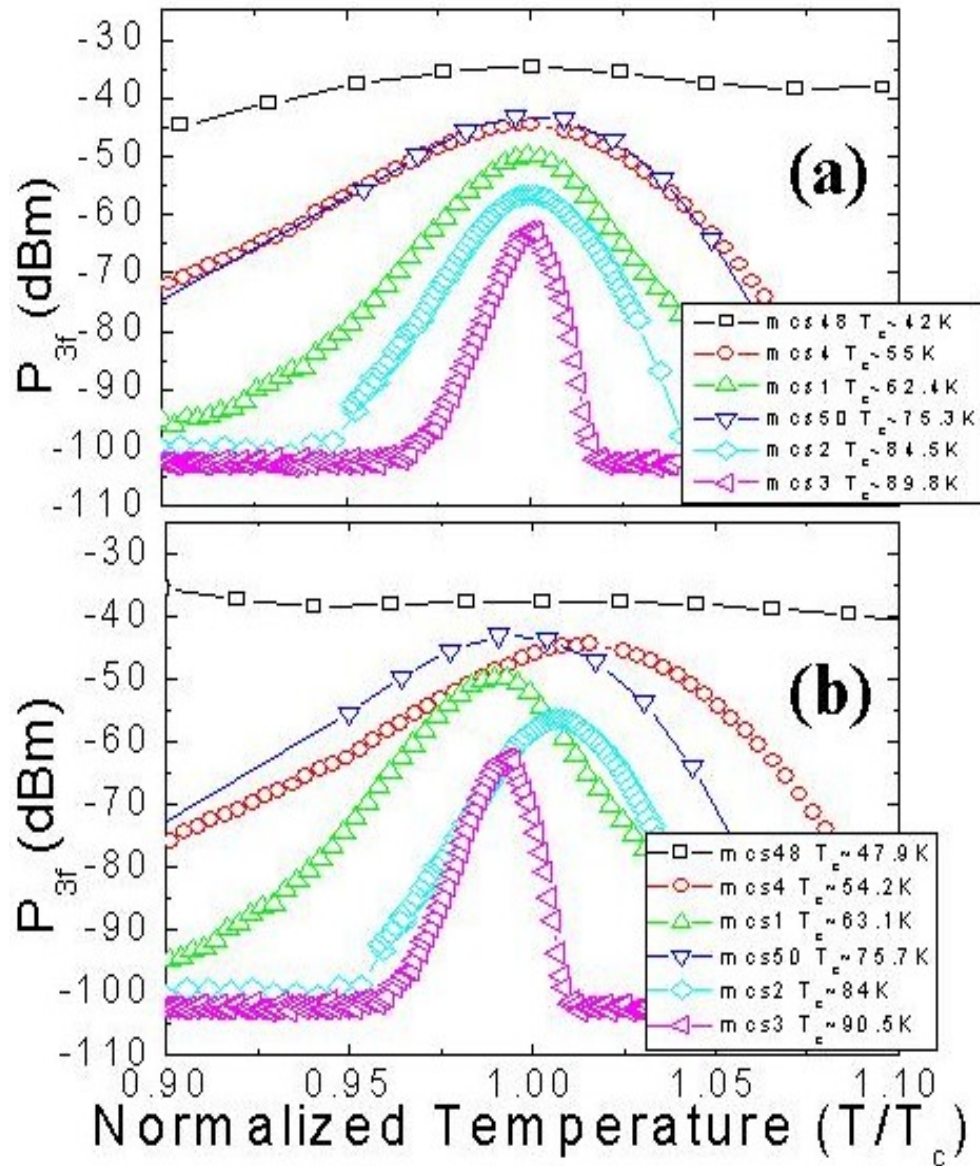


Fig. 6.3  $P_{3f}(T)$  data taken from variously doped YBCO thin films without the magnetic shielding assembly. The data is plot versus the normalized temperature ( $T/T_c$ ), determined by two different ways.  $T_c$ 's in (a) are determined by the temperatures where the  $P_{3f}(T)$  is at maximum ( $T_c(pk)$ ).  $T_c$  in (b) is determined by the AC susceptibility measurements, in which the imaginary part of  $\chi$  shows a peak ( $T_c(ac)$ ).



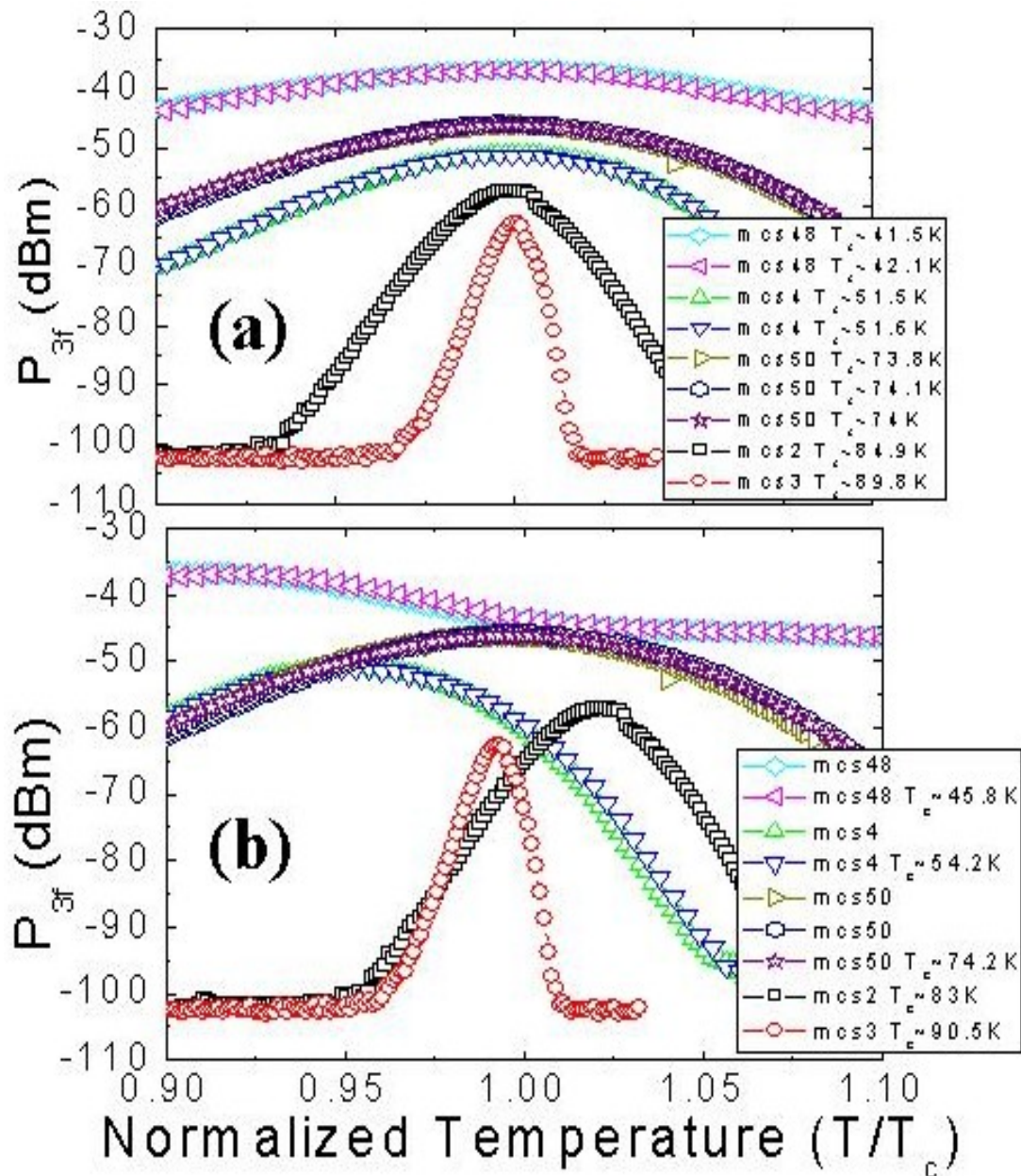


Fig. 6.4 Similar to Fig. 6.2,  $P_{3f}(T)$  data is plotted versus the normalized temperature, and (a) is normalized by  $T_c(pk)$ , and (b) is normalized by  $T_c(ac)$ . However, this data set is taken when the samples were placed in the magnetic shielding assembly.

We must be aware that neither method mentioned above is ideal. The former one depends not only on the temperature of the phase transition, but also where the magnetic penetration depth crosses over to the skin depth and normal metal screening dominates. The latter is a global measurements over an area of  $\sim (3\text{mm})^2$ , which does not give me the local  $T_c$  of the area I measure with the microwave microscope. Nonetheless, this normalization helps us to demonstrate how the nonlinear signals vary near the phase transition, and show how the residual  $P_{3f}$  extends to  $T/T_c > 1$  with lower doping levels.

### 6.1.2 Extraction of $J_{NL}$ from the $P_{3f}$ data

We must note that to quantitatively measure how nonlinear a mechanism is in a given sample, one needs to compare the magnitudes of the scaling current density,  $J_{NL}$ .

Therefore, we need to extract  $J_{NL}$  from our third order harmonic data. Though it is difficult to decide which temperature normalization is more appropriate via Fig. 6.3 and 6.4, by comparing  $J_{NL}$ 's extracted from both normalizations, it is found that normalization by the AC susceptibility measurements should be more appropriate, as discussed below.

Recall that the London penetration depth affects the measured  $P_{3f}$  (Chapter 3). Hence to understand our data, we must consider the doping dependence of the London penetration depth and remove it from our data. Taking the penetration depth data of thin films and crystals from the literature as summarized in Table 5.2, we found that  $\lambda_d(x)$  varies approximately linearly with  $x$  (Fig. 6.5) in our doping regime. Fitting  $\lambda_d(x)$  linearly with  $x$ ,

we have,

$$\lambda_0(x)(\mu m) \cong 0.49 - 2.31x, \quad (6.1)$$

where  $x$  is the hole concentration converted from the  $T_c$  using Eq. 5.1.

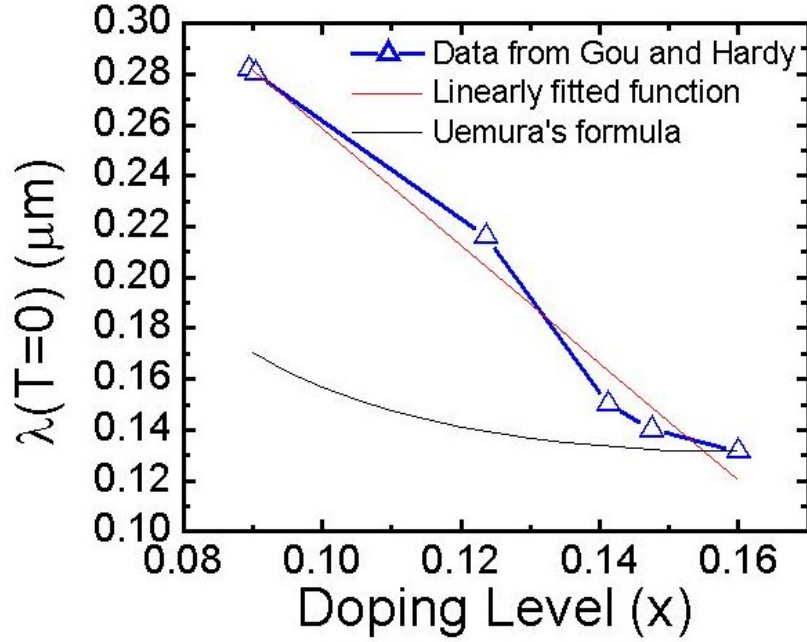


Fig. 6.5 Linear fit of the zero-temperature penetration depth  $\lambda(T=0)$ , measured from thin films and single crystals by Gou *et al.* [98] and Hardy *et al.* [99], versus the doping level  $x$ . The solid black line shows the expected  $\lambda(x)$  from Uemura's formula [96].

From Chapter 3, we have

$$\begin{aligned} P_{3f}(measured) &= 142.6 \times P_{3f}(sample) \\ &= \frac{142.6\Gamma^2}{2Z_0} \left( \frac{\omega\mu_0\lambda^2(T)}{4t^3 J_{NL}^2(T)} \right)^2, \end{aligned} \quad (6.2)$$

where  $\Gamma$  is the figure of merit  $\sim 31 \text{ A}^3/\text{m}^2$  estimated by HFSS (for a loop probe made of

.034” coaxial cable, hanging 12.5 $\mu\text{m}$  above the sample, with 12 dBm power output from the microwave synthesizer),  $t$  is the film thickness,  $Z_0 = 50 \Omega$  is the characteristic impedance of the transmission line and spectrum analyzer input, and  $\omega = 2\pi f$  is the fundamental angular frequency. Since the observed  $P_{3f}$  is doping dependent, with the information of the doping dependence of  $\lambda$ , we can extract the doping dependent  $J_{NL}$ ,

$$J_{NL}(x, T) \cong \sqrt{11.94\Gamma \times \frac{\omega\mu_0\lambda^2(x, T)}{4t^3\sqrt{2Z_0P_{3f}(\text{measured})(x, T)}}}. \quad (6.3)$$

Using this equation, the  $J_{NL}$  of the films in Fig. 6.3 and Fig. 6.4 are converted at  $T = 0.97T_c$ , where  $T_c$  is determined by the peak temperature of  $P_{3f}(T_c(pk))$  and the AC susceptibility measurements ( $T_c(ac)$ ), and presented in Fig. 6.6 as a function of the estimated hole concentration  $x$ .

One of the reasons for choosing  $T = 0.97T_c$  is that for  $T > 0.97T_c$  the analysis becomes very sensitive to the choice of  $T_c$  because of the diverging  $\lambda(T)$  at  $T_c$ . Since we do not measure the local  $T_c$  precisely, we would like to extract  $J_{NL}(x, T)$  at the lowest possible temperature. However,  $P_{3f}(T)$  drops to the noise floor below a certain temperature (e.g. both MCS2 and MCS3 show no  $P_{3f}$  signals above the noise floor below  $\sim 0.95T_c$  in Fig. 6.4(b)), which means that no meaningful  $J_{NL}$  can be extracted below such temperatures. As a result, we choose  $T = 0.97T_c$  to present the doping dependent trend of  $J_{NL}(x)$ , because it is where all the samples present a healthy  $P_{3f}$  signal above the noise floor, but is not too close to  $T_c$ .

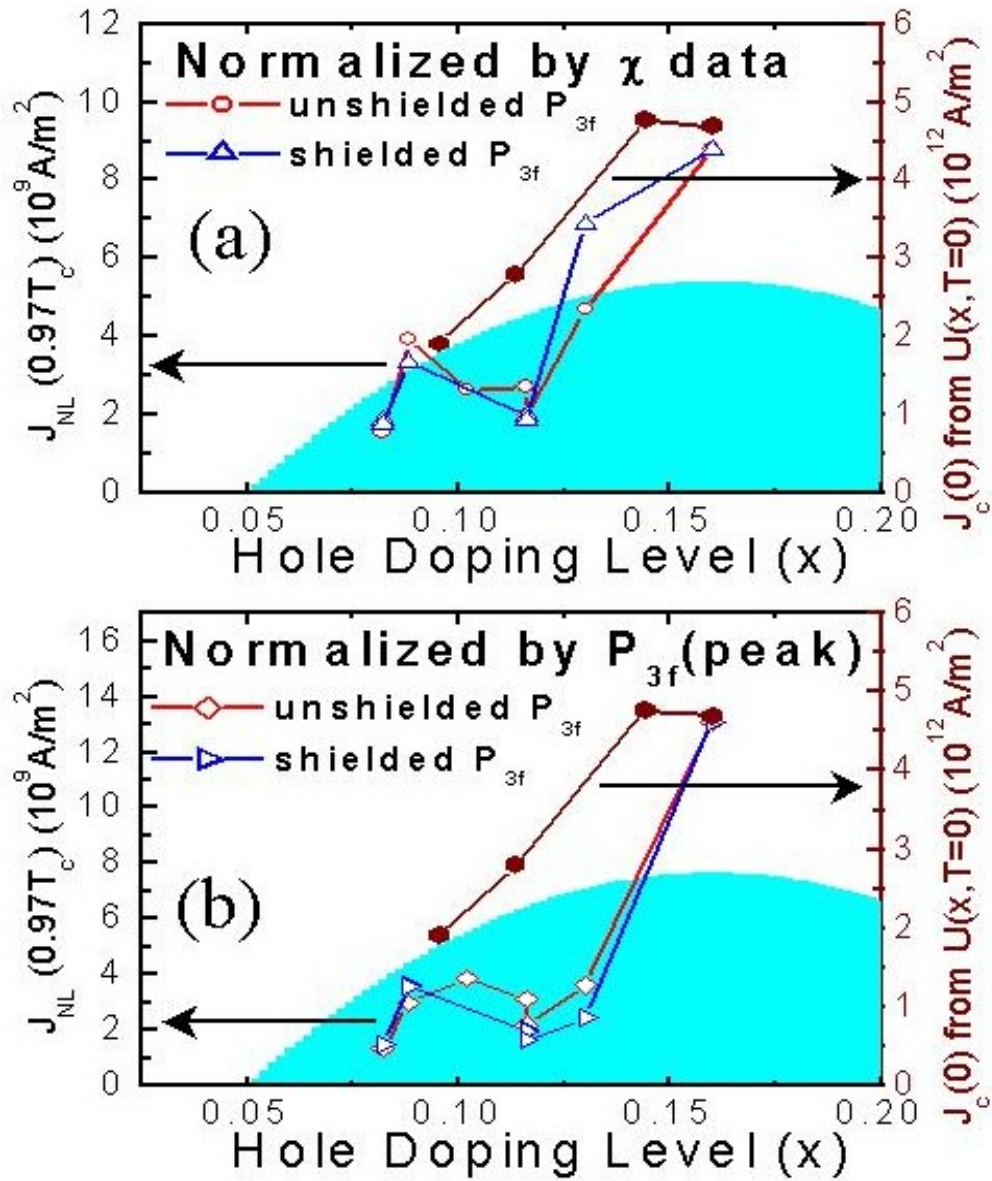


Fig. 6.6  $J_{NL}(0.97T_c)$  converted from the same set of  $P_{3f}$  data taken with/without the magnetic shielding assembly on variously doped YBCO thin films are presented together with the depairing critical current density  $J_c(T=0)$  converted from the zero-temperature condensation energy density measurements by Tallon *et al.* (a) and (b) are normalized by  $T_c(ac)$  and  $T_c(pk)$ , respectively. (a) demonstrates a clear trend of  $J_{NL}$  decreasing with lowering doping level, while (b) shows a less clear trend. The blue background schematically represents  $T_c$  vs. doping.

Another concern is that the assumption  $J/J_{NL} \ll 1$  is violated as the temperature gets too close to  $T_c$  because  $J_{NL}$  decreases rapidly near  $T_c$ . At  $T = 0.97T_c$ , the smallest extracted  $J_{NL}$  (from MCS48) is  $\sim 10^9$  A/m<sup>2</sup>, while the maximum applied current density is  $\sim 5 \times 10^8$  A/m<sup>2</sup> estimated by HFSS. This suggests that at higher temperatures, the assumption  $J/J_{NL} \ll 1$  will be violated at least in the center of the applied current distribution for the most under-doped samples. This concern also suggests that  $0.97T_c$  is a preferable temperature for analysis to find the trend of  $J_{NL}(x)$ .

Returning to Fig. 6.6, the extracted  $J_{NL}(x)$  taken from data with and without the magnetic shielding assembly are presented. While the  $J_{NL}$  extracted from the results normalized by the  $T_c(pk)$  do not show such a clear trend with varying doping levels (Fig. 6.6(b)), the  $J_{NL}$  from the results normalized by the  $T_c(ac)$  clearly indicate that the scaling current density, which is the de-pairing critical current density for the NLME, decreases with decreasing hole concentration (Fig. 6.6(a)). The only exception is MCS50, whose doping level is  $x \cong 0.12$ . The harmonic measurements of this sample show broader patterns than expected, but the cause of this exception is not clear to me. Clearly the trend for  $P_{3f}(x)$  is not affected by the absence or presence of the magnetic shielding assembly.

Recent work on specific heat of variously doped YBCO poly-crystals [88, 89] demonstrated that the zero-temperature condensation energy density  $U(0)$  decreases with decreasing doping level. Following the argument in the earlier section (5.2.2), we can

conclude from this work that the intrinsic de-pairing critical current density should therefore be smaller in under-doped YBCO.

The comparison between the  $J_{NL}(0.97T_c)$  from our harmonic measurements and the  $J_c(0)$  from Tallon's specific heat measurements is also shown in Fig. 6.6. Consistency between the two results in the overall trend is shown. It is noted that the magnitudes of  $J_{NL}(0.97T_c)$  is much smaller than  $J_c(0)$ , which is expected since the de-pairing critical current density decreases to zero as the temperature approaches  $T_c$ .

### 6.1.3 Note on the choice of $\lambda(x, T)$

As mentioned in previous sections, the doping- and temperature-dependence of  $\lambda(x, T)$  is important in our extraction of  $J_{NL}$ . There are two assumptions made about  $\lambda(x, T)$ . One is that the temperature dependence is based on the mean-field theory (GL) rather than the 3D-XY theory. This assumption is tested by using Vigni's model described in Chapter 2 to calculate the expected  $P_{3f}(T)$  from the GL theory and 3D-XY theory for  $\lambda(T)$ . We find that the 3D-XY theory produces a much narrower peak pattern in  $P_{3f}(T)$  than the GL theory, and is very difficult to fit to our experimental data. Therefore, the temperature dependence of  $\lambda(x, T)$  based on the GL theory is more appropriate in our case.

Secondly, the doping dependence of  $\lambda(x, 0)$  is obtained by fitting the experimental data from the literature. Rather than using Uemura's formula [96], I fit the data with a linear function of doping. However, even if Uemura's formula (Fig. 6.5) is used to fit these data,

the difference in  $\lambda(x, T)$  will only magnify the trend in  $J_{NL}(x)$ , which changes by a factor of  $\sim 5$  with a linear function of  $\lambda(x)$  in our doping range.

## 6.2 The unusual $P_{2f}$ peak seen near $T_c$ in all under doped films

As demonstrated earlier in this chapter, the second harmonic also shows astonishing features near  $T_c$  in under doped YBCO thin films, which are not expected from the NLME. Similar to what I've done to the  $P_{3f}$  data, the  $P_{2f}$  data is also normalized by the two alternative  $T_c$  values mentioned previously. As shown in Fig. 6.7, the  $P_{2f}$  data normalized by  $T_c(pk)$  shows residual signals above  $T_c$  (Fig. 6.7(a)), while the onset of  $P_{2f}$  aligns very well at  $T_c$  if normalized by  $T_c(ac)$  (Fig. 6.7(b)). Since the sensitivity of my microscope to TRSB nonlinearities relies on the large screening currents flowing in superconducting state (but largely absent in the normal state), I should be sensitive to TRSB nonlinearities (in  $P_{2f}$  signals) only at and below  $T_c$ . Therefore, this serves as another indication that normalization by  $T_c(ac)$  is more appropriate. On the other hand, the absence of  $P_{2f}$  observed above  $T_c(ac)$  suggests that  $P_{2f}$  comes from the establishment of long-range phase coherence. This clearly contrasts with the  $P_{3f}(T)$  data which extends well above  $T_c$ , and does not require the establishment of long-range phase coherence.



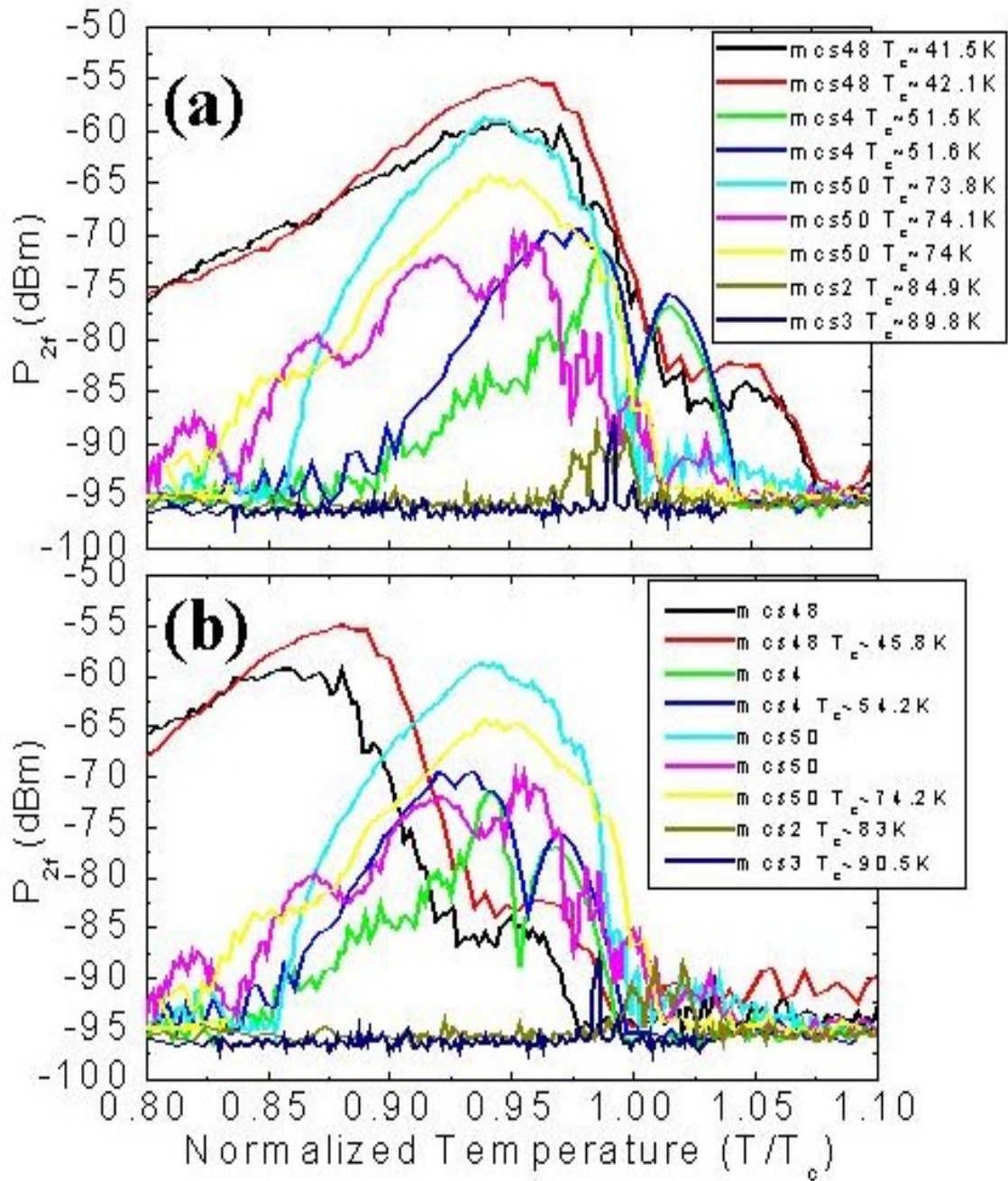


Fig. 6.7  $P_{2f}(T)$  data near  $T_c$  normalized by the  $T_c$ 's of the oxygen-doped samples. (a) is normalized by  $T_c(pk)$ , and (b) by  $T_c(ac)$ .

### 6.2.1 Extraction of $J_{NL}'$ from $P_{2f}$ data

As an attempt to understand this peak feature, I propose the hypothesis for second harmonic generation which is described in detail in chapter 3. This proposal assumes that the modulation of the super-fluid density by currents is now modified by the presence of the spontaneous currents caused by the responsible TRSB mechanism, and the modulated super-fluid density becomes

$$\frac{\rho_s(T, J)}{\rho_s(T, 0)} \cong 1 - \frac{J}{J_{NL}'(T)} - \left( \frac{J}{J_{NL}(T)} \right)^2, \quad J \ll J_{NL}(T), J_{NL}'(T),$$

where  $J_{NL}'(T)$  is the scaling current density which in general (phenomenologically) represents the TRSB nonlinearities.

Following the same algorithm described in chapter 3, the  $J_{NL}'(T)$  is derived from the  $P_{2f}$  data via

$$\begin{aligned} P_{2f}(\text{measured}) &= 900 \times P_{2f}(\text{sample}) \\ &= \frac{900\Gamma'^2}{2Z_0} \left( \frac{\omega\mu_0\lambda^2(T)}{2t^2 J_{NL}'(T)} \right)^2, \end{aligned} \quad (6.4)$$

where  $\Gamma'$  is the figure of merit  $\sim 1.1 \text{ A}^2/\text{m}$  estimated by HFSS (for a loop probe made of .034" coaxial cable, hanging  $12.5\mu\text{m}$  above the sample, with 12 dBm power output from the microwave synthesizer),  $t$  is the film thickness,  $Z_0 = 50 \Omega$  is the characteristic impedance of the transmission line and spectrum analyzer input, and  $\omega = 2\pi f$  is the fundamental angular frequency. Including the doping-dependent penetration depth  $\lambda(x, T)$ ,

we can extract  $J_{NL}'$  via

$$J_{NL}'(x,T) \cong 30\Gamma \times \frac{\omega\mu_0\lambda^2(x,T)}{2t^2\sqrt{2Z_0P_{2f}(measured)(x,T)}}, \quad (6.5)$$

for variously doped YBCO thin films, as shown in Fig. 6.8.

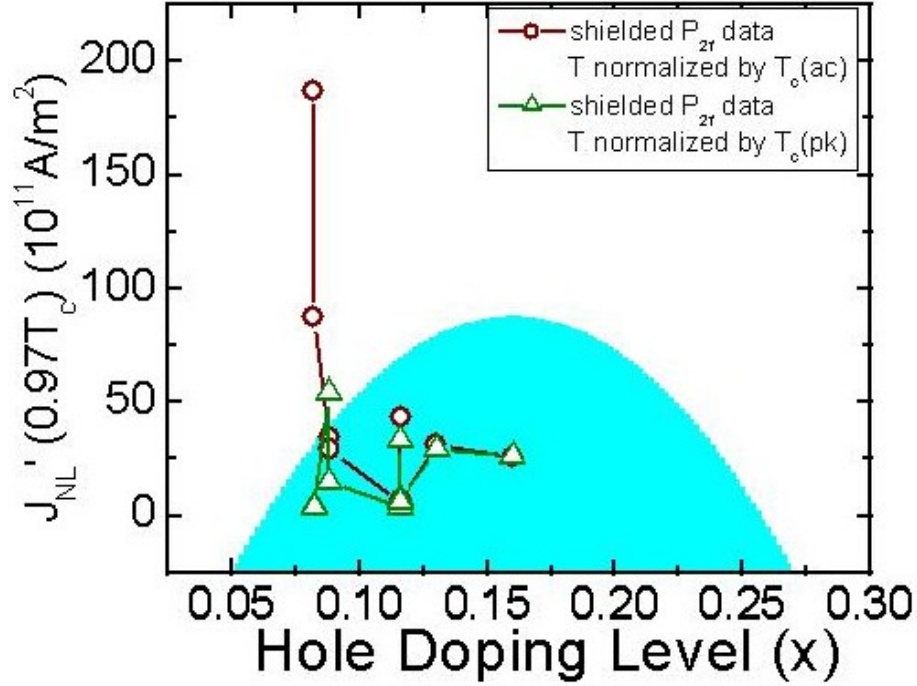


Fig. 6.8  $J_{NL}'$  at  $0.97T_c$  extracted from  $P_{2f}(T)$  data of variously doped YBCO thin films using Eq. 5.6. The temperatures are normalized by  $T_c(ac)$  (circles) and  $T_c(pk)$  (triangles) in the two sets of data, respectively.

What is shown in Fig. 6.8 are the  $J_{NL}'$  extracted from the  $P_{2f}(T)$  data taken with the magnetic shielding assembly, so that the effect of induced vortices by external magnetic fields is minimized. The  $J_{NL}'$  is calculated at  $T = 0.97T_c$ , the same as for  $J_{NL}$  in the previous

section, for comparison. It is noted that the  $J_{NL}'$  calculated from the data normalized by  $T_c(ac)$  shows a trend of generally increasing as the doping level is decreased, while the other normalization doesn't show any clear trend. As in the discussion of  $J_{NL}(x)$ , the discussion below will only focus on the analysis normalized by  $T_c(ac)$ .

The trend of increasing  $J_{NL}'$  for lower doping levels can be understood as follows. As mentioned earlier,  $J_{NL}'$  was proposed phenomenologically to account for a second harmonic response. However, it can be related to the physically-motivated spontaneous current  $J_{TRSB}$  generated by an unknown TRSB mechanism as  $J_{NL}' = J_{NL}^2 / 2J_{TRSB}$  (Eq. 3.10). By converting the  $J_{NL}$  and  $J_{NL}'$  data into  $J_{TRSB}$ , we can see a clear decreasing trend of  $J_{TRSB}$  upon lowering the doping level, which is shown in the inset of Fig. 6.9. This suggests that the magnitude of the spontaneously generated TRSB current density decreases with decreasing doping, similar to the trend expected for the intrinsic de-pairing critical current density, also shown in the inset of Fig. 6.9.

More importantly, we can directly determine  $J_{TRSB}(T)$  from the raw data, independent of the choice of  $T_c$ , and how we define the doping and temperature dependence of  $\lambda$ . From Eq. 6.3 and Eq. 6.5, we have

$$\begin{aligned}
 J_{TRSB}(T) &= \frac{J_{NL}^2(T)}{2J_{NL}'(T)} = \frac{11.94\Gamma\phi\mu_0\lambda^2(x,T)/(4t^3\sqrt{2Z_0P_{3f}(T)})}{60\Gamma'\phi\mu_0\lambda^2(x,T)/(2t^2\sqrt{2Z_0P_{2f}(T)})} \\
 &\cong \frac{2.8(A/m)}{t} \sqrt{\frac{P_{2f}(T)}{P_{3f}(T)}},
 \end{aligned} \tag{6.6}$$

where  $t$  is the film thickness, and  $\Gamma$  and  $\Gamma'$  are assumed to be  $\sim 31 \text{ A}^3/\text{m}^2$ , and  $1.1 \text{ A}^2/\text{m}$ , respectively. Note that the magnitude and temperature dependence of  $J_{TRSB}$  is uniquely determined by the  $P_{2f}(T)$  and  $P_{3f}(T)$  measurements with a minimum of assumptions.

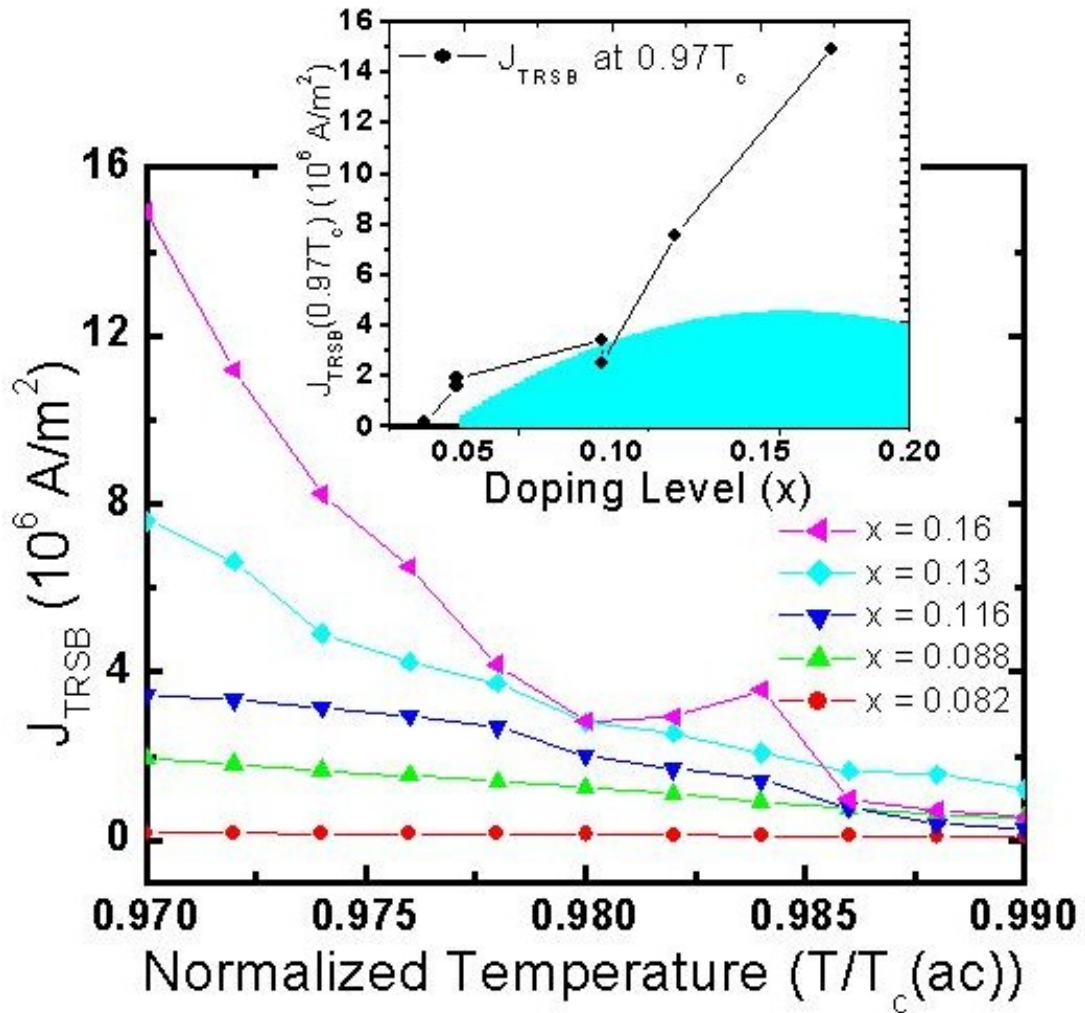


Fig. 6.9  $J_{TRSB}$  vs.  $T/T_c(ac)$  for variously doped YBCO thin films.  $J_{TRSB}$  of all samples shows a clear trend of dropping to zero at, or at least near,  $T_c$ . The magnitude of  $J_{TRSB}$  is also doping dependent. Shown in the inset is the  $J_{TRSB}$  at  $0.97T_c$ , which shows a clear decreasing trend in lower doping levels.

The main part of Fig. 6.9 shows the temperature dependence of  $J_{TRSB}$  deduced from Eq. 6.6 of variously doped YBCO thin films over the temperature range  $0.97 \sim 0.99T_c$ . To illustrate the temperature dependence, we use the  $T_c(ac)$  to normalize the temperatures in the data. (The reason for the lower limit of  $0.97T_c$  is that either the  $P_{2f}(T)$  or  $P_{3f}(T)$  data drops to the noise floor at that temperature so that the derived  $J_{TRSB}$  does not make sense below such temperatures.) In addition to the trend of decreasing  $J_{TRSB}$  at lower doping levels, an astonishing common onset of  $J_{TRSB}(T)$  is observed at, or just below,  $T_c(ac)$ . The development and growth of  $J_{TRSB}(T)$  below  $T_c$  is reminiscent of the development of a TRSB order parameter as described by Sigrist [58]. It is similar to the measurement of a spontaneous internal magnetic field as measured in  $\text{Sr}_2\text{RuO}_4$  by Luke *et al.* with muon spin relaxation [107].

We are aware of the fact that our microscope is not sensitive to nonlinearities in the normal state. Therefore we cannot make a direct comment about Varma's proposal of a spontaneous current flowing along Cu-O bonds with an onset at  $T^* > T_c$ . However, the remarkable onset of  $J_{TRSB}(T)$  near  $T_c$  suggests that the  $P_{2f}$  signal we measured near  $T_c$  is associated with the establishment of long-range phase coherence at  $T_c$ . Therefore, it seems unlikely that non-zero  $J_{TRSB}(T)$  exists at temperatures above  $T_c$ . One support of this interpretation is the observation of spontaneous magnetic moments ("vortices with fractional flux quantum") in YBCO films at  $T \leq T_c$  by Kirtley *et al.* [108] using their scanning SQUID microscope. They attributed these "vortices" to the pinning of a vortex

tangle because of the disorder present in the film, or to local broken time-reversal symmetry because of non-ferromagnetic defects found in the film. This suggests that  $J_{TRSB}$  might be the circulating currents associated with the formation of vortices. In addition, the increase in the magnitude of  $J_{TRSB}$  upon cooling below  $T_c$  is consistent with the results of Kirtley, *et al.* [108] that show an increase in flux strength in the “fractional vortices” observed in (001) YBCO films cooled in zero field. This would explain the clear onset at  $T_c$  due to the establishment of long-range phase coherence required to create long-lived vortex excitations. On the other hand, other attempts to generate spontaneous flux after a quench through  $T_c$  seem to require enormous quench rates ( $\sim 10^8$  K/s) to produce measurable flux [109].

Secondly, the magnitude of  $J_{TRSB}$  is  $\sim 10^7$  A/m<sup>2</sup> in the optimally doped sample near  $T_c$ , and this magnitude decreases as the doping level decreases. Note that this is significantly less than  $J_{NL}(0.97T_c)$ , by several orders of magnitude. If we naively assume that the  $J_{TRSB}$  is proportional to the weak-link critical current density, the trend I observe is consistent with measurements of the critical current density  $J_c$  of 23° mis-oriented YBCO bi-crystal grain boundaries as a function of oxygen doping [110]. There they see a drop of  $J_c$  by a factor of  $\sim 100$  upon going from optimally doped YBCO to oxygen under-doped YBCO with a  $T_c$  of  $\sim 50$ K. We do not have 23° mis-oriented bi-crystal grain boundaries in our films, but low-angle junctions should have a similar trend with doping.

In addition, I can estimate the magnetic fields on the sample surface induced by  $J_{TRSB}$ . Since the thickness  $t$  of my films is  $\sim 1000\text{\AA}$ , which is much smaller than the penetration depth near  $T_c$ , I can assume that the current is flowing uniformly throughout the thickness. The magnetic field on the surface is estimated as

$$B = \mu_0 H = \mu_0 J_{TRSB} t \approx 4\pi \times 10^{-7} \times 10^7 \times 10^{-7} \approx 1.26 \mu T = 12.6 mG .$$

The primary method to measure spontaneous fields in superconductors is muon spin relaxation ( $\mu$ -SR) [107,111]. The published sensitivity limits of these measurements are 800 mG [111] and 100 mG [107]. These results suggest that my technique has superior sensitivity for the detection of spontaneous fields/currents in the superconducting state.

### 6.3 Power dependence measurements of $P_{2f}$ and $P_{3f}$

To develop a clearer picture about the origins of the  $P_{2f}$  and  $P_{3f}$  signals near  $T_c$ , we must check the power dependence. Different power dependent behaviors are expected for the different nonlinear mechanisms. For example, although an enhanced  $P_{3f}$  is expected in d-wave superconductors at low temperatures (Chapter 2), a transition from power-3 dependence to power-2 of  $P_{3f}(P_f)$  is expected upon cooling through  $\sim 0.01T_c$  [32]. Therefore, the power dependence of the measured harmonic signals becomes another important source of information in determination of the responsible nonlinear mechanism.



The third harmonic generation is attributed to the NLME near  $T_c$  in my work. This leads to an expected  $P_{3f} \propto P_f^3$  (power-3 dependence), which can be clearly seen from Eq. 3.6. On the other hand, my proposal for the TRSB scaling current density  $J_{NL}'$  should lead to the conclusion of  $P_{2f} \propto P_f^2$  (power-2 dependence) according to Eq. 3.12.

I measured both the  $P_{2f}(P_f)$  and  $P_{3f}(P_f)$  around  $T_c$  before I obtained the magnetic shielding assembly. While the  $P_{3f}(P_f)$  data shows a very stable and consistent power-3 behavior in all samples, the  $P_{2f}(P_f)$  data was not that reproducible. While some of the  $P_{2f}(P_f)$  data show reproducible power-2 dependence on  $P_f$ , variations from power-2 dependence were observed. Shown in Fig. 6.10 are the  $P_{2f}(P_f)$  and  $P_{3f}(P_f)$  of MCS1 and MCS4 taken at temperatures around their respective  $T_c$ 's. Consistent and stable power-3 dependence in  $P_{3f}(P_f)$  is shown, while the  $P_{2f}(P_f)$  is much noisier and the power-law dependence is not so easily defined (slopes range from  $\sim 1.6$  to 2).

One might consider heating as a problem in the power-dependence measurements, especially at higher power. This issue has been considered by comparing  $P_{3f}(T)$  near  $T_c$  measured above non-GB and GB shown in Chapter 4. Since the GB is more dissipative than plain YBCO, if the heating effect is significant, I should observe a significant shift in the  $P_{3f}(T)$  peak. However, I only observe less than 0.5K shift of  $T_c$ , which can be caused by inhomogeneity of the film. Hence I conclude that heating is not a significant issue in my measurements.

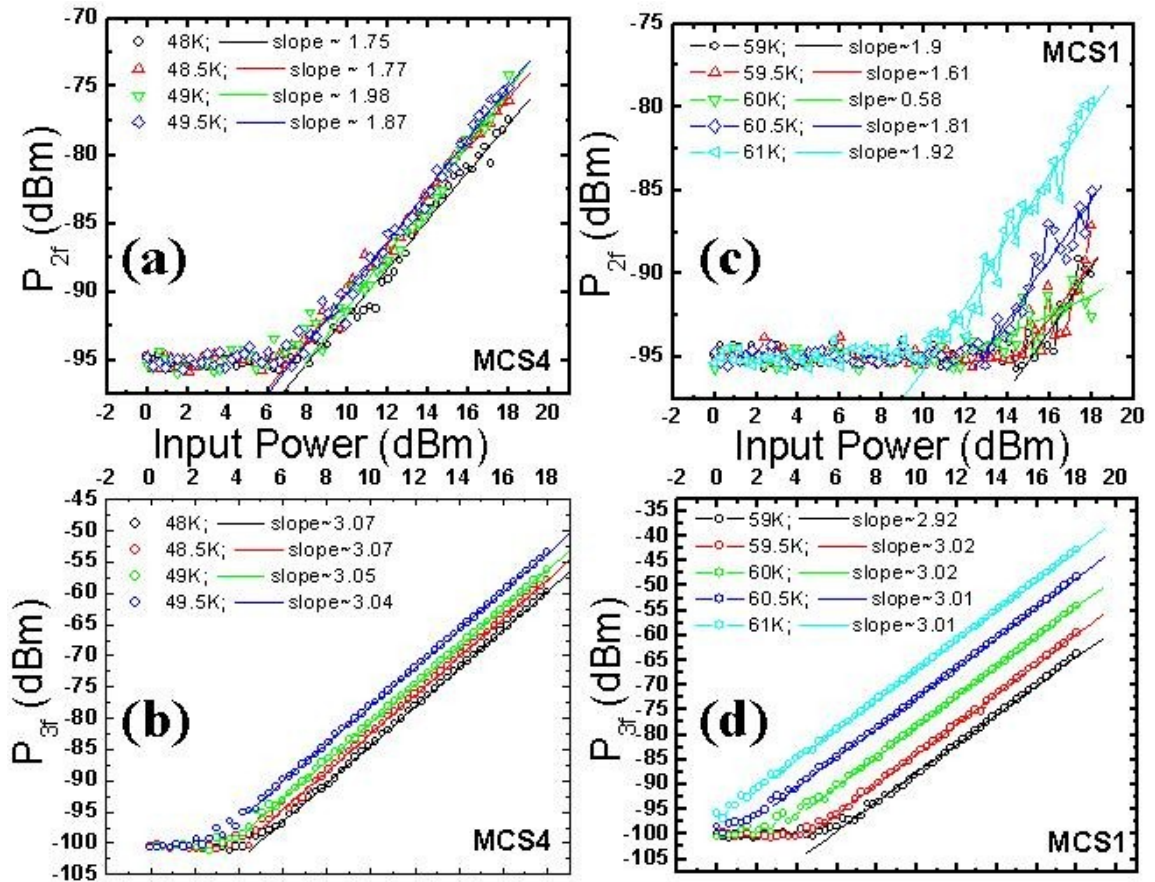


Fig. 6.10 (a) and (b) are  $P_{2f}(P_f)$  and  $P_{3f}(P_f)$  of MCS4, and (c) and (d) are  $P_{2f}(P_f)$  and  $P_{3f}(P_f)$  of MCS1 near  $T_c$ . Fitting for the slope is also shown with each data set. This set of data was taken before the installation of the magnetic shielding assembly.

Since magnetic vortices are potentially involved in these measurements, I intended to repeat these power-dependence measurements after the installation of the magnetic shielding assembly. However, at the time I started to measure  $P_{2f}(P_f)$  and  $P_{3f}(P_f)$ , most of the samples had degraded severely. One signature of the severe degradation is very strong  $P_{2f}$  and  $P_{3f}$  signals persisting from near  $T_c$  to the low temperature region. This was not

observed when I took the magnetically shielded  $P_{2f}(T)$  and  $P_{3f}(T)$  data presented in previous sections. Secondly, the non-monotonic power-dependence is not only observed in  $P_{2f}(P_f)$ , but also in  $P_{3f}(P_f)$ , as shown in Fig. 6.11 in which the data of MCS1 and MCS4 are presented. This is a clear indication that the Josephson nonlinearity dominates the nonlinear response [105] for I have also observed a similar power-dependent behavior on the bi-crystal YBCO thin film (Fig. 4.2).

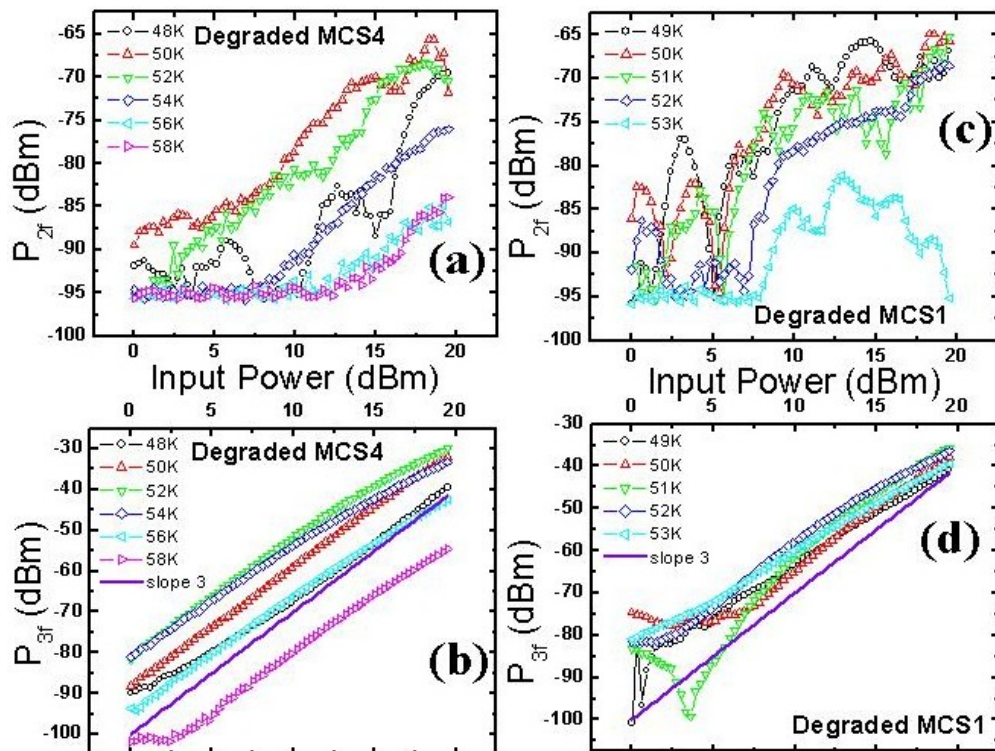


Fig. 6.11 After the installation of the magnetic shielding assembly, most of my samples have degraded and the harmonic measurements look like this. (a) and (b) are  $P_{2f}(P_f)$  and  $P_{3f}(P_f)$  of MCS4, and (c) and (d) are  $P_{2f}(P_f)$  and  $P_{3f}(P_f)$  of MCS1. Non-monotonic patterns are observed in  $P_{2f}(P_f)$ , and in some cases, in  $P_{3f}(P_f)$  as well.  $P_{3f}(P_f)$  also shows unexpected curving away from power-3 behavior.

The only sample whose  $P_{2f}(P_f)$  and  $P_{3f}(P_f)$  remained well behaved is MCS2. Shown in Fig. 6.12 is the  $P_{2f}(P_f)$  and  $P_{3f}(P_f)$  of MCS2 at temperatures around  $T_c$ , which show close to power-2 and power-3 dependence respectively. Using this data for MCS2, I extracted  $J_{TRSB}$  at different power levels to see if the procedure defined by Eq. 6.6 is robust. I find that the  $J_{TRSB}$  values are constant, independent of input power, to within  $\pm 10\%$ . This demonstrates that the nearly assumption-free determination of  $J_{TRSB}$  is robust and valid.

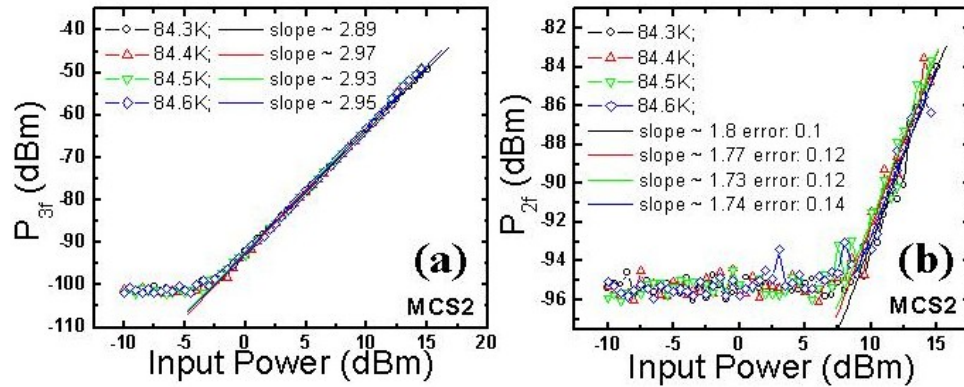


Fig. 6.12  $P_{2f}(P_f)$  and  $P_{3f}(P_f)$  of MCS2 taken with the magnetic shielding assembly. Power-3 dependence is clearly shown in  $P_{3f}(P_f)$ , and the power-law dependence of  $P_{2f}(P_f)$  ranges from  $\sim 1.73$  to 1.8, which is reasonably close to 2.

## 6.4 Conclusion

In this chapter, I have demonstrated a systematic study of the doping dependent nonlinearities of high- $T_c$  superconductors near  $T_c$  using a set of variously under doped YBCO thin films. The analysis of the third harmonic generation, which we believe is mainly caused by the NLME near  $T_c$ , leads to a conclusion of enhanced NLME (smaller

$J_{NL}$ ) for lower doping levels. This is in agreement with a completely independent study of the zero-temperature condensation energy of variously doped YBCO crystals by Tallon *et al.*

The second harmonic generation near  $T_c$  is interpreted as the manifestation of a spontaneous current  $J_{TRSB}$  generated by an unknown TRSB mechanism, as described in Chapter 3. One prediction of this model is the power-2 dependence of  $P_{2f}(P_f)$ , which is observed in the power-dependence measurements. It is important to remember that the analysis for extracting  $J_{TRSB}(T)$  does not depend on the doping and temperature dependent magnetic penetration depth  $\lambda(x, T)$  or a choice of  $T_c$ , but solely on the ratio of the measured  $P_{2f}$  and  $P_{3f}$ , and the film thickness, which are all well measured. From the analysis, a remarkable onset of  $J_{TRSB}(T)$  is shown at, or at least near,  $T_c$ . In addition, the magnitude of  $J_{TRSB}$  becomes progressively smaller in more under doped YBCO thin films. These observations are consistent with a weak-link vortex mechanism for the TRSB, although this is by no means definitive.

It is also noted that the model for the second harmonic generation is a phenomenological model, lacking of solid theoretical background. However, if a prediction for the current dependence of  $\lambda$  due to TRSB nonlinearities is developed, it can be compared to the analysis presented in this chapter to quantitatively address the responsible nonlinearity.

## CHAPTER 7

### SUMMARY AND FUTURE WORK

#### 7.1 Summary

Our work started with the development of the first scanned-probe magnetic near-field microwave microscope. This microscope was used to image the local permeability of different materials and the variation of the ferromagnetic-resonant field in a CMR material. Descending from the permeability imaging near-field microwave microscope, our nonlinear near-field microwave microscope has shown its capability of spatially identifying local nonlinear sources via measurement of the local harmonic generation from the YBCO bi-crystal grain boundary at  $\sim 60\text{K}$ . Locally enhanced second and third harmonic signals are observed near the grain boundary, and the magnitudes and spatial distributions of  $P_{2f}$  and  $P_{3f}$  are well modeled by the Extended Resistively Shunted Josephson (ERSJ) array model. The observed  $P_{2f}$  is attributed to the vortex dynamics driven by the microwave signal along the grain boundary. The ERSJ model simulated by WRSpice<sup>®</sup> demonstrates how the vortices/anti-vortices are generated and move along the grain boundary. These result in a time asymmetric magnetic field configuration along the boundary during a single RF cycle, and lead to the observed  $P_{2f}$  signal.

I further employed this microscope to study the doping-dependent nonlinearities in the under-doped high- $T_c$  superconductors (HTSC). The samples I studied are YBCO thin films deposited on NGO and STO substrates using the PLD technique. The oxygen deficiency of the samples was adjusted later by Ben Palmer [90] using his re-annealing apparatus. To quantitatively address the nonlinear mechanisms responsible for the measured harmonic signals near  $T_c$ , I introduce the scaling current density  $J_{NL}(x,T)$  and used Booth's algorithm to derive this quantity from our third harmonic data. By systematically analyzing  $P_{3f}$  data from variously doped YBCO thin films, I found a decreasing trend for  $J_{NL}(x,T)$  as the doping level is decreased. The  $P_{3f}$  signal near  $T_c$  is attributed to the intrinsic NLME of HTSC in my experiment, therefore the  $J_{NL}(x,T)$  is the de-pairing critical current density  $J_c(x,T)$ . The trend for  $J_c(x)$  found in my work is consistent with an independent work by Tallon *et al.* measuring the zero-temperature condensation energy as a function of doping [88, 89].

In addition to the third harmonic generation, I also observe significant second harmonic generation near  $T_c$  in under-doped YBCO thin films, which indicates the presence of a time-reversal symmetry breaking (TRSB) nonlinear mechanism. To quantitatively address such a nonlinear mechanism, I introduce a spontaneously flowing current  $J_{TRSB}$ , which manifests in the NLME as a  $J/J_{NL}'$  term, and makes the penetration depth linearly dependent on the external current. Extending Booth's algorithm to the linear-current-dependent term, I extract  $J_{NL}'$  and found an increasing trend of  $J_{NL}'$  as the doping level is

decreased. On the other hand,  $J_{TRSB}$ , whose extraction is solely dependent on knowledge of the film thickness, the input power, and the ratio of the measured  $P_{2f}$  and  $P_{3f}$ , shows a remarkable onset at  $T_c$ , and a trend of decreasing in magnitude as the doping level is decreased. This strongly suggests the presence of a doping dependent TRSB nonlinear mechanism below  $T_c$ , though the origin of this mechanism is not yet clear.

## 7.2 Future Work

Although my microscope has demonstrated its distinctive ability of locally measuring nonlinear properties, its sensitivity to nonlinearities, and spatial resolution, can be further improved.

As I mentioned in Chapter 1, I gave up driving the probe in a resonant mode so that I can have the capability of broadband measurements. However, by doing this, I also gave up the amplification of signals from the resonant mode, which is represented by the Q factor of the resonator. The typical Q factor of a coaxial transmission line resonator is about a few hundred, which means 20~30 dB of gain. I use two microwave amplifiers with total gain ~ 50 – 60 dB to compensate this trade-off. However, both amplifiers are broadband amplifiers, which amplify a lot of signals beyond the narrow bandwidths that I am interested and lift up the noise floor a lot (~ 40dB). Truly narrowband amplifiers are suggested to reduce the noise floor. More details about other limitations that this microscope faces, and suggested improvements are described below.



### 7.2.1 Sensitivity to the Nonlinearities

First and foremost, we would like to improve the sensitivity of this microscope to weaker nonlinear signals (i.e. signals from larger  $J_{NL}$  and  $J_{NL}'$ ). As demonstrated in Chapter 3, both  $P_{2f}$  and  $P_{3f}$  signals are proportional to  $\lambda^4$ , which is a diverging quantity near  $T_c$ . This means that my sensitivity to nonlinearities (as a function of temperature) is enhanced dramatically near  $T_c$ , but much lower at low temperatures. This is another reason why I observe a clear and healthy  $P_{3f}$  peak near  $T_c$ , in addition to the sample being more nonlinear near  $T_c$ . However, for lower temperatures (e.g.  $T < 0.9T_c$ ), we do not have this advantage of superior sensitivity. At lower temperatures, the largest  $J_{NL}$  I can measure is  $\sim 10^{10}$  A/m<sup>2</sup>, which is still much smaller than what is expected from the intrinsic NLME. Therefore, improving the sensitivity is the key to studying the intrinsic nonlinearities of superconductors at lower temperatures.

According to the arguments in Chapter 3, by reducing the film thickness, increasing the input frequency, and enlarging the figure the merit, the sensitivity of the microscope to nonlinearities can be greatly improved. However, the film thickness is more or less limited by the deposition technique and the tendency for film quality to degrade as the thickness decreases below about 100 nm. The input frequency is also limited by the frequency band defined by the existing low- and high-pass filters. These leave us with no other way to improve the sensitivity than by enlarging the figure of merit ( $\Gamma$ ,  $\Gamma'$ ) of the microscope.

From the calculations of  $\Gamma$  and  $\Gamma'$  by the HFSS software and my analytical model (Chapter 3), I find that both  $\Gamma$  and  $\Gamma'$  increase greatly upon reducing the loop size and bringing it closer to the sample. This suggests that by making the probe smaller and smaller, we will have better and better sensitivity. However, the smallest commercially available coaxial cable (with compatible SMA connector) is UT-20, whose outer conductor outer diameter is 0.020", which is not much smaller than the current probe size (0.034" outer diameter). In addition, at the time we made the loop probe, there was no non-magnetic UT-20 available commercially. Though it is available now, to make high quality connections between UT-20 coaxial cables and connectors is a very challenging task. Therefore, to push this approach to the limit, a lithographically patterned loop which can be as small as 15  $\mu\text{m}$  in diameter was suggested. I have designed such loops (shown in Fig. 7.1) for use with UT-34 (0.034" outer diameter) coaxial cable in my piezo-positioning low-temperature microwave microscope. HFSS calculations show that the microscope figure of merit increases substantially to  $\Gamma \sim 1.3 \times 10^6 \text{ A}^3/\text{m}^2$  for 1W input power. Dragos Mircea has fabricated these loops for his cryogenic microwave microscope. This approach will also greatly improve the spatial resolution, which is on the order of the loop diameter.

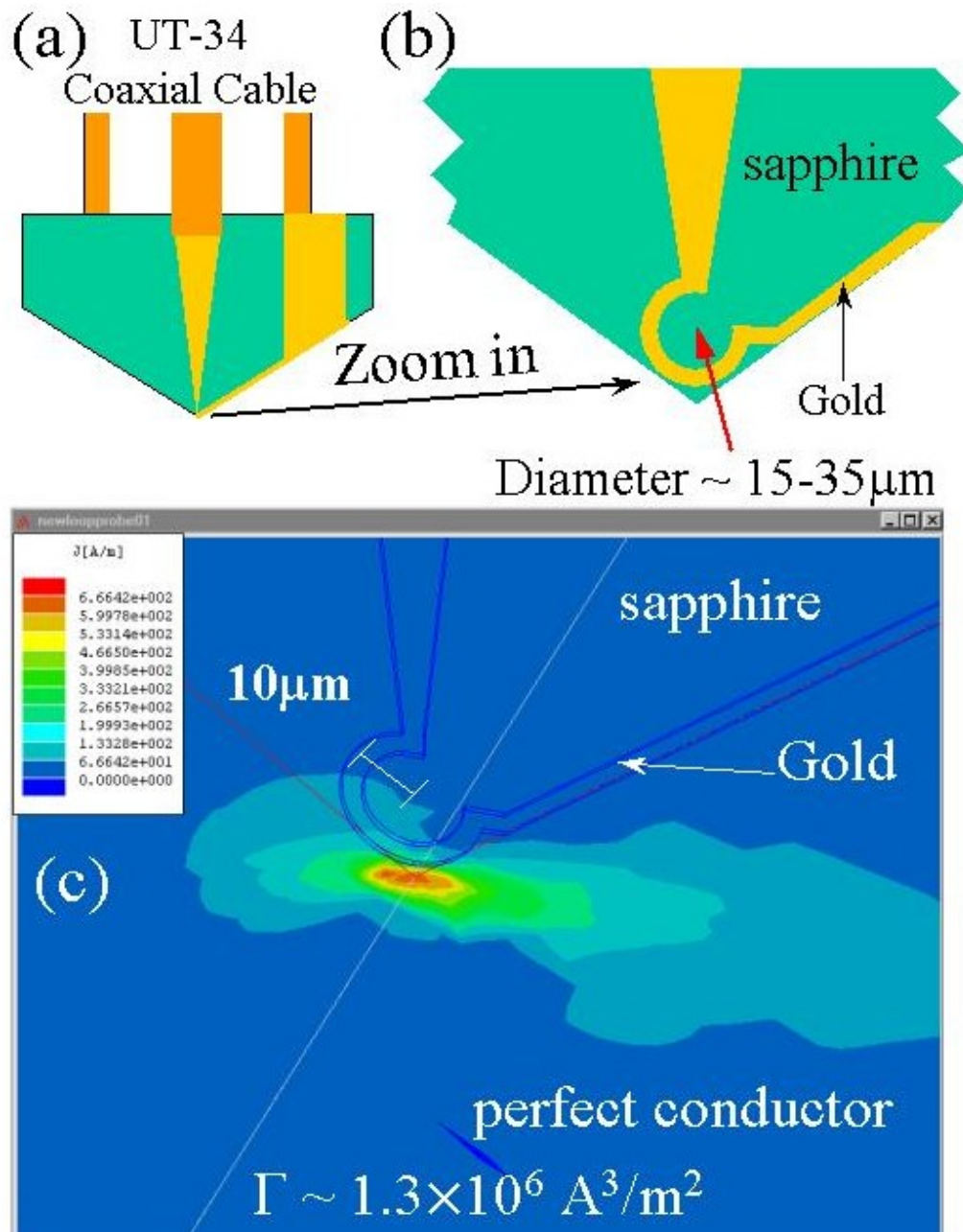


Fig. 7.1 (a) and (b) Schematic of a patterned loop probe on a sapphire substrate. (c) the surface current  $|K|$  distribution simulated by HFSS for a 20 μm diameter loop probe at 6.5 GHz.

### 7.2.2 Spatial Resolution

In the field of microscopy, better spatial resolution is always desired. The spatial resolution of our currently used microscope is not good enough for identifying much finer structural defects or impurities in HTSC thin films, which are on the order of a nano-meter. Although the spatial resolution of the current microscope can be improved to the order of 10  $\mu\text{m}$  as mentioned previously, even much better spatial resolution is desired.

Usually, such ultra-high spatial resolution scanning microscopy is achieved by using tunneling mechanisms (e.g. Scanning Tunneling Microscopy, or STM) or force-controlling mechanisms (e.g. Atomic Force Microscopy, AFM, and Magnetic Force Microscopy, MFM). I have attempted to combine the nonlinear near-field microscope with the tunneling mechanism, which controls the tip/sample separation through the feedback on the tunneling current. Due to the extremely weak coupling between the probe and sample, I have to apply relatively high microwave power ( $\sim +15$  dBm) to observe any harmonic generation. However, we found that by applying such high power microwave signals through the tunneling barrier (which is itself a nonlinear circuit element), we introduce significant amounts of rectified currents, which add to the tunneling current, and interfere with the mechanism controlling the probe/sample distance via the tunneling current. I tried to pulse the input microwave signals (as low as 10% duty cycle). The rectified current is reduced (less tip-withdraw), but still severe enough, and the nonlinear signals are smaller. I show in Fig. 7.2 how the tip withdraws as a function of the input microwave power (continuous

wave signals). In addition, I note that the color of the sample surface changes locally under such high input microwave power, and indicates some unknown contamination caused probably by local heating. Therefore, the technical challenge here is to take advantage of the very sensitive distance control mechanism of STM (by applying low enough input microwave power  $< -15$  dBm) without losing the sensitivity to the nonlinear signals.

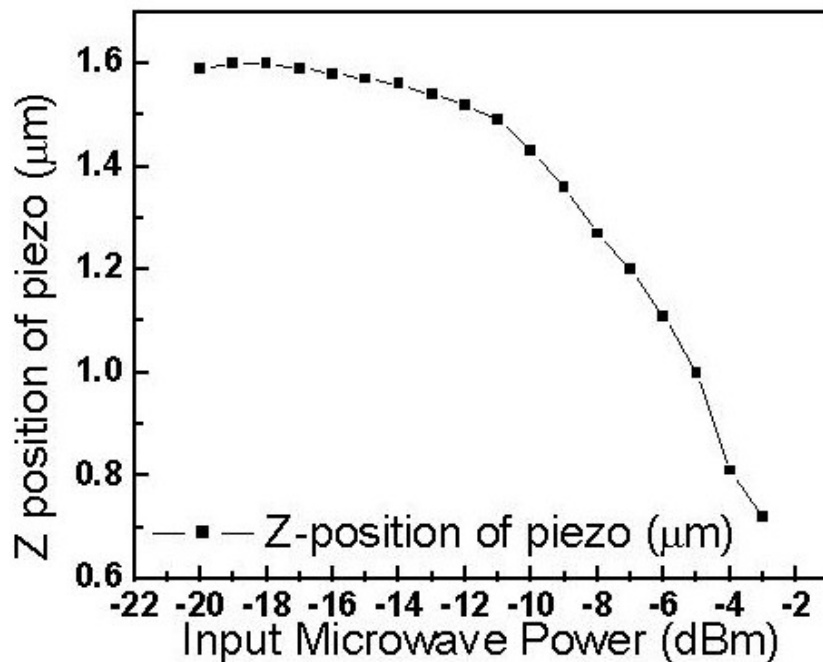


Fig. 7.2 The extension of z-piezo as a function of input microwave power taken with an STM microwave microscope. Smaller numbers in z-position means that the tip is withdrawing farther away from the sample.

To achieve this goal, resonant techniques are suggested to amplify the desired harmonic signals while the input microwave power is limited to  $< -15$  dBm. I designed and built a re-entrant microwave cavity which has resonant modes around 14 GHz and 19 GHz with

different Q factors and field configurations as shown in Fig. 7.3. By applying microwave signal through the STM tunnel junction at one half or one third of the resonant frequency, the second or third harmonic signal is amplified by the Q factor, and picked by a magnetic loop probe. We also note that some of the resonant modes have electric fields concentrated at the end of the tip, and some have magnetic fields. Therefore, we can sensitively detect through either electric or magnetic coupling to the sample by choosing the appropriate mode.

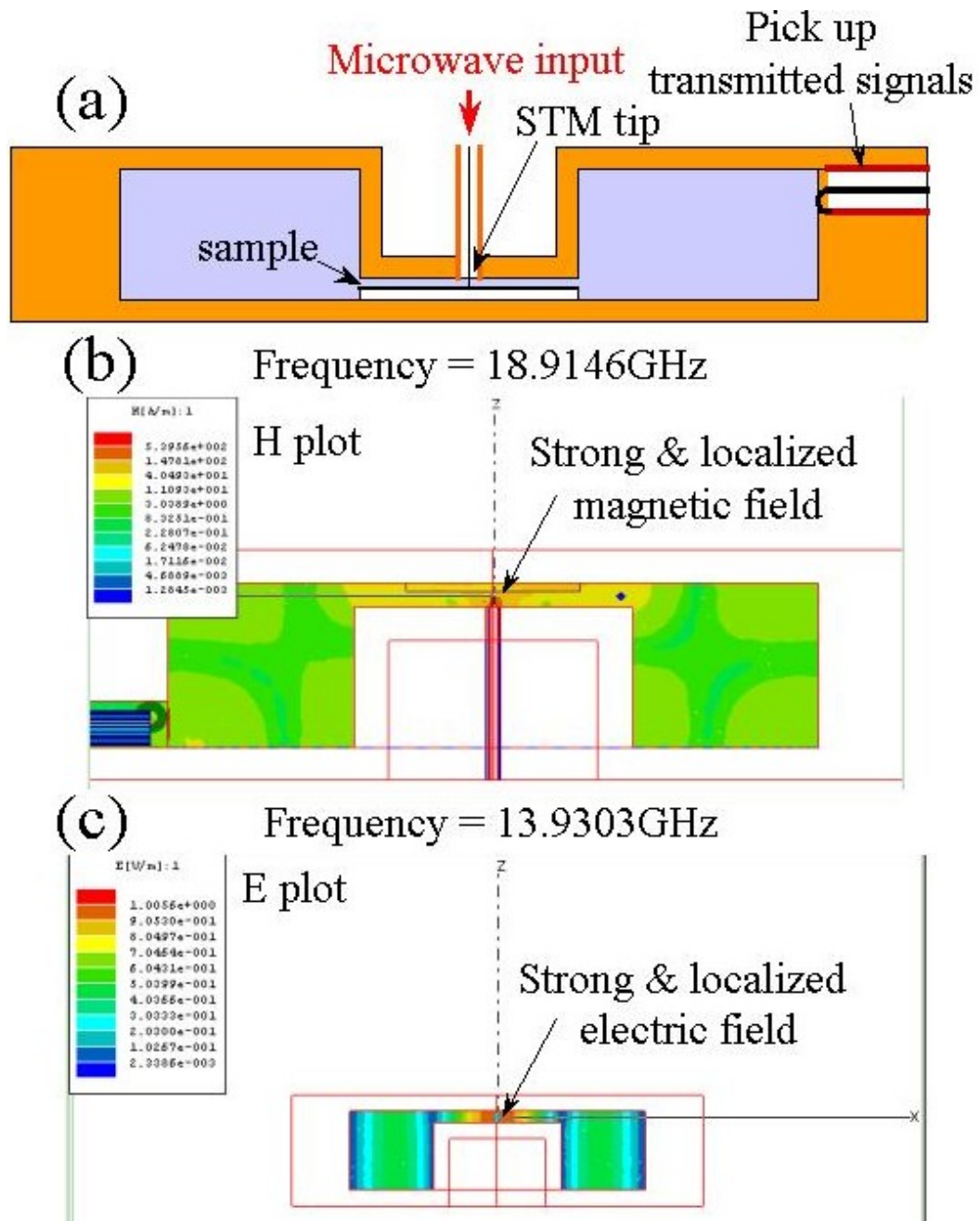


Fig. 7.3 Schematic of the re-entrant cavity. On the bottom are the field configurations at resonant modes  $\sim 14$  and  $19$  GHz, simulated by HFSS. Either electric or magnetic fields are concentrated in the small volume near the tip in each mode.

Shown in Fig. 7.4 is an STM topography image of a 30° mis-orientated YBCO bi-crystal grain boundary taken without inference from microwave signals at room temperature. The sample is the one discussed in Chapter 4, and the islands in the figure are expected to be a-axis grains out-grown on a c-axis surface. Nonlinear responses are expected at the boundaries between the a-axis grains and the c-axis film surface. Therefore, as long as high sensitivity can be maintained via the resonant technique at low input microwave powers, we expect to be able to measure the local nonlinear response at ultra-high spatial resolution, and correlate the nonlinear sources with the topographic features. The spatial resolution perhaps will be as good as that of STM, which is on the order of 1 nm.[9]



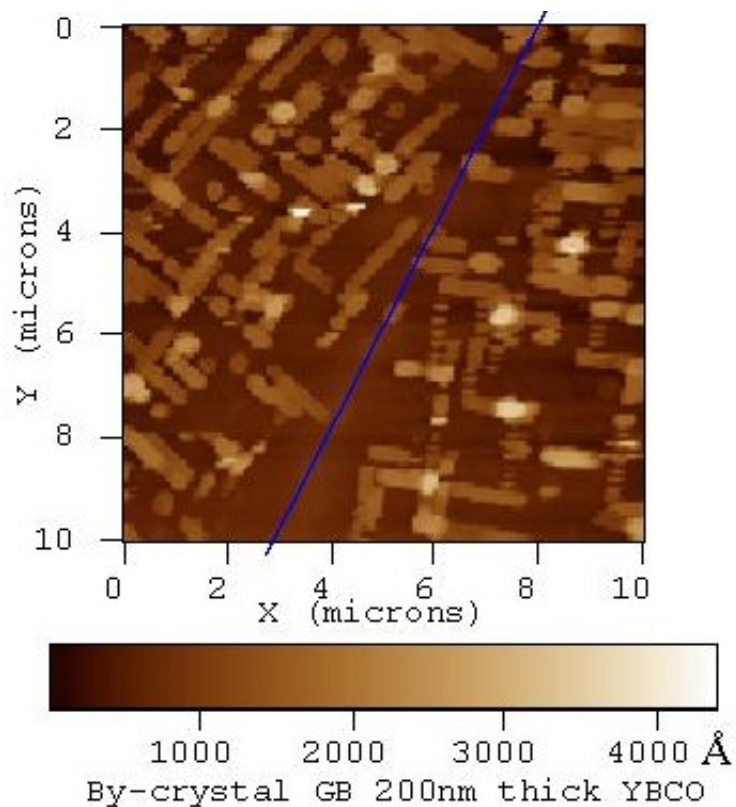


Fig. 7.4 STM topography image of a 200nm thick c-axis YBCO film on a STO 30° mis-oriented bi-crystal substrate. The blue line roughly marks the bi-crystal grain boundary. Topographic features are possibly a-axis grains, which rotate by 30° across the grain boundary.

In addition, I have been able to measure the  $P_{2f}$  and  $P_{3f}$  via the analog output on the spectrum analyzer as shown in Fig. 7.5. This allows me to combine the local harmonic measurement with the electronics controlling the STM tunneling and data acquisition process, so that the images of the topography,  $P_{2f}$  and  $P_{3f}$  can be simultaneously taken. Although the topography data is not relevant at this moment because the STM tip withdraws due to the rectified currents, this data shows that we can simultaneously take

harmonic data and STM images. Therefore, by implementing the suggested modification discussed above, I believe this microscope has great potential in locally determine the nonlinear sources on the nano-meter scale.

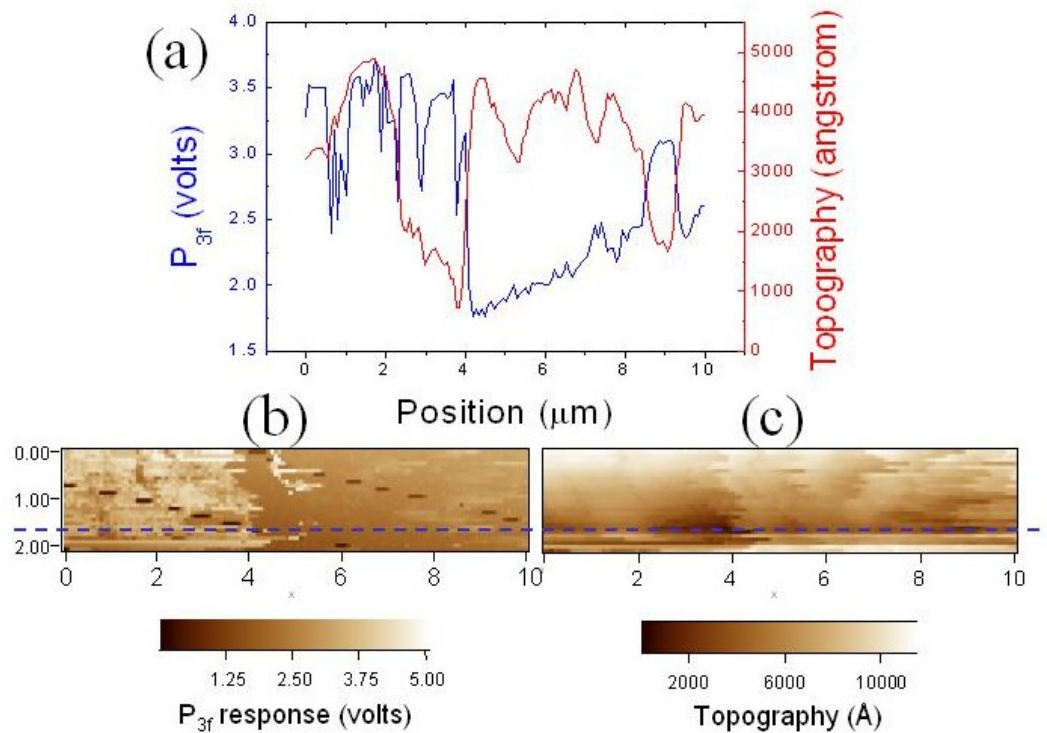


Fig. 7.5 Simultaneously taken harmonic data with STM imaging. (b) is the  $P_{3f}$  data taken while taking the STM image of a Tl2212 film in (c) at  $95\text{K} < T_c$  ( $\sim 105\text{K}$ ). (a) shows the comparison between the  $P_{3f}$  data and the topography along the blue dashed line in (b) and (c). The input microwave frequency is  $\sim 6.5$  GHz.

### 7.3 Conclusion

Our nonlinear near-field microwave microscope has proven to be a promising tool to measure the local nonlinearities of HTSC. By improving the sensitivity, it may prove very

useful in studying and deepening our understanding of the fundamental physics of HTSC (e.g. low temperature NLME and the ABS nonlinearity in d-wave superconductors). By improving the spatial resolution to the order of  $\sim 1$  nm, it may prove useful in identifying and characterizing the properties of the extrinsic nonlinearity due to structural defects or impurities.

## APPENDIX A

### FOURIER TRANSFORMS USED IN DATA ANALYSIS AND MODEL CALCULATIONS

#### A.1 Data Analysis – AC Circuit with a Nonlinear Inductor

The problem assumes an AC current source connected to a nonlinear (current-dependent) inductor. The details of this problem are described in Chapter 3. In the more general case, which is to have both the linear and quadratic current dependence in the inductor, the equation describing this circuit becomes,

$$V(t) = L \frac{dI(t)}{dt} = L_0 \frac{dI(t)}{dt} + \Delta L' I(t) \frac{dI(t)}{dt} + \Delta L I(t)^2 \frac{dI(t)}{dt}, \quad (\text{A.1})$$

where  $L = L_0 + \Delta L' I(t) + \Delta L I(t)^2$  is the current-dependent nonlinear inductor,  $V(t)$  is the voltage across the inductor, and the driving current  $I(t) = I_0 \sin(\omega t)$ . Substituting the function of  $I(t)$  into Eq. A.1, we have

$$\begin{aligned} V(t) &= \left( L_0 + \Delta L' I_0 \sin(\omega t) + \Delta L I_0^2 \sin^2(\omega t) \right) I_0 \omega \cos(\omega t) \\ &= \omega I_0 \left( L_0 \cos(\omega t) + \Delta L' I_0 \sin(\omega t) \cos(\omega t) + \Delta L I_0^2 \sin^2(\omega t) \cos(\omega t) \right) \end{aligned} \quad (\text{A.2})$$

Because of the nonlinear inductor,  $V(t)$  contains higher harmonic terms, and can be expressed as

$$V(t) = \sum_{n=1}^3 (V_{nf,a} \text{Sin}(n\omega t) + V_{nf,b} \text{Cos}(n\omega t)), \quad (\text{A.3})$$

where  $V_{nf,a}$  and  $V_{nf,b}$  are the coefficients of n-th order in-phase (sin) and out-of-phase (cos) terms. To obtain these coefficients, Fourier Transforms are used:

$$V_{nf,a} = \frac{2}{T} \int_0^T V(t) \text{Sin}(n\omega t) dt$$

$$V_{nf,b} = \frac{2}{T} \int_0^T V(t) \text{Cos}(n\omega t) dt. \quad (\text{A.4})$$

The calculated coefficients are listed in Table A.1.

Table A.1 Fourier coefficients in Eq. A.3 calculated via Eq. A.4.

	n = 1	n = 2	n = 3
$V_{nf,a}$	0	$\omega \Delta L' I_0^2 / 2$	0
$V_{nf,b}$	$\omega L_0 I_0 + (\omega \Delta L I_0^3 / 4)$	0	$-\omega \Delta L I_0^3 / 4$

## A.2 Model Calculation – Extracting Harmonics from Numerical Simulations

In Chapter 4, I describe two models to understand the harmonic generation from the YBCO bi-crystal grain boundary. One is to use Mathematica™ to solve the circuit of an AC current source driving a resistively shunted Josephson junction. The equation governing this circuit is

$$I_0 \text{Sin}(\omega t) = I_c \text{Sin} \Delta \gamma(t) + \frac{\Phi_0}{2\pi R} \frac{d\Delta \gamma(t)}{dt}, \quad (\text{A.5})$$

where  $I_0 \text{Sin}(\omega t)$  is the driving current,  $\Phi_0$  is the flux quantum,  $R$  is the shunted resistance,  $I_c$  is the critical current of the Josephson junction, and  $\Delta \gamma$  is the gauge invariant phase difference across the junction. Since what we measure is the potential difference generated on the sample, the voltage across the junction, which is proportional to the derivative of  $\Delta \gamma$ , is the desired quantity:

$$V(t) = \frac{\Phi_0}{2\pi} \frac{d\Delta \gamma(t)}{dt}. \quad (\text{A.6})$$

$V(t)$  contains higher order harmonic terms, and can be expanded as

$$V(t) = \sum_{n=0}^{\infty} (V_{1+2n f, a} \text{Sin}((1+2n)\omega t) + V_{1+2n f, b} \text{Cos}((1+2n)\omega t)). \quad (\text{A.7})$$

It is noted that  $V(t)$  only contains odd order harmonics. This is because Eq. A.5 describes a single Josephson junction, which preserves the Time-Reversal Symmetry [44].

Since  $V(t)$  is obtained by numerically solving Eq. A.5 with Mathematica™, there is no analytical form for the coefficients in Eq. A.7. Additionally, Mathematica™ has difficulty performing the Fourier Transforms in Eq. A.4 numerically due to the oscillating nature of the simulated results. Therefore, I perform the Fourier Transforms by summations instead of integration:

$$\begin{aligned}
V_{n f, a} &= \frac{2}{T} \sum_{m=0}^{\frac{T}{\Delta t}-1} V(m\Delta t) \text{Sin}(n\omega \cdot m\Delta t) \Delta t \\
V_{n f, b} &= \frac{2}{T} \sum_{m=0}^{\frac{T}{\Delta t}-1} V(m\Delta t) \text{Cos}(n\omega \cdot m\Delta t) \Delta t,
\end{aligned} \tag{A.8}$$

where  $\Delta t$  is the time step in the summation, which determines how close the summation comes to the integral. In most of my calculations, I use  $\Delta t = T/1000$ , which is a compromise between the time required for calculation and the accuracy of the calculation. The second and third harmonic generations from a Josephson junction simulated by Mathematica™ are calculated using Eq. A.8, and  $P_{2f} = (V_{2f,a}^2 + V_{2f,b}^2)/2Z_0$  and  $P_{3f} = (V_{3f,a}^2 + V_{3f,b}^2)/2Z_0$ . Of course, the probe/sample coupling, the attenuation and amplification through the coaxial transmission line system are also included in the calculation.

Another model used in Chapter 4 is the Extended Resistively Shunted Josephson junction model simulated numerically by WRSpice™. Details of how to use WRSpice™ can be found in Appendix B. An inductively coupling Josephson junction array is built in WRSpice™ for simulation, and WRSpice™ can calculate and output the potential difference across each junction. For the same reason mentioned previously, the coefficients of higher order terms in the Fourier expansion are extracted numerically using Eq. A.8.

## APPENDIX B

### HOW TO USE WRSPICE<sup>®</sup> SOFTWARE?

#### B.1 Introduction to WRSpice<sup>®</sup> Simulations of Extended Josephson Junctions

WRSpice<sup>®</sup> is a program developed by Steve Whiteley based on Spice3, which was developed in Berkeley, with additional models for Josephson junctions based on sine-Gordon equation. It is designed to simulate circuits with superconducting devices made of Josephson junctions, for instance, Superconducting Quantum Interference Devices (SQUID). Most conventional devices, for example, resistors, inductors, capacitors, current and voltage sources, and some other semi-conductor devices are also available in WRSpice<sup>®</sup>, though it's not as extensive as in the most advanced conventional Spice program. WRSpice<sup>®</sup> can perform different types of simulations. The one that I used in my work is "transient analysis", which is a time-based analysis, and simulates the circuit as it runs in real time. Another analysis called "frequency analysis", which simulates a circuit as frequency is varying, is also available. It is worth noting that WRSpice<sup>®</sup> alone does not have schematic design capability, though it is capable of plotting and text editing. To graphically enter the circuit schematics, another program, Xic<sup>®</sup>, is required to work with WRSpice<sup>®</sup>. However, in my work, I didn't use Xic<sup>®</sup> at all. This is because in my simulations I need to vary a huge amount of variables for each simulation in a systematic



way, but the batch mode capability in Xic<sup>®</sup> is very limited, and not user-friendly. As a result, it is much easier to work in WRSpice<sup>®</sup>, which has only a text-editing interface. WRSpice<sup>®</sup> is under continuous development by Steve Whiteley, and the updates are obtained on-line. It was originally developed in the UNIX environment, and the version we have has been modified for Windows systems. We are informed by Steve Whiteley that the NT based Windows system is preferred because of its better ability in managing memory usage. Since the circuits I simulate are very large, I noticed that WRSpice<sup>®</sup> is a very resource-demanding program; hence memories (both physical and virtual) and speed of the computer become crucial to its performance. For detailed information about this program, including WRSpice<sup>®</sup> and Xic<sup>®</sup>, manuals for each of them are available in the lab. There is also on-line help available, which may be helpful at times. In the rest of this section, I explain in detail how I use this program to simulate my model circuits. It should serve as a good start for people, who are new to this program.

## B.2 The Circuit Script File

All files used in WRSpice<sup>®</sup> are any plain text files. The “Circuit” file is denoted by “.cir”. Refer to “**ERSJ51.cir**” as an example as we proceed to construct such file.

- a) The **first** line in “**ERSJ51.cir**” is “\*title: the subcircuit of an ERSJ cell.” started with a “\*”. This line is usually the description of the circuit file, and will be printed on the screen while the file is called by WRSpice<sup>®</sup>. *This line is optional.*

b) Then we need to specify the special devices used in the circuit model. For the common devices, for example, voltage sources, current sources, resistors, capacitors, inductors, and so on, no specification is required. However, for Josephson junctions, we need to load the device model using the command line “**.model**”. For Josephson junctions we used, the device model is **jj1**, and there are device parameters associated with the model, which are specified through: “**jj(rtype=1, cct=1, icon=10m, vg=2.8m, delv=0.08m,+ icrit=.01m, r0=1, rn=20, cap=.1p)**”. The meaning of each parameters can be found in the device models in WRSpice manual. The important parameters are “*icrit (critical current, set to 10 $\mu$ A)*”, “*rn (shunt resistance 20 $\Omega$ )*”, and “*cap (shunt capacitance 0.1pF)*”.

c) One way of constructing a huge repetitive circuit array is to construct a simple sub-circuit, which acts as a user-defined *black box*. And then use this box in further circuit construction.

To build a sub-circuit, use the command line “**.subckt cell**” followed by the nodes of this “*black box*”. If there are any variables which we want to vary in this black box, we also declare them in this line with the default values, so that if there are no values assigned to the variables, the default values will be used. Construction of this “black box” is ended by the line “**.ends cell**”.

In our sub-circuit, a Josephson junction (**b1**), a resistor (**r1**), an AC current source (**i1**), and 2 inductors (**l1 & l2**) are used. The numbers are to label the devices, and

the “letters” are the convention in WRSpice<sup>®</sup> for calling each device. As the result of this construction, there are 5 nodes for this “*black box*”, including 4 nodes for physical devices, and 1 node for the phase difference across the Josephson junction. To extract information of the phase difference of each junction, this phase node must have different names of phase (e.g. phase1, phase2, etc) for each sub-circuit. Since in ERSJ51.cir, all phase nodes are given the same name, therefore, the phase information is not available. However, all other information, for instance, the voltage differences across devices and currents flowing through devices, are unaffected. Therefore, only integration of the voltage differences across the junction over time,  $\Delta\gamma(t) = \frac{2\pi}{\Phi_0} \int_0^t V(t') dt'$ , is needed to recover the phase information without the information from the phase nodes.

- d) Then a command line “.tran .5p 25n” is used to specify the type of analysis, which is “transient analysis” in this case. This is a “time” based analysis, which calculates variables as function of time. The analysis is performed for the time period from t=0s to t=25ns with time step  $\Delta t=0.5ps$ . The number of data points, which is  $25ns/0.5ps=50000$  in this case, determines the resulted data size of the simulation.
- e) The rest of the circuit construction is straightforward. To call the sub-circuit, we use the “X” notation for the sub-circuit, and “cell” following the node assignment. The

assignment of the variables in the sub-circuit is at the end of the line (i.e. “ival” in this case).

- f) The identical circuit can also be constructed without the sub-circuit. This actually provides better accessibility for measuring the voltages or currents of each device. For example, in “**curersj51.cir**”, no sub-circuit is used, and each device is shown in the circuit construction script. In this way, a 0voltage voltage source can be assigned to any device for measuring the current of that device, which is a typical way of measuring currents in WRSpice<sup>®</sup>.

### B.3 The Operational Script File

The Circuit Script file is a description of circuit diagram and type of analysis for WRSpice<sup>®</sup> to simulate. The Operational Script is what really carried out the simulation. Since what we want WRSpice<sup>®</sup> to do is simple, this script is very simple too.

#### B.3.1 The Core Operational Script

It starts with a line “**.control**” indicating this is an Operational script, and the second line is “**source filepath/filename**”, calling for the Circuit Script file. Up to this point, the Circuit Script file is loaded to the WRSpice<sup>®</sup>, and it knows what and how to analysis. The command “**run**” is to start the simulation. If you want to do something simple after the simulation, you can also add other command lines after the “**run**”. But usually I close this Script file here with the command line “**.endc**”.

Without additional specification, WRSpice, by default, temporarily records all voltages information, and all currents of voltage sources, which can be plotted or saved later.

### B.3.2 The Plotting/Saving Script

Plotting is also an operation of WRSpice<sup>®</sup>, so this file also starts with “**.control**”, and ends with “**.endc**”.

The “**body**” of this script is simply “**plot .....**”. If we are interested in the current of device ***b1***, we put a *0volt voltage source v1* in series with ***b1***, and plot the current of the voltage source by “**plot i(v1)**”. If we are interested in the voltage across device ***r1*** which connects to nodes ***1*** and ***2***, the command line is simply “**plot v(1)-v(2)**”. To save the plotted data, simply click on “save” command on the side of the plotting window, and enter the filepath and filename in the dialog box followed by pressing “enter”.

Saving data is similar to plotting. With the same structure started with “**.control**” and ended with “**.endc**”, the body is simply “**write variable/or calculated numbers filepath/filename**”.

### B.3.3 How to Operate WRSpice<sup>®</sup>

When WRSpice is started, there will be 2 windows prompt out. One is small and with tool bar on top like normal windows program (setting window), the other is the command line window like the MSDOS prompt window (command window).

a) Define the data size

As mentioned above, the data size is determined by the “time” and “time step” in the transient analysis.

Therefore, before using the WRSpice<sup>®</sup>, it is suggested to set the virtual memory of the machine to the maximum (4GB). When WRSpice<sup>®</sup> is started, before running any script, adjust the “**max data size**” setting in WRSpice<sup>®</sup> to 4GB as well. This can be done by clicking the “**tools**” on the tool bar of the setting window and selecting “**Sim Def**” in the drop-down list. Then a windows will show up with the default setting of “**max data size**” of 32MB (shown as 32000 in the text box). Change this number to 4000000 (i.e. 4GB), and check the “**set**” check box. Then click on “**dismiss**” bottom to close this window. Now the “**max data size**” should have been set to 4GB.

b) The way that WRSpice calls for a script file is to use “source” command. To start the simulation, type in “**source filepath/filename**”, where the filename is the Core Operational Script file, in the command window. When the simulation is finished, then type in “**source filepath/filename**”, where the filename is the Plotting Script file, to plot the desired data, and use the “**save**” bottom on the plot window to save the data to desired files.

Due the limitation of the physical and virtual memory, it is suggested not to plot more than **25** plots at once. Save the data immediately after plotting them. Close the

plot window, which is saved immediately after saving it, by clicking “**dismiss**”.

However, if the window position has been moved on the screen, **DO NOT** close the window after saving the data, or it may freeze the WRSpice program. Just leave the window on the screen.

#### B.3.4 About System Resources

Since my WRSpice<sup>®</sup> simulation consumes tremendous system resources, it is worth noting that plotting certainly consumes more memory. If it is not necessary to view how the data looks before saving, it is suggested saving the data directly via “*Saving Script*”. An example can be given to see how much more efficient it is via using “*Saving Script*”. Since I have 1000 junctions in my circuit array, when I want to save information of each junction separately, I have to perform “**plotting + saving**” or “**saving**” 1000 times. If I do it via the “*Plotting Script*” then saving the data via the bottom on the plot, with extreme care as mentioned above, I can save at most ~120 files in one simulation. Then the WRSpice<sup>®</sup> is frozen, and needed to restart and re-simulate again. If I do it via the “*Saving Script*”, I can save more than 600 files at one time, before the virtual memory runs out, and I have to restart the program and re-simulate again.

This comparison clearly shows that “*Saving Script*” is much more efficient than “*Plotting Script*” if viewing the plot of data is not necessary before saving it.

If repeated simulations of different circuit files are to be performed, the command “**free**” is useful in erasing the loaded circuit and all recorded data, including plots, from the virtual

memory so that it can be used for next simulation. An example of using this command can be found in the file “*runall.cir*”.



## REFERENCES

- 
- [1] A. B. Pippard, “**The surface impedance of superconductors and normal metals at high frequencies: I. Resistance of superconducting tin and mercury at 1200 Mcyc./sec.,**” Proc. Roy. Soc. A **191**, 370-384, 1947.
- [2] E. A. Syngé, “**A suggested method for extending microscopic resolution into the ultra-microscopic region,**” Phil. Mag. C **6**, 356-362, 1928.
- [3] Zdenek Frait, “**The use of high frequency modulation in studying ferromagnetic resonance,**” Czech. J. Phys. **9**, 403-404, 1959; Z. Frait, V. Kambersky, Z. Malek, and M. Ondris, “**Local variations of uniaxial anisotropy in thin films,**” Czech. J. Phys. **B10**, 616-617, 1960.
- [4] R. F. Soohoo, “**A Microwave Magnetic Microscope,**” J. Appl. Phys. **33**, 1276-1277, 1962.
- [5] Steven M. Anlage, D. E. Steinhauer, B. J. Feenstra, C. P. Vlahacos, and F. C. Wellstood, in Proceeding of the NATO Advanced Study Institute on “**Microwave Superconductivity,**” Kluwer Academic Publisher, Norwell, MA, 2001, 239-269.
- [6] Sheng-Chiang Lee, C. P. Vlahacos, B. J. Feenstra, Andrew Schwartz, D. E. Steinhauer, F. C. Wellstood, and Steven M. Anlage, “**Magnetic Permeability Imaging of Metals**”

- 
- with a Scanning Near-Field Microwave Microscope,”** Appl. Phys. Lett. **77**, 4404-4406, 2000.
- [7] Sheng-Chiang Lee and Steven M. Anlage, **“Spatially-Resolved Nonlinearity Measurements of  $\text{YBa}_2\text{Cu}_3\text{O}_{7-\delta}$  Bicrystal Grain Boundary,”** Appl. Phys. Lett. **82**, 1893-1895, 2003.
- [8] R. C. Black, F. C. Wellstood, E. Datsker, A. H. Miklich, D. T. Nemeth, D. Koelle, F. Ludwig, and J. Clarke, **“Microwave microscopy using a superconducting quantum interference device,”** Appl. Phys. Lett. **66**, 99-101, 1995.
- [9] Atif Imtiaz and Steven M. Anlage, **“A novel STM-assisted microwave microscope with capacitance and loss imaging capability,”** Ultramicroscopy **94**, 209-216, 2003.
- [10] V. Korenivski, R. B. van Dover, P. M. Mankiewich, Z.-X. Ma, A. J. Becker, P. A. Polakos, and V. J. Fratello, **“A Method to Measure the Complex Permeability of Thin Films at Ultra High Frequencies,”** IEEE Trans. Magn. **32**, 4905-4907, 1996.
- [11] Y. Gao and I. Wolff, **“A New Miniature Magnetic Field Probe for Measuring Three-Dimensional Fields in Planar High-Frequency Circuits,”** IEEE Trans. Microwave Theory Tech. **44**, 911-918, 1996.
- [12] V. Agrawal, P. Neuzil, and D. W. van der Weide, **“A Microfabricated Tip for Simultaneous Acquisition of Sample Topography and High-Frequency Magnetic Field,”** Appl. Phys. Lett. **71**, 2343-2345, 1997.

- 
- [13] M. Ikeya, M. Furusawa, and M. Kasuya, “**Near-field scanning electron spin resonance microscopy,**” *Scanning Microscopy* **4**, 245-248, 1990.
- [14] Z. Zhang, P. C. Hammel, M. Midzor, M. L. Roukes, and J. R. Childress, “**Ferromagnetic resonance force microscopy on microscopic cobalt single layer films,**” *Appl. Phys. Lett.* **73**, 2036-2038, 1998.
- [15] K. Wago, D. Botkin, C. S. Yannoni, and D. Rugar, “**Paramagnetic and ferromagnetic resonance imaging with a tip-on-cantilever magnetic resonance force microscope,**” *Appl. Phys. Lett.* **72**, 2757-2759, 1998.
- [16] S. E. Lofland, S. M. Bhagat, H. L. Ju, G. C. Xiong, T. Venkatesan, and R. L. Greene, “**Ferromagnetic resonance and magnetic homogeneity in a giant-magnetoresistance material  $\text{La}_{2/3}\text{Ba}_{1/3}\text{MnO}_3$ ,**” *Phys. Rev. B* **52**, 15058-15061, 1995.
- [17] Y. Martin and H. K. Wickramasinghe, “**Magnetic Imaging by “Force Microscopy” with 1000Å Resolution,**” *Appl. Phys. Lett.* **50**, 1455-1457, 1987.
- [18] S. Y. Yamamoto and S. Schultz, “**Scanning Magnetoresistance Microscopy,**” *Appl. Phys. Lett.* **69**, 3263-3265, 1996.
- [19] D. E. Steinhauer, C. P. Vlahacos, S. K. Dutta, B. J. Feenstra, F. C. Wellstood, and Steven M. Anlage, “**Quantitative Imaging of Sheet Resistance with a Scanning Near-Field Microwave Microscope,**” *Appl. Phys. Lett.* **72**, 861-863, 1998.

- 
- [20] D. E. Steinhauer, C. P. Vlahacos, C. Canedy, A. Stanishevski, J. Melngailis, R. Ramesh, F. C. Wellstood, and S. M. Anlage, “**Imaging of Microwave Permittivity, Tunability, and Damage Recovery in (Ba,Sr)TiO<sub>3</sub> Thin Films,**” Appl. Phys. Lett. **75**, 3180-3182, 1999.
- [21] D. E. Steinhauer, “**Quantitative Imaging of Sheet Resistance, Permittivity, and Ferroelectric Critical Phenomena with a Near-Field Scanning Microwave Microscope,**” Ph.D. Dissertation, University of Maryland, 2000.
- [22] C. P. Vlahacos, R. C. Black, S. M. Anlage, A. Amar, and F. C. Wellstood, “**Near-field Scanning Microwave Microscope with 100 nm Resolution,**” Appl. Phys. Lett. **69**, 3272-3274, 1996.
- [23] J. M. Jaycox and M. B. Ketchen, “**Planar Coupling Scheme for Ultra Low Noise DC SQUIDs,**” IEEE Trans. Magn. MAG-17, 400-403, 1981.
- [24] A. Schwartz, M. Scheffler, and S. M. Anlage, “**Determination of the Magnetization Scaling Exponent for Single-Crystal La<sub>0.8</sub>Sr<sub>0.2</sub>MnO<sub>3</sub> by Broadband Microwave Surface Impedance Measurements,**” Phys. Rev. B **61**, R870-873, 2000.
- [25] A. Schwartz, M. Scheffler, and S. M. Anlage, “**The Frequency, Temperature, and Magnetic Field Dependence of Ferromagnetic Resonance and Anti-resonance in La<sub>0.8</sub>Sr<sub>0.2</sub>MnO<sub>3</sub>,**” cond-mat/0010172.

- 
- [26] Michael Tinkham, “*Introduction to Superconductivity*,” Singapore: McGraw-Hill, 1996.
- [27] Terry P. Orlando and Kevin A. Delin, “*Foundations of Applied Superconductivity*,” Addison-Wesley, 1991.
- [28] J. Gittleman, B. Rosenblum, T. E. Seidel, and A. W. Wicklund, “**Nonlinear Reactance of Superconducting Films**,” Phys. Rev. **137**, A527, 1965.
- [29] S. K. Yip and J. A. Sauls, “**Nonlinear Meissner Effect in CuO Superconductors**,” Phys. Rev. Lett. **69**, 2264, 1992.
- [30] D. Xu, S. K. Yip, and J. A. Sauls, “**Nonlinear Meissner Effect in Unconventional Superconductors**,” Phys. Rev. B **51**, 16233, 1995.
- [31] T. Dahm and D. J. Scalapino, “**Theory of Intermodulation in a Superconducting Microstrip Resonator**,” J. Appl. Phys. **81**, 2002, 1997.
- [32] T. Dahm and D. J. Scalapino, “**Nonlinear Current Response of a d-wave Superfluid**,” Phys. Rev. B **60**, 13125, 1999.
- [33] J. R. Cooper, “**An Empirical Pair-breaking Picture for the Non-linear Meissner Effect in d-wave Superconductors**,” cond-mat/0008270.
- [34] M. Spiewak, “**Magnetic field dependence of high-frequency penetration into a superconductor**,” Phys. Rev. Lett. **1**, 136-138, 1958.

- 
- [35] Y. V. Sharvin and V. F. Gantmakher, “**Dependence of the depth of penetration of the magnetic field in a superconductor on the magnetic field strength,**” Sov. Phys. JETP **12**, 866-872, 1961.
- [36] S. Sridhar and J. E. Mercereau, “**Non-equilibrium dynamics of superconducting quasiparticles,**” Phys. Rev. B **34**, 203-216, 1986.
- [37] T. Hanaguri, Y. Iino, A. Maeda, T. Fukase, “**Magnetic field dependence of the London penetration depth in Type-II superconductor  $V_3Si$ ,**” Physica C **246**, 223-227, 1995.
- [38] A. Maeda, T. Hanaguri, Y. Iino, S. Masuoka, Y. Kokata, J. Shimoyama, K. Kishio, H. Asaoka, Y. Matsushita, M. Hasegawa, H. Takei, “**Nonlinear Meissner Effect in Double Layered High- $T_c$  Cuprates Investigated by Measurement of the Penetration Depth,**” J. Phys. Soc. Japan **65**, 3638-33645, 1996.
- [39] S. Sridhar, D. H. Wu, and W. Kennedy, “**Temperature Dependence of Electrodynamic Properties of YBCO Crystals,**” Phys. Rev. Lett. **63**, 1873-1876, 1989.
- [40] A. Maeda, Y. Iino, T. Hanaguri, N. Motohira, K. Kishio, and T. Fukase, “**Magnetic field dependence of the London penetration depth of  $Bi_2Sr_2CaCu_2O_y$ ,**” Phys. Rev. Lett. **74**, 1202-1205, 1995.
- [41] A. Carrington, R. W. Giannetta, J. T. Kim, and J. Giapintzakis, “**Absence of nonlinear Meissner effect in  $YBa_2Cu_3O_{6.95}$ ,**” Phys. Rev. B **59**, R14173-14176, 1999.

- 
- [42] C. P. Bidinosti, W. N. Hardy, D. A. Bonn, and R. Liang, “**Measurements of the Magnetic Field Dependence of  $I$  in  $\text{YBa}_2\text{Cu}_3\text{O}_{6.95}$ : Results as a Function of Temperature and Field Orientation,**” *Phys. Rev. Lett.* **83**, 3277-3280, 1999.
- [43] K. Halterman, O. T. Valls, and I. Zutic, “**Reanalysis of the magnetic field dependence of the penetration depth: observation of the nonlinear Meissner effect,**” *Phys. Rev. B* **63**, 180405 (R), 2001.
- [44] J. McDonald and John R. Clem, “**Microwave response and surface impedance of weak links,**” *Phys. Rev. B* **56**, 14723-14732, 1997.
- [45] C. J. Lehner, D. E. Oates, Y. M. Habib, G. Dresselhaus, and M. S. Dresselhaus, “**Modeling the Microwave Impedance of High-Tc Long Josephson Junctions,**” *J. Supercond.* **12**, 363-375, 1999.
- [46] M.-R. Li, P. J. Hirschfeld, and P. Wolfle, “**Is the Nonlinear Meissner Effect Unobservable?**” *Phys. Rev. Lett.* **81**, 5640-5643, 1998.
- [47] I. Kosztin and A. J. Leggett, “**Nonlinear Effects on the Magnetic Penetration Depth in d-wave Superconductors,**” *Phys. Rev. Lett.* **79**, 135-138, 1997.
- [48] I. Ciccarello, C. Fazio, M. Guccione, and M. Li Vigni, “**Nonlinear Magnetization of YBCO Single Crystals Near  $T_c$ ,**” *Phys. Rev. B* **49**, 6280, 1994.

- 
- [49] Chia-Ren Hu, “**Midgap Surface States as a Novel Signature for  $d_{x_a^2-x_b^2}$ -wave Superconductivity,**” Phys. Rev. Lett. **72**, 1526, 1994.
- [50] M. Covington, M. Aprili, E. Paraoanu, and L. H. Greene, “**Observation of Surface-Induced Broken Time-Reversal Symmetry in  $\text{YBa}_2\text{Cu}_3\text{O}_7$  Tunnel Junctions,**” Phys. Rev. Lett. **79**, 277, 1997.
- [51] L. H. Greene, M. Aprili, M. Covington, E. Badica, D. E. Pugel, H. Aubin, Y.-M. Xia, M. B. Salamon, Sha Jain, and D. G. Hinks, “**Spectroscopy of the Andreev Bound State of High-Temperature Superconductors: Measurements of Quasiparticle Scattering, Anisotropy, and Broken Time-Reversal Symmetry,**” Physica C **341-348**, 1633, 2000.
- [52] L. H. Greene, P. Hentges, H. Aubin, M. Aprili, E. Badica, M. Covington, M. M. Pafford, G. Westwood, W. G. Klemperer, S. Jian, D. G. Hinks, “**Planar Tunneling Spectroscopy of High-Temperature Superconductors: Andreev Bound States and Broken Symmetries,**” Physica C **387**, 162, 2003.
- [53] R. Krupke and G. Deutscher, “**Anisotropy Magnetic Field Dependence of the Zero-Bias Anomaly on In-Plane Oriented  $[110] \text{Y}_1\text{Ba}_2\text{Cu}_3\text{O}_{7-x}/\text{In}$  Tunneling Junctions,**” Phys. Rev. Lett. **83**, 4634-4637, 1999.
- [54] Y. Dagan, A. Kohen, G. Deutscher, and A. Revcolevschi, “**Absence of Andreev reflections and Andreev bound states above the critical temperature,**” Phys. Rev. B **61**, 7012-7016, 2000.



- 
- [55] Y. Dagan and G. Deutscher, “**Thickness independence of field-induced time-reversal symmetry breaking in  $\text{YBa}_2\text{Cu}_3\text{O}_{7-\delta}$  thin films,**” Phys. Rev. B **64**, 092509, 2001.
- [56] Y. Dagan and G. Deutscher, “**Doping and Magnetic Field Dependence of In-Plane Tunneling into  $\text{YBa}_2\text{Cu}_3\text{O}_{7-x}$ : Possible Evidence for the Existence of a Quantum Critical Points,**” Phys. Rev. Lett. **87**, 177004, 2001.
- [57] J. Y. T. Wei, N.-C. Yeh, D. F. Garrigus, and M. Strasik, “**Directional Tunneling and Andreev Reflection on  $\text{YBa}_2\text{Cu}_3\text{O}_{7-\delta}$  Single Crystals: Predominance of d-wave Pairing Symmetry Verified with the Generalized Blonder, Tinkham, and Klapwijk Theory,**” Phys. Rev. Lett. **81**, 2542-2545, 1998.
- [58] Manfred Sigrist, “**Superconductivity with broken time-reversal symmetry,**” Physica B **280**, 154-158, 2000.
- [59] J. Lesueur, ESPCI Paris, Presented at the Materials and Mechanisms of Superconductivity Conference, Rio de Janeiro, May, 2004.
- [60] Yu. Barash, M. S. Kalenkov, and J. Kurkijärvi, “**Low-Temperature Magnetic Penetration Depth in d-wave Superconductors: Zero-Energy Bound State and Impurity Effects,**” Phys. Rev. B **62**, 6665, 2000.

- 
- [61] A. Carrington, F. Manzano, R. Prozorov, R. W. Giannetta, N. Kameda, and T. Tamegai, “**Evidence for Surface Andreev Bound States in Cuprate Superconductors from Penetration Depth Measurements,**” *Phys. Rev. Lett.* **86**, 1074, 2001.
- [62] W. N. Hardy, D. A. Bonn, D. C. Morgan, Ruixing Liang, and Kuan Zhang, “**Precision Measurements of the Temperature Dependence of  $l$  in  $\text{YBa}_2\text{Cu}_3\text{O}_{6.95}$ : Strong Evidence for Nodes in the Gap Function,**” *Phys. Rev. Lett.* **70**, 3999, 1993.
- [63] Steven M. Anlage, Dong-Ho Wu, Jian Mao, Sining Mao, X. X. Xi, T. Venkatesan, J. L. Peng, and R. L. Greene, “**The Electrodynamics of  $\text{Nd}_{1.85}\text{Ce}_{0.15}\text{CuO}_{4-y}$ : Comparison with Nb and  $\text{YBa}_2\text{Cu}_3\text{O}_7$ ,**” *Phys. Rev. B* **50**, 523, 1994.
- [64] C. M. Varma, “**Proposal for an experiment to test a theory of high-temperature superconductors,**” *Phys. Rev. B* **61**, R3804-R3807, 2000.
- [65] A. Kaminski, S. Rosenkranz, H. M. Fretwell, J. C. Campuzano, Z. Li, H. Raffy, W. G. Cullen, H. You, C. G. Olson, C. M. Varma, and H. Höchst, “**Spontaneous breaking of time-reversal symmetry in the pseudogap state of a high- $T_c$  superconductors,**” *Nature* **416**, 610-613, 2002.
- [66] S. V. Borisenko, A. A. Kordyuk, A. Koitzsch, T. K. Kim, K. Nenkov, M. Knupfer, J. Fink, C. Grazioli, S. Turchini, and H. Berger, “**Circular dichroism in angle-resolved photoemission spectra of under- and overdoped Pb-Bi2212,**” *cond-mat/0305179*.

- 
- [67] M. E. Simon and C. M. Varma, “**Symmetry consideration for the detection of second-harmonic generation in cuprates in the pseudogap phase,**” *Phys. Rev. B* **67**, 054511, 2003.
- [68] Balam A. Wellemsen, K. E. Kihlstrom, T. Dahm, D. J. Scalapino, B. Gowe, D. A. Bonn, and W. N. Hardy, “**Microwave Loss and Intermodulation in TBCCO Thin Films,**” *Phys. Rev. B.* **58**, 6650-6654, 1998.
- [69] James C. Booth, J. A. Beall, D. A. Rudman, L. R. Vale, and R. H. Ono, “**Geometry Dependence of Nonlinear Effects in High Temperature Superconducting Transmission Lines at Microwave Frequencies,**” *J. Appl. Phys.* **86**, 1020-1027, 1999.
- [70] James C. Booth, Leila R. Vale, and Ronald H. Ono, “**On-Wafer Measurements of Nonlinear Effects in High Temperature Superconductors,**” *IEEE Trans. Appl. Supercond.* **11**, 1387-1391, 2001.
- [71] Nathan Bluzer and David K. Fork, “**Inductance of a Superconducting Corbino Ring,**” *IEEE Trans. Magn.* **28**, 2051-2055, 1992.
- [72] A.Yu. Aladyshkin, A. A. Andronov, E. E. Pestov, Yu. N. Nozdrin, V. V. Kurin, A. M. Cucolo, R. Monaco, and M. Boffa, “**Study of the nonlinear response of superconductors in the microwave band using a local technique,**” *Radiophysics and Quantum Electronics* **46**, 109-127, 2003.

- 
- [73] Carlos Collado, Jordi Mateu, and Juan M. O'Callaghan, "**Analysis and Simulation of the Effects of Distributed Nonlinearities in Microwave Superconducting Devices,**" submitted to IEEE Trans. Appl. Supercond., 2003.
- [74] J. Mateu, C. Collado, J. M. O'Callaghan, "**Comparison between nonlinear measurements in patterned and unpatterned thin films,**" unpublished manuscript.
- [75] Greg Ruchti, "**Electromagnetic Simulations with Ansoft High Frequency Structure Simulator and Ansoft Optimetrics,**" Senior Thesis, University of Maryland, 2003.
- [76] John David Jackson, "*Classical Electrodynamics,*" 3<sup>rd</sup> Edition, New York: Wiley, 1998.
- [77] P. P. Nguyen, D. E. Oates, G. Dresselhaus, and M. S. Dresselhaus, "**Nonlinear surface impedance for YBCO thin films: Measurements ad a coupled-grain model,**" Phys. Rev. B **48**, 6400, 1993.
- [78] D. E. Oates, P. P. Nguyen, Y. Habib, G. Dresselhaus, M. S. Dresselhaus, G. Koren, and E. Polturak, "**Microwave power dependence of YBCO thin-film Josephson edge junction,**" Appl. Phys. Lett. **68**, 705, 1996.
- [79] Jeffrey S. Herd, D. E. Oates, Hau Xin, and Stuard J. Berkowitz, "**Coupled-Grain/RSJ Series Array for Modeling of Nonlinear Microwave Surface Impedance of YBCO Thin Films,**" IEEE Trans. Appl. Supercond. **9**, 2117-2120, 1999.

- 
- [80] W. Hu, A. S. Thanawalla, B. J. Feenstra, F. C. Wellstood, and S. M. Anlage, “**Imaging of microwave intermodulation fields in a superconducting microstrip resonator,**” *Appl. Phys. Lett.* **75**, 2824-2826, 1999.
- [81] Evgeny E. Pestov, Yury N. Nozdrin, and Vladislav V. Kurin, “**Third-Order local nonlinear microwave response of YBCO and Nb thin films,**” *IEEE Trans. Appl. Supercond.* **11**, 131-134, 2001.
- [82] Sheng-Chiang Lee and Steven M. Anlage, “**Study of Local Nonlinear Properties Using a Near-Field Microwave Microscope,**” *IEEE Trans. Appl. Supercond.* **13**, 3594-3597, 2003.
- [83] D. E. Oates, Y. M. Habib, C. J. Lehner, L. R. Vale, R. H. Ono, G. Dresselhaus, and M. S. Dresselhaus, “**Measurement and Modeling of Microwave Impedance of High-T<sub>c</sub> Grain Boundaries,**” *IEEE Trans. Appl. Supercond.* **9**, 2446-2451, 1999.
- [84] Sojiphong Chatraphorn, “**Room-Temperature Magnetic Microscopy using a High-T<sub>c</sub> SQUID,**” Ph.D. Dissertation, University of Maryland, 2000.
- [85] E. Goldobin, A. M. Klushin, M. Siegel, and N. Klein, “**Long Josephson junction embedded into a planar resonator at microwave frequencies: Numerical simulation of fluxon dynamics,**” *J. Appl. Phys.* **92**, 3239-3250, 2002.
- [86] K. K. Likharev, “**Superconducting weak links,**” *Rev. Mod. Phys.* **51**, 101-159, 1979.

- 
- [87] Sudip Chakravarty, R. B. Laughlin, Dirk K. Morr, and Chetan Nayak, “**Hidden order in cuprates,**” Phys. Rev. B **63**, 094503, 2001.
- [88] J. W. Loram, K. A. Mirza, J. R. Cooper, and J. L. Tallon, “**Superconducting and Normal State Energy Gaps in  $Y_{0.8}Ca_{0.2}Ba_2Cu_3O_{7-\delta}$  from the Electronic Specific Heat,**” Physica C **282-287**, 1405-1406, 1997.
- [89] J. L. Luo, J. W. Loram, J. R. Cooper, and J. Tallon, “**Doping Dependence of Condensation Energy and Upper Critical Field in  $Y_{0.8}Ca_{0.2}Ba_2Cu_3O_{7-\delta}$  from Specific Heat Measurement,**” Physica C **341-348**, 1837-1840, 2000.
- [90] B. S. Palmer, “**Development and Applications of Scanning Probe Techniques: Scanning Eddy Current Dynamometer and Photoconductivity Studies of Underdoped YBCO,**” Ph.D. Dissertation, University of Maryland, 2003.
- [91] J. R. Waldram, D. M. Broun, D. C. Morgan, R. Ormeno, and A. Porch, “**Fluctuation effects in the microwave conductivity of cuprate superconductors,**” Phys. Rev. B **59**, 1528-1537, 1999.
- [92] C. Kusko, Z. Zhai, N. Hakim, R. S. Markiewicz, S. Sridhar, D. Colson, V. Viallet-Guillen, A. Forget, Yu. A. Nefyodov, M. R. Trunin, N. N. Kolesnikov, A. Maignan, A. Daignere, and A. Erb, “**Anomalous microwave conductivity due to collective transport in the pseudogap state of cuprate superconductors,**” Phys. Rev. B. **65**, 132501, 2002.

- 
- [93] John Martinis, presentation W32.08 at the APS March Meeting, Austin, Texas, 2003.
- [94] J. L. Tallon, C. Bernhard, H. Shaked, R. L. Hitterman, J. D. Jorgensen, “**Generic superconducting phase behavior in high- $T_c$  cuprates:  $T_c$  variation with hole concentration in  $\text{YBa}_2\text{Cu}_3\text{O}_{7-\delta}$ .**” Phys. Rev. B. **51**, 12911, 1995.
- [95] Senta Karotke, “**High Frequency Conductivity of Superconductive  $(\text{Nd}_{1-y}, \text{Ca}_y)\text{Ba}_2\text{Cu}_3\text{O}_{6+x}$  and  $(\text{Y}_{1-y}, \text{Ca}_y)\text{Ba}_2\text{Cu}_3\text{O}_{6+x}$  single crystals,**” Diploma Thesis, University of Karlsruhe/University of Maryland, 2001.
- [96] Y. J. Uemura, L. P. Le, G. M. Luke, B. J. Sternlieb, W. D. Wu, J. H. Brewer, T. M. Riseman, C. L. Seaman, M. B. Maple, M. Ishikawa, D. G. Hinks, J. D. Jorgensen, G. Saito, and H. Yamochi, “**Basic Similarities among Cuprates, Bismuthate, Organic, Chevrel-Phase, and Heavy-Fermion Superconductors Shown by Penetration-Depth Measurements,**” Phys. Rev. Lett. **66**, 2665-2668, 1991.
- [97] C. Panagopoulos, J. R. Cooper, and T. Xiang, “**Systematic behavior of the in-plane penetration depth in d-wave cuprates,**” Phys. Rev. B **57**, 13422-13425, 1998.
- [98] Y. S. Gou, H. K. Zeng, J. Y. Juang, J. Y. Lin, K. H. Wu, T. M. Uen, and H. C. Li, “**Determination of the doping dependence of the penetration depth using YBCO microstrip ring resonators,**” Physica C **364-365**, 408-410, 2001.
- [99] Hardy *et al.*, Proc. Of 10<sup>th</sup> Anniv. Workshop, 1996.

- 
- [100] D. van der Marel, A. J. Leggett, J. W. Loram, and J. R. Kirtley, “**Condensation energy an high- $T_c$  superconductivity**,” Phys. Rev. B **66**, 140501, 2002.
- [101] Microlab/FXR, “**PIM Application Note: PASSIVE INTERMODULATION (PIM)**”, <http://microlab.fxr.com/pimnte.htm>.
- [102] AMP, “**RF Coax Connectors/Appendix C – Intermodulation in RF Coaxial Connectors**,” <http://www.amp.com/communications/com>.
- [103] <http://www.summitekinstruments.com>.
- [104] J. Halbritter, “**A review of weak/strong links and junctions in high- $T_c$  superconductors as a transition to a Mott insulator**,” Supercond. Sci. Technol. **16**, R47-R69, 2003.
- [105] O. V. Abramov, G. I. Leviev, V. G. Pogosov, and M. R. Trunin,” **Microwave response of a  $\text{YBa}_2\text{Cu}_3\text{O}_{7-x}$  superconducting ceramic**,” JETP Lett. **46**, 546-548, 1987.
- [106] An alternative way to measure the nonlinear response of superconductors is to do the following. Apply just enough input power at frequency  $f$  to keep the harmonic power  $P_{3f}$  (or  $P_{2f}$ ) constant as the sample temperature is changed. In this way, one will apply a “constant perturbation” to the sample and always keep it near its equilibrium state.



- 
- [107] G. M. Luke, Y. Fudamoto, K. M. Kojima, M. I. Larkin, J. Merrin, B. Nachumi, Y. J. Uemura, Y. Maeno, Z. Q. Mao, Y. Mori, H. Nakamura, and M. Sigrist, “**Time-reversal symmetry-breaking superconductivity in  $\text{Sr}_2\text{RuO}_4$** ,” *Nature* **394**, 558-561, 1998.
- [108] F. Tafuri and J. R. Kirtley, “**Spontaneous magnetic moments in  $\text{YBa}_2\text{Cu}_3\text{O}_{7-d}$  thin films**,” *Phys. Rev. B* **62**, 13934-13937, 2000.
- [109] A. Maniv, E. Polturak, and G. Koren, “**Observation of Magnetic Flux Generated Spontaneously During a Rapid Quench of Superconducting Films**,” *Phys. Rev. Lett.* **91**, 197001, 2003.
- [110] Jason P. Sydow, Michael Berninger, and Robert A. Buhrman, “**Effects of Oxygen Content on YBCO Josephson Junction Structures**,” *IEEE Trans. Appl. Supercond.* **9**, 2993-2996, 1999.
- [111] R. F. Kiefl, J. H. Brewer, I. Affleck, J. F. Carolan, P. Dosanjh, W. N. Hardy, T. Hsu, R. Kadono, J. R. Kempton, S. R. Kreitzman, Q. Li, A. H. O’Reilly, T. M. Riseman, P. Schleger, P. C. E. Stamp, H. Zhou, L. P. Le, G. M. Luke, B. Sternlieb, Y. J. Uemura, H. R. Hart, and K. W. Lay, “**Search for Anomalous Internal Magnetic Fields in High- $T_c$  Superconductors as Evidence for Broken Time-Reversal Symmetry**,” *Phys. Rev. Lett.* **64**, 2082-2085, 1990.

# CURRICULUM VITAE

Name: Sheng-Chiang Lee

Permanent Address: 409 Beacon Hill Terrace, Gaithersburg, MD 20878

Degree and date to be conferred: Ph.D., 2004

Title of Dissertation: Measurements of Doping-Dependent Microwave Nonlinearities in High-Temperature Superconductors

Date of Birth: October 20, 1975

Place of Birth: Taipei, Taiwan

Collegiate Institutions Attended:

Institution	Dates Attended	Degree Earned	Date of Degree
National Taiwan University	1993-1997	B.S., Physics	1997
University of Maryland	1997-2004	Ph.D., Physics	2004

Working Experience:

1. Research Assistant, University of Maryland, College Park, Maryland (1998 – Present)
2. Teaching Assistant, University of Maryland, College Park, Maryland (1997 – 1998)

Professional Publications:

1. Sheng-Chiang Lee and Steven M. Anlage, “**Doping Dependent Time-Reversal Symmetric Nonlinearity of  $YBa_2Cu_3O_{7-\delta}$  thin films**”, to be published in Physica C (2004); cond-mat/0306416v2
2. Sheng-Chiang Lee and Steven M. Anlage, “**Study of Local Nonlinear Properties Using a Near-Field Microwave Microscope**”, IEEE Trans. Appl. Supercond., vol. 13, pp.3594-3597, 2003
3. Sheng-Chiang Lee and Steven M. Anlage, “**Spatially-Resolved Nonlinearity Measurements of  $YBa_2Cu_3O_{7-\delta}$  Bi-Crystal Grain Boundaries**”, Appl. Phys. Lett. **82**, 1893 (2003)
4. S.C. Lee, C. P. Vlahacos, B. J. Feenstra, Andrew Schwartz, D. E. Steinhauer, F. C. Wellstood, and Steven M. Anlage, “**Magnetic Permeability Imaging of Metals with a Scanning Near-Field Microwave Microscope**”, Appl. Phys. Lett. **77**, 4004 (2000)

Presentations and Posters:

1. “Searching for Time-Reversal Symmetry Breaking States in Cuprate Superconductors” – Poster at the MRS Fall Meeting, Boston, Massachusetts, December 2003.
2. “Evaluation of Time-Reversal Symmetry Breaking in  $\text{YBa}_2\text{Cu}_3\text{O}_{7-\delta}$  Thin Films Using the Near-Field Microwave Microscope” – Presentation at the APS March Meeting, Austin, Texas, March 2003.
3. “Study of Local Nonlinear Properties Using a Near-Field Microwave Microscope” – Poster at the Applied Superconductivity Conference, Houston, Texas, August 2002.
4. “Study of Local Nonlinearity of High- $T_c$  Superconductors Using Near-Field Microwave Microscope” – Poster at the APS March Meeting, Indianapolis, Indiana, March 2002.
5. “Exploration of Intrinsic Nonlinearity of High- $T_c$  Superconductors” – Presentation at the APS March Meeting, Seattle, Washington, March 2001.

6. “Magnetic Permeability of Metals & FMR Field Imaging with the Scanning Near-Field Microwave Microscope” – Presentation at the APS March Meeting, Seattle, Washington, March 2001.